Advancements in Wind Energy Metrology
UPWIND 1A2.3

Risø-R-Report

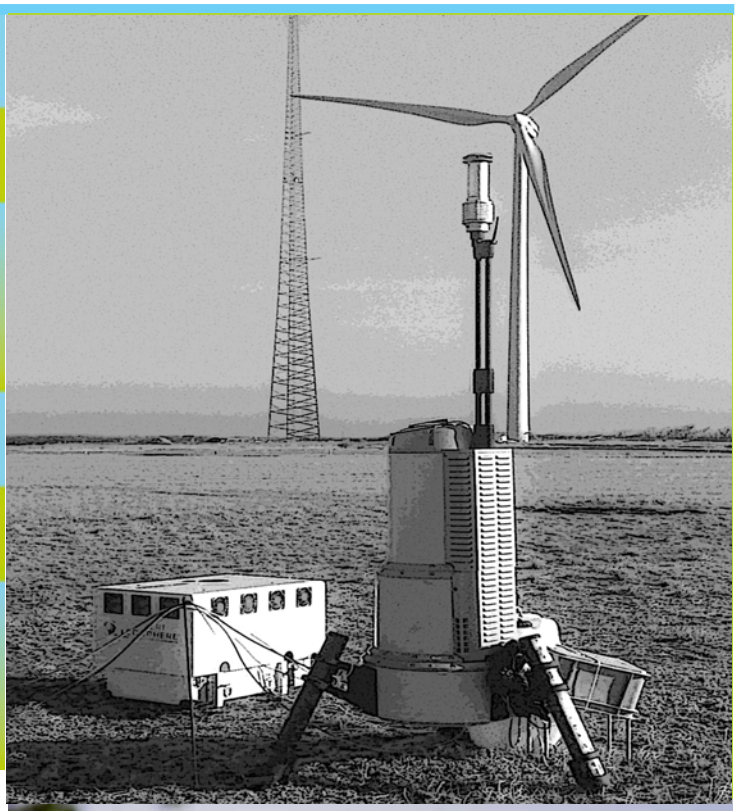

Editors:
T.F. Pedersen and R. Wagner

Authors:
N. Angelou, F. Bingöl, M. Courtney, B. Diznabi,
D. Foussekis, J. Gottschall, K.H. Hansen , H.E. Jørgensen,
L. Kristensen, G.C. Larsen, P. Lindelöw-Marsden, J. Mann,
T. Mikkelsen, U.S. Paulsen, T.F. Pedersen, A. Peña,
A. Sathe, M. Sjöholm, R. Wagner

Risø-R-1752(EN)
February 2011

Risø DTU
National Laboratory for Sustainable Energy

Editors: Troels F. Pedersen and Rozenn Wagner
Title: Advancements in Wind Energy Metrology – UPWIND 1A2.3
Division: VEA/TEM

Risø-R-1752(EN)
February 2011

Abstract (max. 2000 char.):
An overview of wind related metrology research made at Risø DTU over the period of the UPWIND project is given. A main part of the overview is devoted to development of the Lidar technology with several sub-chapters considering different topics of the research. Technical problems are not rare for this new technology, and testing against a traditional met mast have shown to be efficient for gaining confidence with the ground based Lidar technology and for trust in accuracy of measurements. In principle, Lidar measurements could be traceable through the fundamental measurement principles, but at this stage of development it is not found feasible. Instead, traceability is secured through comparison with met masts that are traceable through wind tunnel calibrations of cup anemometers. The ground based Lidar measurement principle works almost acceptable in flat terrain. In complex terrain and close to woods the measurement volume is disturbed because the flow is no longer horizontally homogeneous. These conditions require special attention and correction methods. Due to the large measurement volume, ground based Lidars perform a spatial averaging which has the effect of a low pass filter on turbulence measurements. Theory and measurements seem to be in good agreement. Lidar measurements from a rotating spinner have been performed. The analysis show good perspectives for scanning the incoming wind, which may lead to better controlled wind turbines. Lidars have also been used to scan the wake of wind turbines. These measurements document the meandering wake pattern.

The second part of the overview considers power performance measurements. A new investigation on the influence of wind shear points to a revision of the definition of a power curve. A new measurement method has been developed which has a good chance of being implemented in the present revision of the IEC performance standard. Also, a turbulence normalization method has been tested but not found efficient enough for inclusion in the IEC standard. In relation to the coming IEC standard on performance verification with the use of nacelle anemometry, IEC61400-12-2-CD, nacelle anemometry has been studied, both with experiments and in theory. An alternative to nacelle anemometry has been developed, the so-called spinner anemometer. This type of sensor measures yaw-error with high absolute accuracy, and avoids the draw-backs of nacelle anemometry because the spinner anemometer is positioned in front of the rotor. Advances in classic mast measurement technologies have also been made. A mast flow distortion correction method has been developed to improve classical state of the art mast measurements. Finally, an optical method for measurements of turbine vibrations is considered.

ISSN 0106-2840
ISBN 978-87-550-3851-6

Contract no.:
EU-FP6 UPWIND project

Group's own reg. no.:
1125053-01

Sponsorship:

Cover :
A pulse-lidar and a continuous lidar in front of a wind turbine and mast at Høvsøre test site

Pages:99
Tables:4
References:133

Information Service Department
Risø National Laboratory for Sustainable Energy
Technical University of Denmark
P.O.Box 49
DK-4000 Roskilde
Denmark
Telephone +45 46774005
bibl@risoe.dtu.dk
Fax +45 46774013
www.risoe.dtu.dk

Contents

Preface

In broad sense advancements in metrology in the wind energy sector is in a rapid development. This is specifically the case with regard to measurements of the wind in the boundary layer of the atmosphere. The development is related to the increase of size of wind turbines with higher towers and larger rotors sweeping deeper into the atmospheric boundary layer. This up-scaling of wind turbine technology is a continuous process where the UPWIND project tries to look into the crystal sphere to prepare for the larger turbines. The heights of these larger machines are at the limit of classic meteorological mast measurement techniques. This is why remote sensing and especially Lidar technologies are in the focus of today's wind related metrology research. However, classical wind measurement techniques still needs to be polished in order to be able to compare and verify development of the new remote sensing techniques and to meet the increasing requirements on measurement accuracy in performance measurements. This report is an overview of metrology research made at Risø DTU over the period of the UPWIND project.

1 Introduction

While the first part of the UPWIND metrology task was to identify measurement methods available in the past (the metrology database), another part was to identify metrology problems that need attention in further work, and a third part to consider problems to advance the progress in metrology in wind energy. Problems with existing wind measurement technologies have been identified. Although earlier and present EU-projects have considered classical mast measurement methods, which significantly advanced the state of the art of mast cup and sonic anemometry, but still development needs were identified for these types of measurements. Requirements for detailed turbulence measurements call for better procedures in international standards on sonic anemometer calibration and classification. This task is considered now in the revision work on the IEC standard on performance measurements. The rapid development of remote sensing wind measurement technologies such as Lidar and Sodar, have lead to a substantial number of projects over the last years, nationally and internationally. Ground based Lidar technology has almost reached a mature stage. In the past few years calibration and traceability issues have been considered and the technology is now being introduced in the IEC power performance standard revision for wind shear measurements.

2 LiDAR

2.1 Lidar testing

Rozenn Wagner, Mike Courtney, Julia Gottschall

1. Introduction

Wind measurements are fundamental to the wind energy industry. For both wind resource and power performance testing, the mast-mounted cup anemometer is the dominant and only formally accepted sensor for wind speed. This robust, simple and accurate instrument has served the industry well. However, the rapid increase in wind turbine size over the past few years has exposed the cup anemometer's Achilles heal – the mast structure needed to locate the cup anemometer at the hub-height of the wind turbine. With typical hub-heights now often exceeding both 80 and 90m, traditional mast-mounted cup anemometry has become an expensive and logistically complex affair. At the same time, the current practice of basing power performance measurements on a single, hub-height wind speed measurement becomes intuitively more and more suspect for such huge rotor swept areas. Recent numerical studies [1] indicate that the correlation between measured electrical power and wind speed increases if the wind speed is based on a weighted average of the wind speed profile over the entire rotor rather than on a single point measurement. Here, remote sensing is set to play a major role.

An alternative to mast-mounted anemometry is ground-based lidars. They have the potential to replace mast measurements and in time, to perform with comparable accuracy to cup anemometers. Since the emergence of sufficiently coherent lasers at wavelengths compliant with fiber optic components (so-called 'fiber lasers'), lidar systems can now be built using quality tested, standard telecommunications components, available off-the-shelf and connected together by standard terminated optical fibers. The lasers consume relatively low electrical power and do not require elaborate cooling systems. Since precise alignment is no longer generally an issue, robust portable systems can be realized. Eye-safety concerns can also be overcome since the majority of fiber lasers emit at the eye-safe wavelength of 1.5µm.

Several commercial lidar systems are now available. Two of them have been extensively tested by Risø DTU at the Test Station for Large Wind Turbine located at Høvøsre, in Denmark under the auspices of UpWind (WP6). It is our belief that the insight gained in this testing has played a significant role in the development of these systems. A comprehensive list of lidar error sources derived from these investigations can be found in Lindelöw [4]. Our extensive experience in comparing lidar measurements to those obtained from instruments on an adjacent met mast has enabled us to establish a procedure for lidar testing (Chapter xx). Although this procedure needs to be adapted to the type of lidar tested, the most important steps give a general frame that is recommended to be followed for all lidar verifications.

2. Method

The lidar testing procedure developed and used by Risø DTU follows 3 main steps: the choice of the appropriate location, the data selecton and the analysis. These 3 steps are further described below.

2.1 Test site, reference instruments and measurement sector

As the basic assumption for these lidars is that the wind field is horizontally homogeneous, the test site must be flat. Moreover, as lidars are becoming very accurate, it is important to use very good instruments as reference for the testing. Therefore the cup anemometers and wind vanes used as reference should be carefully calibrated and mounted on the mast. Furthermore, wind lidars are wind profilers, therefore the measurements should be compared at several heights simultaneously.

Risø DTU Test Station for Large Wind Turbines is located on the west coast of Denmark. This site comprises a met mast of 116m equipped with Risø cup anemometers at 5 levels and wind vanes at 2 levels. Surrounded by farm land on the east side and by the cost on the west side, this site is very much suitable for lidar testing [1].

Figure 1 The row of wind turbines at Høvsøre with the 116.5m meteorological tower in the foreground and the 160m beacon mast between the first and second wind turbine. The picture is taken from a low flying aircraft to the south-west of the mast.

Finally the measurement sector should exclude the wind directions for which either the reference sensor or the lidar measurements are perturbed by the wake of the mast or any obstacles (e.g. wind turbine).

2.2 Data selection

To maximize the comparability between the lidar and the reference measurements and the repeatability between different instances of the test, the sample data are filtered before evaluation according to the following criteria:

a) Reference data
   1. The data for which the reference cup anemometer are suspected of being influenced by icing (either on a temperature criterion or by comparison to another close cup anemometer) are removed.
   2. Only mean wind speeds between 4 and 16 m/s are considered as this is the wind speed range for which cup anemometers are calibrated.
   3. Cup anemometer measurement must be corrected for mast and boom effects. This effect can affect the measurements by up to 2% for boom mounted instruments. At Risø DTU test site, a correction was implemented based on the comparison of simultaneous wind speed measurements by two cup anemometers mounted on two different booms (with different orientation) at the same height (see chapter 3.1 in this report).

b) Lidar data

   The lidar measurements are selected according to their signal to noise ratio (SNR) or equivalent in the same manner that is recommended to be applied in the field.

2.3 Data analysis

Three quantities are analysed: the 10 minute mean wind speed, the 10 minute standard deviation and the 10 minute standard deviation of the wind speed.

The 10 minute mean wind speeds measured by the lidar are compared to the simultaneous cup measurements first with a linear regression analysis, where the gain offset and R2 are checked.

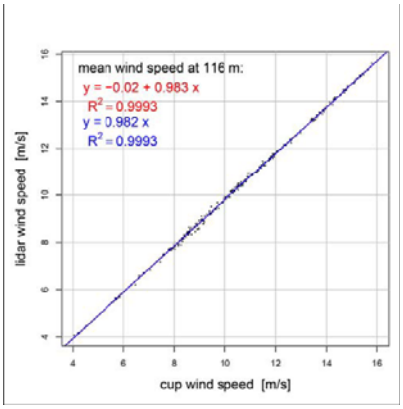

Figure 2 Illustration of linear (1-parametric) regression for mean wind speed at 116m for a Windcube WLS7 [3]

This analysis is completed by a 2 parametric regression, i.e. lidar wind speed versus cup wind speed and local shear, see example in Figure 3. The 2-parametric regression enables us to detect a sensing height error. However this advanced analysis is based on a measurement of the local shear, which requires a heavy instrumentation (at least one wind sensor above the level of measurement and one below) [2]. Finally, the lidar error, defined as the difference between the lidar and the cup measurements, plotted versus various parameters such the wind speed, direction or SNR, can reveal some tendencies in the lidar measurements.

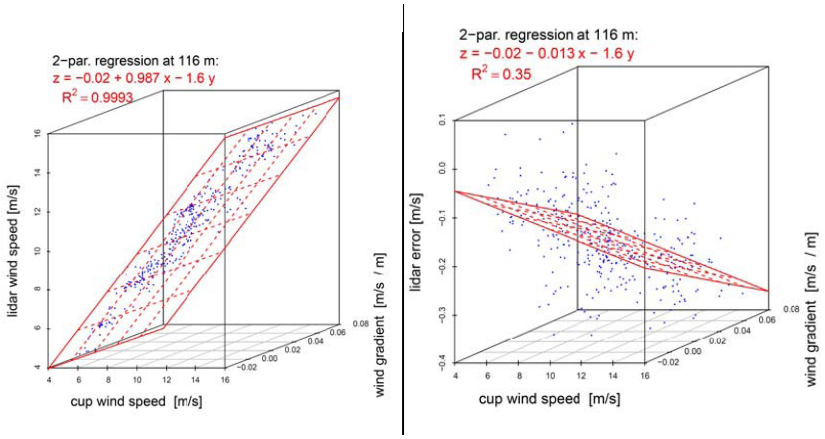

Figure 3 Illustration of 2-parametric regression at 116m for a Windcube WLS7[3]

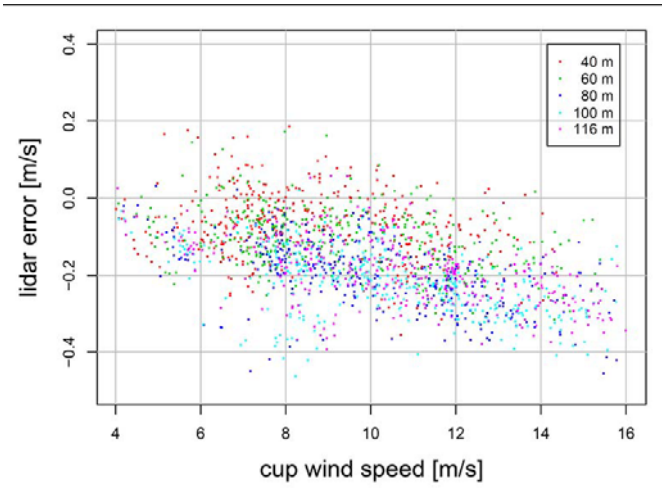

Figure 4 Lidar error versus wind speed for a Windcube WLS7 [3]

The 10 minute mean direction is analysed with a linear regression.

Finally, a linear regression is also performed for the standard deviation of the wind speed. This is not expected to result in a gain close to 1 since a lidar cannot resolve turbulent structure smaller than the probe volume, moreover the lidar sampling frequency is significantly smaller than that of a cup anemometer (see chapter 2.4).

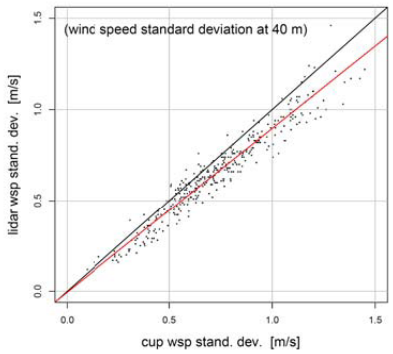

Figure 5 Illustration of linear regression for wind speed standard deviation at 116m for a Windcube WLS7[3]

3. Discussion and conclusions

The suggested procedure is general frame for lidar testing resulting from the many verifications performed at Høvøsre. It may not be as systematic as the calibration procedure for a cup anemometer since the difference between lidar systems is of different nature than the difference between cup anemometers. However, we believe that it is for now (due to missing alternative) the best way to verify the performance of such an instrument. Moreover the traceability of the lidar measurements is achieved by the comparison to the calibrated reference sensors. To be complete, such a procedure must include an evaluation of the uncertainty budget. This is described in more details in the next section.

References

[1] Wagner R, Antoniou I, Petersen SM, Courtney M, Jørgensen HE., The influence of the Wind Speed Profile on Wind Turbine Performance Measurements, Wind Energy, 12,issue: 4, 348-362, (2009).

[2] Lindelöw P, Courtney M, Parmentier R, Cariou JP, Wind shear proportional errors in the horizontal wind speed sensed by focused, range-gated lidars, In: IOP Conf. Series: Earth and Environmental Science 1 (2008) 012001.

[3] Gottschall J, Courtney M, Verification test for three WindCube™ WLS7 LiDARs at the Høvsøre test site. Risø-R-1732(EN) 2010.

[4] Lindelöw-Marsden P, UpWind D1. Uncertainties in wind assessment with LIDAR, Risø-R-1681, Risø 2008.

2.2 Lidar measurements traceability

Julia Gottschall

The need for measuring wind speed and direction at greater heights and at several levels simultaneously gains in importance as wind turbines get larger and higher. For this purpose, remote sensing profilers become very attractive for resource assessment and power performance testing. However, the existing standards only permit the use of cup anemometers as standard instruments. The main issue preventing the use of remote sensors in such standards is the need to maintain the traceability of the measurements in the international standard system.

As main outcome of our work during the last years, we have defined a verification procedure that enables us to achieve the required traceability for lidar profilers. The procedure is based on a direct comparison of the measurements from the lidar and reference sensors mounted on a mast at various height levels. In a first step, the data are corrected and filtered to obtain a representative data set ensuring a repeatable test. Secondly, a linear regression is applied to the data for each height. Three different regression models may be considered here. The third step is a bin-average analysis of the lidar error, i.e. the difference between the lidar and reference measurements, forming the basis for the ensuing uncertainty estimation.

The results of the verification test are both used to calibrate the lidar measurements and to derive a corresponding uncertainty budget. A significant limitation of the procedure is the considerable uncertainty introduced by the reference sensors themselves. The decision as to whether to apply the derived lidar calibration or not therefore mainly depends on the interpretation of this reference uncertainty and the assumed and observed biases.

The work on lidar measurement traceability is directly connected to our more general activities on lidar testing (see chapter 2.2). However, an even stronger focus is put on the estimation of uncertainties and the necessary requirements for a standardization of the applied procedures. As already mentioned, traceability of the lidar measurements is a prerequisite for introducing lidars as standard instruments to the different standard procedures in wind energy (as e.g. the common IEC or MEASNET standards). A significant part of our work has directly influenced the present revision of the IEC 61400-12-1 standard on power performance testing with the introduction of remote sensing instruments as one of its major issues.

Two scientific publications were prepared on the topic of lidar measurement traceability: a technical paper for the Wind Energy journal, to be published in a special issue on the UpWind project in 2011 [1], and a proceedings paper for the EWEC 2010 [2].

References:

[1] J. Gottschall, R. Wagner, M. Courtney, H. E. Jørgensen, and I. Antoniou: *Lidar profilers in the context of wind energy – A verification procedure for traceable measurements*; Wind Energy (submitted, to be published as Special Issue paper 2011).

[2] J. Gottschall, M. Courtney, P. Lindelöw, and A. Albers: *Classification of lidar profilers – or: how to introduce lidars to power performance testing*; EWEC 2010 (poster and proceedings paper).

2.3 Lidar in complex terrain

Ferhat Bingöl, Jakob Mann and Dimitri Foussekis[(1)]
(1) CRES, Centre for Renewable Energy Sources, 19th km Marathonos Ave, 19009, Pikermi Attiki Greece

Abstract
Conically scanning lidars assume the flow to be homogeneous in order to deduce the horizontal wind speed. However, in mountainous or complex terrain this assumption is not valid implying a risk that the lidar will derive an erroneous wind speed. The magnitude of this error is measured by collocating a meteorological mast and a lidar at two Greek sites, one hilly and one mountainous. The maximum error for the sites investigated is of the order of 10 %. In order to predict the error for various wind directions the flows at both sites are simulated with the linearized flow model, WAsP Engineering 2.0. The measurement data are compared with the model predictions with good results for the hilly site, but with less success at the mountainous site. This is a deficiency of the flow model, but the methods presented in this paper can be used with any flow model.

1. Introduction

Lidars (light detection and ranging) are becoming an alternative to meteorological masts for vertical profile measurements for the assessment of wind energy potential. They have several advantages over traditional anemometry such as ease of deployment and that large heights can be reached without excessive costs [1]. They have shown encouraging results reproducing cup anemometer wind speeds within a few percents both on- and off-shore, and several different types of lidars have been investigated thoroughly [2,3]. This success has been limited to flat terrain and it is the purpose of this paper to investigate the performance in mountainous terrain, occasionally called complex terrain. Here the flow is no longer homogenous and that can give a large bias on the horizontal wind speed estimated from the lidar. To illustrate this very simply Figure 1 shows a lidar shooting at an angle φ from vertical upwind and downwind, situated in flow where the horizontal wind speed U is constant, but where the vertical wind speed W changes linearly with the downwind position x. This could crudely mimic the flow over a hill where (in case of $\alpha \equiv dW/dx$ negative) the upstream is tilting upwards and downstream downwards. The projected wind speed on the upwind beam is:

$$v_{up} = -(U + h\alpha) \sin \varphi ,$$

while it is:

$$v_{down} = (U + h\alpha) \sin \varphi$$

for the downwind beam. Assuming wrongly horizontal homogeneity, we can calculate the horizontal velocity as estimated from the lidar:

$$Ulidar = (v_{down} - v_{up})/2 \sin \varphi = U + h\alpha \quad (1)$$

and we see in the case of negative α that the horizontal wind is underestimated.

One remarkable fact seen from (1) is that the underestimation is not diminished as φ tends to zero. In other words, reducing φ will not reduce the bias on the horizontal velocity. It is a simple, but rather tedious exercise, to show that the same is true for a more realistic setting, where the horizontal wind is obtained from a conical scan in an arbitrary linear flow: $U_i(x) = U_i(0) + x_j \partial U_i / \partial x_j$ where $U_i(x)$ is the wind vector at the position x, $U_i(0)$ is the wind vector at the center of the conical circle and the derivative term is the first order Taylor expansion around x = 0 [4].

We studied the bias caused by inhomogeneous flow, both by comparing collocated mast and lidar measure ments in complex terrain, and by predicting the bias by help of a simple flow model. We focus on the continuous wave (cw) lidar ZephIR developed by QinetiQ [5].

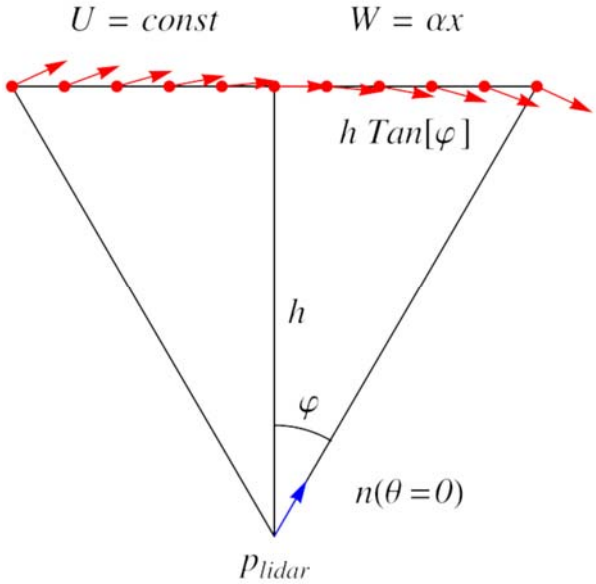

Figure 1 Simplified lidar scanning geometry in a linearly changing mean flow. The lidar is shooting up- and down-stream with a half opening angle φ. The horizontal component of the mean wind U is constant while the vertical component W changes linearly with position x.

2. Test Sites

The Lavrio site is located 38 km SE of the center of Athens close to the coast of the Aegean Sea. The experiment took place between 2007-Dec-01 and 2008-Jan-15. The highest point is 200 m ASL and main wind direction is 0°. The 100 m triangular lattice reference meteorological mast is equipped with cup anemometers and vanes at five heights (10 m, 32 m, 54 m, 76 m and 100 m). Cups are to the east and vanes are to the west. There are also ultrasonic 3D Gill anemometers at three heights (34 m, 78 m, 98 m) which are not used in this study due to problems with icing but this does not influence the used cup anemometers and vanes. Additionally, the temperature profile is measured using differential thermometers, as well as, the atmospheric pressure and the solar radiation. Dedicated instrumentation is used for signal protection, filtering and conditioning. The lidar is located nearly 12 m north of the mast. The measurement heights are 32 m and 78 m.

The Panachaiko site is located 165 km northwest of Athens, at Vounogiorgis Mountain, south east of the village Sella, 14 km south of the Patras Sea. The experiment ran from 2007-Sep-19 to 2007-Oct-11. The terrain in the vicinity of the site is very complex. Highest point is 2000 m in the region where the experiment surrounding is between 1700 and 1750 m ASL. The prevailing wind directions are ENE and SW. The triangular lattice reference meteorological mast has six cup anemometers (10 m, 20 m, 30 m, 40 m, 54 m) and two vanes (40 m, 54 m). Additionally, there are also air temperature and relative humidity measurements at 54 m. The lidar is located nearly 20 m WSW of the mast. The lidar measurement heights are 30 m and 55 m. In both experiments lidar data are collected by the standard QinetiQ software and synchronized with mast data by the CRES WindRose software. Instruments are calibrated according to the requirements of IEC61400- 12-1:2005/Annex F and MEASNET guidelines at CRES Laboratory for Wind Turbine Testing.

3. Theory and method

WAsP Engineering

WAsP Engineering is a linearized flow model developed at Risø DTU. We have tested the model with different resolutions and map sizes [4] and have chosen a small enough resolution that the results did not change significantly. The resolution should be so fine that the lidar's scanning circle is well resolved. For those reasons we choose for the Lavrio site a 4 m resolution with a 2.5 km map size and for the Panahaiko site a 10 m with a 5 km map size.

Modelling the Lidar Error

We want to calculate the radial velocity in the direction of the laser beam vr in the points forming a circle, where the lidar is measuring. Then we use these values to derive horizontal wind speed in the same way as it is done in the QinetiQ ZephIR. We also calculate the horizontal wind speed at the mast position at the relevant heights. The QinetiQ ZephIR makes scans in different heights with 50 data points on each circle. These data are fitted to a rectified trigonometric function to give the horizontal wind speed, the vertical wind speed and the wind direction. The instrument has a sign ambiguity on the wind vector, but that is resolved by crudely measuring the wind direction at the instrument. Detailed information on modelling can be found in paper "Conically scanning lidar error in complex terrain" [6].

4. Results

At Lavrio, most of the winds are northerly which means it is blowing from lidar to the mast. The scatter plots (Figure 2-top) show generally 5 % to 7 % errors in wind speed measurements. For the WAsP Engineering model we have used 3 km to 3 km map with 4 m resolution simulating the wind direction from 0◦ to 360◦ with 2◦ bins. We have used all the data from the mast at each height and averaged them according to the wind direction in 6◦ bins.

The comparison between the model and the measurements is shown in Figure 2 (lower two plots) and shows good correlation in some sectors. The mast is voluminous, thus the selected data must be far from boom di rection which is 113°. These sectors are marked with light grey areas in the plots for ±30°. The ideal ratio line of one is also shown and it represents the cases where there is no difference between the lidar and the mast measurements. The black line is the model and the points are the measurement results.

Especially for northerly directions the model predicts the lidar error well for both heights, while for the southerly directions the prediction is not so good. We believe this can be a result of the limitation of WAsP Engineering. In southerly directions very close to the site there are steep slopes. In this sector and height, the flow model has difficulties predicting the tilt angles as compared to sonic measurements for periods with no icing problems.

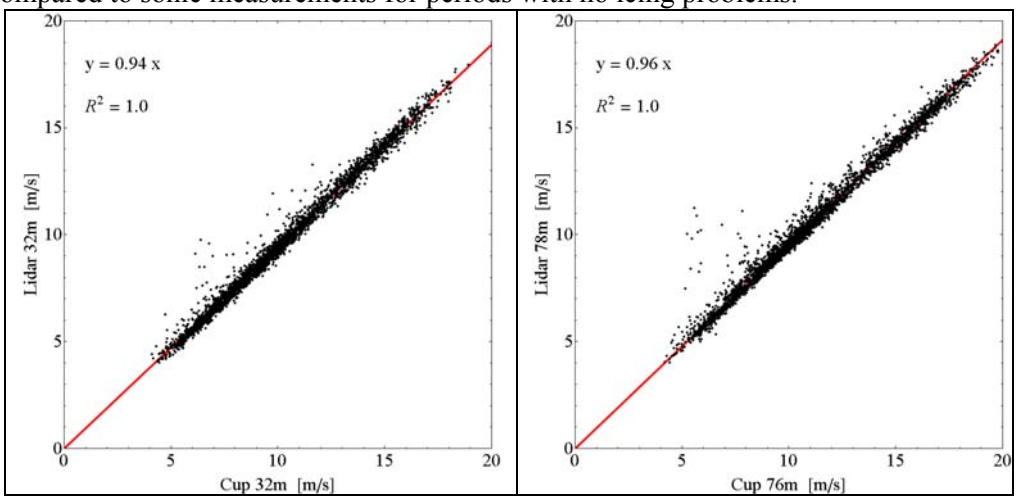

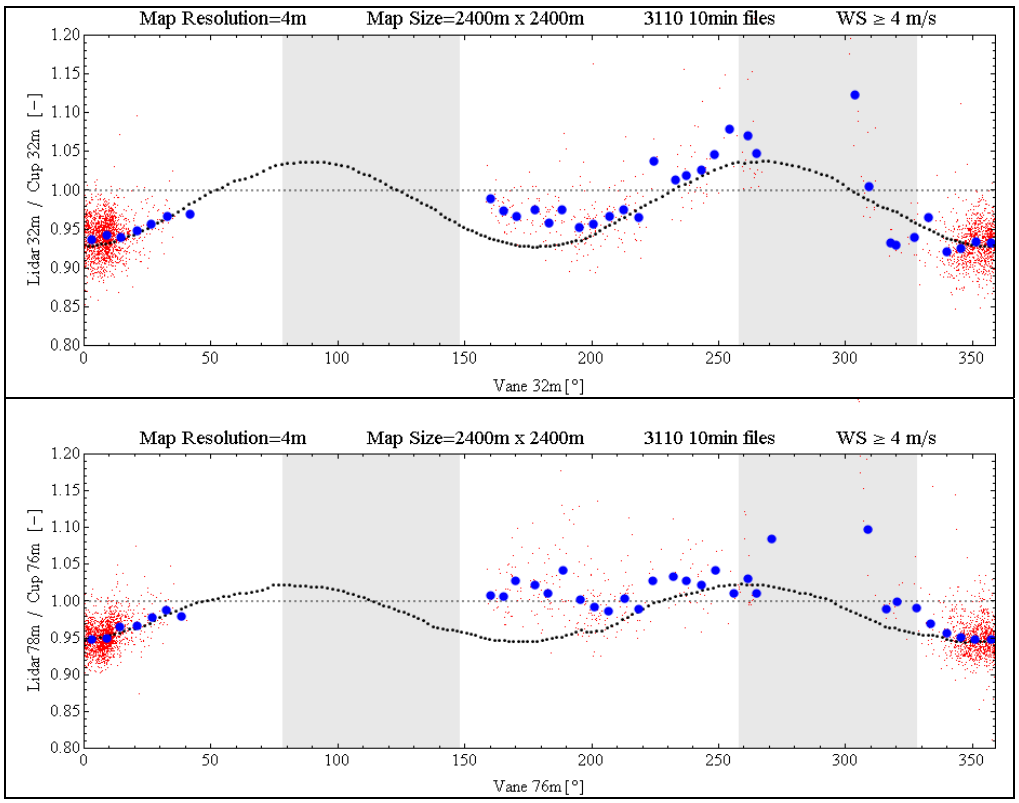

Figure 2: Lavrio: The scatter plots show generally 4 % to 6 % errors in wind speed measurements (top). Lower two plots are the comparison between the model and the measurement data for two different heights. Small red dots are the error ratio for each 10 minutes measurement, big blue dots are the averaged 6◦ bins according to the wind direction and medium black dots are the model results. The mast shadow is marked with grey rectangles. The ideal ratio line of one, dashed blue, is also shown and it represents the cases where there is no difference between the lidar and the mast measurements. Especially for northerly directions the model predicts the lidar error well for both heights, while for the southerly directions the prediction is not so good.

The second site, Panahaiko, is much more complex than Lavrio, so there are many sectors which could be problematic for WAsP Engineering to model. The scatter plots in Figure 3 (top) show data for all directions. The mast at Panahaiko is smaller than at Lavrio so the sector with flow distortion is smaller (±25°) shown in grey in the figure. The boom direction is 210◦. The comparison between the modelled error and the measurements as a function of direction is shown in Figure 3 (lower two plots). It is not a perfect prediction, but the model gives the right order of magnitude for this complex site.

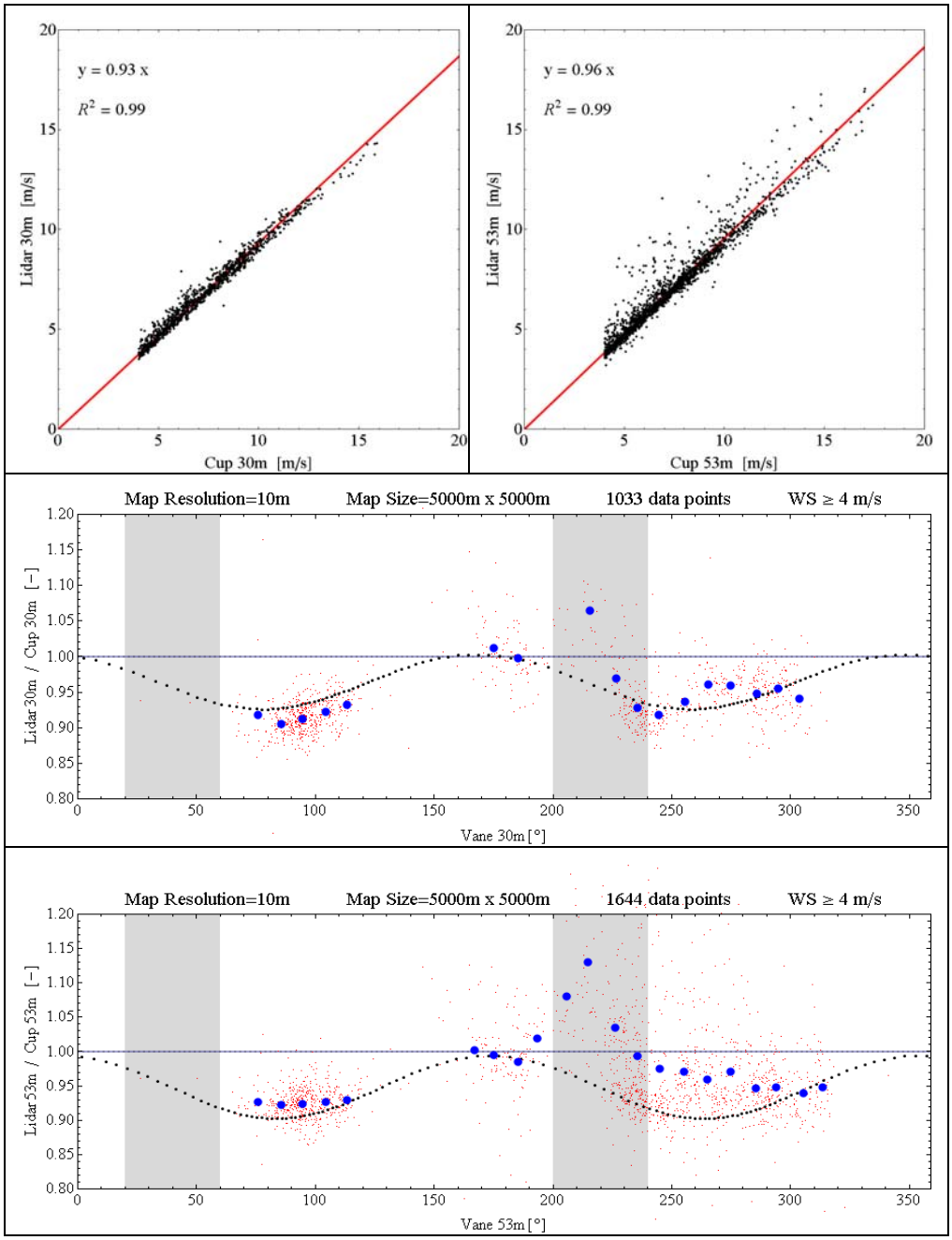

Figure 3: Panahaiko: The scatter plots show generally 4 % to 7 % errors in wind speed measurements (top). Lower two plots are the comparison between the model and the measurement data for two different heights. Small red dots are the error ratio for each 10 minutes measurement, big blue dots are the averaged 10◦ bins according to the wind direction and medium black dots are the model results. The mast shadow is marked with grey rectangles. The ideal ratio line of one, dashed blue, is also shown and it represents the cases where there is no difference between the lidar and the mast measurements. It is not a perfect prediction, but the model gives the right order of magnitude for this complex site.

5. Conclusion

Lidars, used over flat homogeneous terrain, show errors in the mean wind speed of only a few percent. We have shown that in complex terrain of the type commonly used for wind turbine parks, errors in the horizontal wind speed as measured by a conically scanning lidar can be of the order of 10 %. This is due to the lack of horizontal homogeneity of the flow, which is assumed in the interpretation of the lidar data. The findings are based on two experiments

involving collocated lidars and meteorological masts in complex terrain, together with flow calculations over the same terrains. For that calculation we use WAsP Engineering, and we find that the calculations match the experiment except for some sectors where the terrain is particularly steep. This is not surprising, since the WAsP Engineering is built on a linearized flow model, which is only valid for limited terrain slopes. The model is not for highly complex terrain that can incorporate the stability effect in any reliable way. Furthermore most of the wind speeds analyzed, from both sites, are quite high so it is not unreasonable to assume neutral stratification. That is why there is concluding thoughts about stability. To make more reliable predictions of the error in very steep terrain, other more advanced flow models must be used. We investigate the resolution needed for the WasP Engineering calculations.

Acknowledgments
This study is a part of UpWind project funded under the EU's Sixth Framework Programme (FP6).

References

[1] EMEIS, S., M. HARRIS, R.M. BANTA, 2007: *Boundary- layer anemometry by optical remote sensing for Wind energy applications.* – Meteorol. Z. 16, 337–347.

[2] KINDLER, D., A. OLDROYD, A. MACASKILL, D. FINCH, 2007: *An eight month test campaign of the Qinetiq ZephIR system: Preliminary results.* – Meteorol. Z. 16, 479–489.

[3] COURTNEY, M., R. WAGNER, P. LINDELÖW, 2008: *Testing and comparison of lidars for profile and turbulence measurements in wind energy*. – IOP Conference Series: Earth and Environmental Science 1, 012021, 14 pp.

[4] BINGÖL , F., J. MANN, D. FOUSSEKIS, 2008: *Modeling conically scanning lidar error in complex terrain with WAsP engineering.* – Report Risø–R–1664(EN), Risø National Laboratory for Sustainable Energy – DTU, available at www.risoe.dtu.dk/Knowledge base/publications/Reports/ ris-r-1664.aspx

[5] SMITH , D.A., M. HARRIS, A.S. COFFEY, T. MIKKELSEN, H. E. JØRGENSEN, J. MANN, R. DANIELIAN, 2006: *Wind lidar evaluation at the Danish wind test site in Høvsøre.* – Wind Eenergy 9, 87–93.

[6] BINGÖL , F., J. MANN, D. FOUSSEKIS, 2008: *Conically scanning lidar error in complex terrain* Meteorologische Zeitschrift, Vol. 18, No. 2, 189-195 (April 2009) Open Access Article

2.4 Lidar turbulence measurements

Jakob Mann, Ameya Sathe, Julia Gottschall and Mike Courtney

Abstract
Modeling of the systematic errors in the second-order moments of wind speeds measured by continuous-wave (ZephIR) and pulsed (WindCube) lidars is presented. These lidars use the velocity azimuth display technique to measure the velocity vector. The model is developed for the line-of-sight averaging and the full extent of conical scanning. The predictions are compared with the measurements from the ZephIR, WindCube and sonic anemometers at a flat terrain test site, under different atmospheric stability conditions. It is observed that the systematic errors are up to 90% for the vertical velocity variance, whereas they are up to 70% for the horizontal velocity variances. The systematic errors also vary with atmospheric stability, being lowest for the very unstable conditions. It is concluded that with the current measurement configuration, these lidars cannot be used to measure turbulence precisely.

1. Introduction

Atmospheric turbulence is one of the main inputs in assessing loads on the wind turbines. Thus, accurate estimation of wind speed and turbulence at several heights is crucial for the successful development of a wind farm. In wind energy the current standard is the use of meteorological masts equipped with cup/sonic anemometers. However, tall meteorological masts are very expensive, and offshore, the costs increase significantly. The advent of remote sensing devices like lidars gives a further boost to the development of wind energy. In recent years with the introductions of the ZephIR and WindCube there has been a surge in the verification campaigns of comparing the lidar mean wind speed with that of a cup anemometer for wind energy applications [1, 2, 3, 4]. [3] discuss the advantages and disadvantages of CW and pulsed lidars. In order to use a lidar as a standard measuring instrument in the future, a fair degree of confidence is also required in the turbulence measurements.

Although lidars have been introduced in wind energy recently, for meteorology they have been investigated previously to measure turbulence using different scanning techniques. A comprehensive review is given in [5] that covers different remote sensing techniques for turbulence measurements including lidars. A review of the use of lidars for wind energy applications is also presented in [6]. Recently, studies have been carried out to model the spatial averaging effects [7] and compare the 3D turbulence measurements using three staring lidars [8]. [9] estimated the momentum fluxes using lidars and modelled the unfiltered turbulence from the CW lidar, where the model compares reasonably well with the measurements. In the present work, line-of-sight averaging and the full extent of conical scanning is considered.

A theoretical model is developed to estimate the systematic errors in the second-order moments of wind speeds measured by lidars. The systematic errors are the errors that arise due to the averaging effect in the line-of-sight and the quite large circle in which lidars measure wind speed. Two types of lidars are considered, the ZephIR developed by QinetiQ (Natural Power) as a continuous wave (CW) lidar and the WindCube developed by Leosphere as a pulsed lidar. The verification is carried out by comparing the variances measured by the ZephIR and WindCube with that of the sonic anemometers placed at different heights on a meteorological mast. Further details will be given in [10].

2. Theory

The model in this study is developed for the velocity azimuth display (VAD) technique of lidar scanning.

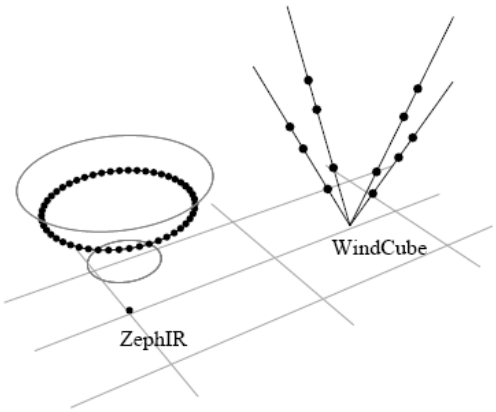

Figure 1 Schematic of the velocity azimuth display scanning of the two lidar systems. The ZephIR scans at many points on the azimuth circle, with a typical scan consisting of measurements of v_r at 50 points on the azimuth circle.

Fig.1 shows the lidar emitting the laser beam in different ways for the two lidar systems treated here. The line-of-sight velocity (also called radial velocity v_r) is given as the dot product of the unit directional vector and the velocity field at the point of focus for a CW lidar, and the center of the range gate for the pulsed lidar,

$$v_r(\theta) = n(\theta) \cdot \mathbf{v}(d_f n(\theta)) \tag{2}$$

where θ is the azimuth angle, d_f is the focus distance for the CW lidar, and the distance to the center of the range gate for the pulsed lidar at which the wind speeds are measured, $\mathbf{v} = (u, v, w)$ is the instantaneous velocity field evaluated at the focus point $d_f n(\theta)$, and $n(\theta)$ is the unit directional vector given as,

$$n(\theta) = (\cos\theta\sin\varphi, \sin\theta\sin\varphi, \cos\varphi) \tag{3}$$

In reality it is impossible to obtain the backscattered radiation precisely from only the focus point, and there is always backscattered radiation of different intensities from different regions in space along the line-of-sight. Hence, it is necessary to assign appropriate weights to the backscattered intensity such that the weight corresponding to the focus point is the highest. Mathematically, the weighted average radial velocity can be written as,

$$\tilde{v}_r(\theta) = \int_{-\infty}^{\infty} \varphi(s) n(\theta) \cdot \mathbf{v}(sn(\theta) + d_f n(\theta))\, ds \tag{4}$$

where *φ(s)* is any weighting function, integrating to one, and *s* is the distance along the beam from the focus. For simplicity we assume that *s=0* corresponds to the focus distance. The following are the main assumptions of our model:

The terrain is homogeneous

The flow field is frozen during the scan

Eq. (4) with an appropriately chosen *φ(s)* models the averaging well

The spatial structure of the turbulent flow is described well by the spectral tensor model of [11]

Systematic turbulence errors for the ZephIR lidar

If we assume the coordinate system such that *u* is aligned to the mean wind direction, *v* is perpendicular to the mean wind direction, *w* is the vertical component, and the mean wind comes from the North then $\tilde{v}_r(\theta)$ can be expressed as,

$$\tilde{v}_r(\theta) = A + B\cos\theta + C\sin\theta \tag{5}$$

where the coefficients $A=w_{qq}\cos\phi$, $B=u_{qq}\sin\phi$ and $C=v_{qq}\sin\phi$ and the sign ambiguity in $\tilde{v}_r(\theta)$ is neglected (see [9]). We use the subscript *qq* to denote the velocity components measured by ZephIR, since they are not the true velocity components *u*, *v* and *w*. The assumption that the mean wind comes from the North is only made for simplicity. For a lidar measuring at many points on the azimuth circle the choice of the mean wind direction does not matter since averaging over the entire circle is carried out. The values of the coefficients *A*, *B* and *C* are found using least squares method by fitting Eq. (5) to the measured values of $\tilde{v}_r(\theta)$ at all the scanned azimuth angles. The coefficients can be written as Fourier integrals,

$$A = \frac{1}{2\pi}\int_0^{2\pi} \tilde{v}_r(\theta)d\theta \tag{6}$$

$$B = \frac{1}{\pi}\int_0^{2\pi} \tilde{v}_r(\theta)\cos\theta\, d\theta \tag{7}$$

$$C = \frac{1}{\pi}\int_0^{2\pi} \tilde{v}_r(\theta)\sin\theta\, d\theta \tag{8}$$

We proceed by deriving expressions for the w_{qq} variance. The expressions for the (co-)variances of the remaining components of wind velocity can be derived in a similar manner. The variance of *A* is written as $\sigma_A^2 = \langle A'^2 \rangle$, where $\langle\ \rangle$ denotes ensemble averaging of a variable. From the above definition of *A* we can write,

$$\sigma_A^2 = \langle w_{qq}'^2 \rangle \cos^2\phi \tag{9}$$

Using Eq. (6) we can also write,

$$\sigma_A^2 = \left\langle \left(\frac{1}{2\pi}\int_0^{2\pi} \tilde{v}_r'(\theta)d\theta \right)^2 \right\rangle \tag{10}$$

Lengthy manipulations allow us to express σ_A^2 in terms of the three-dimensional spectral velocity tensor $\Phi_{ij}(\mathbf{k})$, which is the Fourier transform of the covariance tensor.

Let $\alpha_i(\mathbf{k}) = \left(\int_{-\infty}^{\infty} \varphi(s) \left[\frac{1}{2\pi}\int_0^{2\pi} n_i(\theta) e^{i(s+d_f)\mathbf{k}\cdot n(\theta)} d\theta \right] ds \right)$. Eq. (10) can then be written as (using Eq. (9)),

$$\langle w_{qq}'^2 \rangle \cos^2\phi = \int \Phi_{ij}(\mathbf{k})\alpha_i(\mathbf{k})\alpha_j^*(\mathbf{k})dk \tag{11}$$

where * denotes complex conjugation. Thus the integral reduces to evaluating $\alpha_i(\mathbf{k})$ since the analytical expressions for $\Phi_{ij}(\mathbf{k})$ are given in [11]. Eq. (11) can then be estimated numerically. For a CW lidar, $\varphi(s)$ is well approximated by a Lorentzian function [12],

$$\varphi(s) = \frac{1}{\pi}\frac{1}{l^2 + s^2} \tag{12}$$

where l is the Rayleigh length ($l = \lambda_b \, d_f^2/\pi \, r_b^2$, where $\lambda_b = 1.55\mu$m is the wavelength of the emitted radiation, and $r_b = 19.5$ mm is the beam radius). The resulting $\left\langle w_{qq}^{'2} \right\rangle$ can now be evaluated and a similar approach is taken for deriving u_{qq} and v_{qq} variances, and for the variances measured by the WindCube. An additional complication for the ZephIR is that the beam rotates three times calling for an extra averaging in time, which is included in the theoretical prediction in figure 2(a) and 2(b), see [10] for details. We present the systematic errors as the ratio of the lidar second-order moments and the true second-order moment.

3. Comparison of models with the measurements

Meteorological measurements are taken at 10, 20, 40, 60, 80 and 100 m at Risø DTU's test center at Høsvøre in Denmark. We use the high frequency (20 Hz) and 10-min mean sonic anemometer measurements at 40--100 m between December 2008 and November 2009. Sonic anemometers are placed at several heights on the North booms of the meteorological mast and the lidars are place within a few tens of meters of the mast.

In order to avoid the influence of the wakes from the wind turbines and the met-mast on lidar measurements, and inhomogeneities due to the sudden change of roughness (sea-land transition), only the eastern sector (50°--150°) is analyzed. Only observations of wind speeds greater than 4 m/s are used.

The estimation of Φ_{ij} using the model from [11] requires three input parameters, $\alpha\varepsilon^{2/3}$, which is a product of the spectral Kolmogorov constant α [13] and the rate of viscous dissipation of specific turbulent kinetic energy $\alpha\varepsilon^{2/3}$, a length scale L and an anisotropy parameter γ. We use these input parameters obtained by fitting the sonic anemometer measurements under different atmospheric stability conditions, at several heights on the meteorological mast in the eastern sector [14].

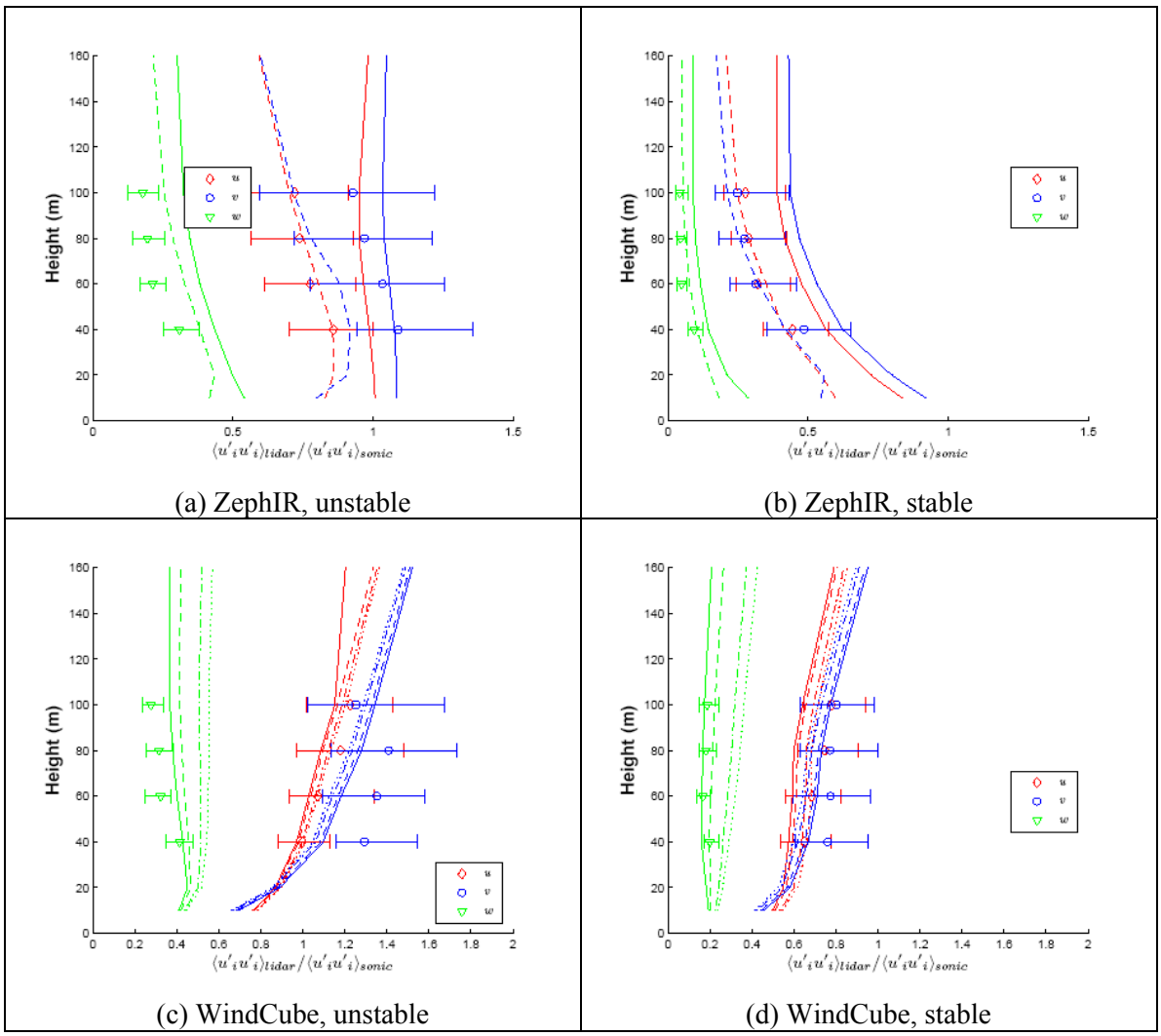

(a) ZephIR, unstable

(b) ZephIR, stable

(c) WindCube, unstable

(d) WindCube, stable

Figure 2 Systematic errors under different atmospheric stability conditions. The markers indicate measurements. The solid lines are the theoretical plots without the low-pass filter, and the dashed lines are with the low-pass filter for the ZephIR. For the WindCube the theoretical error depends weakly on wind direction, so it is plotted as a dotted line for 0°, dash-dot line for 15°, dashed line for 30° and solid line for 45°.

Fig.2 shows the comparison of the modelled systematic errors (section 2) with the measurements for *u*, *v* and *w* variances. The theoretical plots are shown with and without the three second time averaging. The measurements are represented as median, first and third quartiles respectively. We infer the following:

- The systematic errors vary considerably under different atmospheric stability conditions -- The variation is up to 50% for *u* and *v* variances, and up to 20% for *w* variance. There is also a large variation in the length scales of different velocity components resulting in varying attenuation of the variances.
- For the ZephIR the systematic errors increase with height under all atmospheric stability conditions -- This is due to a quadratic increase in the probe length with height [1]. The diameter of the scanning circle also increases with height. This results in a greater attenuation of the second-order moments with increasing height.
- For the WindCube the systematic errors decrease with height for the *u* and *v* variances under all atmospheric stability conditions, probably because the probe length is constant with height, and hence, at lower heights there is a combined averaging effect due to the probe length and the diameter of the scanning circle.

Considering that at lower heights the length scales are smaller than at higher heights, it is likely that the variances are attenuated greater at lower heights than at higher heights.

- The systematic errors in *w* variance is much larger (approximately 3—5 times) than that of the *u* and *v* variances -- This is due to the very small length scales of the *w* component as compared to those for *u* and *v*, resulting in the attenuation of the *w* variance of up to 90%. The *u* and *v* variances are attenuated up to 70%.
- The trend of the systematic errors predicted by both models is in agreement with the observations at all heights.
- The calculation with the three second averaging is in better agreement with the measurements at all heights.

4. Conclusion

The main goal of this paper is to understand the systematic errors in the second-order moments of CW and pulsed lidars. In particular, we model the systematic errors for the ZephIR and WindCube, which are used as CW and pulsed lidars respectively. In general, the model predicts the systematic errors quite well although there are many uncertainties associated with the assumptions made in the model.

As of now, with the current measurement configuration, the systematic errors of the second-order moments are quite large and depend strongly on stability, and hence, it is clear that the ZephIR and WindCube cannot be used to measure turbulence precisely.

We are currently looking into alternative ways of analyzing the lidar data and different beam configurations that would render turbulence measurements more feasible. One idea is to use two different half opening angles as in [15], who show that all terms in the Reynolds stress tensor can be obtained by using the single beam statistics, without resorting beam covariances, which is done in this paper. That would require serious hardware changes to the instruments treated here. Another idea is to supplement the analysis with information on the width of the Doppler spectra, as done for the momentum flux in [9], in order to neutralize the effect of along beam averaging.

References

[1] D. A. Smith, M. Harris, A. S. Coffey, T. Mikkelsen, H. E. Jørgensen, J. Mann, and R. Danielian, *Wind lidar evaluation at the Danish wind test site in Høvsøre*, Wind Energy, vol. 9, pp. 87–93, 2006.

[2] D. Kindler, A. Oldroyd, A. Macaskill, and D. Finch, *An eight month test campaign of the QinetiQ ZephIR system: Preliminary results*, Meteorologische Zeitschrift, vol. 16, no. 5, pp. 479–489, 2007.

[3] M. Courtney, R. Wagner, and P. Lindelöw, *Testing and comparison of lidars for profile and turbulence measurements in wind energy*, in 14th International Symposium for the Advancement of Boundary Layer Remote Sensing, 2008.

[4] A. Peña, C. B. Hasager, S.-E. Gryning, M. Courtney, I. Antoniou, and T. Mikkelsen, *Offshore wind profiling using light detection and ranging measurements*, Wind Energy, vol. 12, no. 2, pp. 105–124, 2009.

[5] D. A. M. Engelbart, M. Kallistratova, and R. Kouznetsov, *Determination of the turbulent fluxes of heat and momentum in the ABL by ground-based remote-sensing techniques (a review)*, Meteorologische Zeitschrift, vol. 16, no. 4, pp. 325–335, 2007.

[6] S. Emeis, M. Harris, and R. M. Banta, *Boundary-layer anemometry by optical remote sensing for wind energy applications*, Meteorologische Zeitschrift, vol. 16, no. 4, pp. 337–347, 2007.

[7] M. Sjöholm, T. Mikkelsen, J. Mann, K. Enevoldsen, and M. Courtney, *Spatial averaging-effects in turbulence measured by a continuous-wave coherent lidar*, Meteorologische Zeitschrift, vol. 18, no. 3, Sp. Iss. SI, pp. 281–287, 2009.

[8] J. Mann, J. Cariou, M. Courtney, R. Parmentier, T. Mikkelsen, R. Wagner, P. Lindelöw, M. Sjöholm, and K. Enevoldsen, *Comparison of 3D turbulence measurements using three staring wind lidars and a sonic anemometer*, Meteorologische Zeitschrift, vol. 18, no. 2, Sp. Iss. SI, pp. 135–140, 2009.

[9] J. Mann, A. Peña, F. Bingöl, R. Wagner, and M. S. Courtney, *Lidar scanning of momentum flux in and above the surface layer*, Journal of Atmospheric and Oceanic Technology, vol. 27, no. 6, pp. 792–806, 2010. DOI:10.1175/2010JTECHA1389.1.

[10] A. R. Sathe, J. Mann, J. Gottschall, and M. Courtney, *Estimation of the systematic errors in lidar turbulence measurements*. To be published in JTECH, 2011.

[11] J. Mann, *The spatial structure of neutral atmospheric surface-layer turbulence*, Journal of Fluid Mechanics, vol. 273, pp. 141–168, 1994.

[12] C. M. Sonnenschein and F. A. Horrigan, *Signal-to-noise relationships for coaxial systems that heterodyne backscatter from atmosphere*, Applied optics, vol. 10, no. 7, p. 1600, 1971.

[13] A. S. Monin and A. M. Yaglom, *Statistical Fluid Mechanics*, vol. 2. MIT Press, 1975.

[14] A. Peña, S.-E. Gryning, and J. Mann, *On the length scale of the wind profile*, Quarterly Journal of the Royal Meteorological Society, 2010. Accepted.

[15] W. L. Eberhard, R. E. Cupp, and K. R. Healy, *Doppler lidar measurements of profiles of turbulence and momentum flux*, Journal of Atmospheric and Oceanic Technology, vol. 6, pp. 809–819, 1989.

2.5 Lidar measurement from spinner

Nikolas Angelou, Torben Mikkelsen, Kasper H. Hansen and Mikael Sjöholm

1. Introduction

One important topic of investigation for the wind energy is the optimization of the power performance of wind turbines. So far, the wind turbine control is based on the measurement of the direction and the speed of the wind, from instruments (wind vanes and anemometers) installed on top of the nacelle. These instruments are subject to errors due to the effect of the blades rotation to the wind flow. Furthermore the wind turbine's operation parameters are being adjusted to the wind fluctuations, only after their detection.

A wind lidar instrument mounted on top of the nacelle or installed in the spinner of a wind turbine, when aligned with the horizontal axis of the wind turbine can provide detailed measurements of the wind characteristics (speed and direction) of the incoming wind flow at different distances from the rotor plane. Such an application offers an unimpeded view of the wind field that the wind turbine will experience.

The feasibility of this application can lead to the achievement of improved wind turbine control through lidar instruments mounted or integrated in wind turbines, with the benefits of enhanced power production performance, as well as increased life time of the wind turbine [1]. The optimization of the power production can be achieved through active lidar controlled yaw, rpm and pitch control of the blades. An increase of the life time of the wind turbine, by protecting the blades from intense bending moments, can be accomplished by timely lidar detection of approaching extreme wind events, e.g. gusts [2].

2. The SpinnerEx 2009 experiment

The feasibility of upwind observations via a spinner-mounted wind lidar was tested during the SpinnerEx 2009 experiment, held by Risø – DTU in collaboration with Natural Power (UK)., which was conducted as part of the new Danish research infrastructure facility activities under the auspices of Windscanner.dk.

For the needs of the SpinnerEx2009 experiment a QinetiQ (Natural Power, UK) ZephIR lidar was installed in the rotating spinner of a Vestas NM80 2.5 MW wind turbine, belonging to Dong Energy (DK). The QinetiQ (Natural Power) ZephIR lidar is a commercial available wind lidar, capable of measuring the wind characteristics (speed and direction), with a fast sampling rate (50 Hz) in distances between 10 m – 200 m. A built-in optical prism is used in order to deflect the laser beam and thus providing the capability to scan in a conical pattern. The performance of such a system has been verified through the comparison of the lidar measurements with cup anemometers installed in a met mast [3].

The ZephIR wind lidar was modified and installed into the rotating spinner of the Vestas NM80 wind turbine (see Figure 1), aligned with the horizontal axis of the wind turbine This way it was possible to investigate the structure of the incoming wind field in front of the wind turbine. Time series of wind speed measurements from the lidar with 50 Hz sampling rate were successfully obtained for approximately 60 days, during a measurement campaign which lasted from April to August 2009.

Figure 1 Photograph of the NM 80 wind turbine. Here it is visible the optical head of the QinetiQ's (Natural Power) ZephIR lidar in the tip of the wind turbine spinner (left). In addition it can be seen the interior of the spinner were the lidar was mounted (right).

Measurements in two distances away from the wind turbine were acquired, at 46 m and 100 m, respectively. These distances corresponded to 0.58 and 1.24 Ø (Ø: rotor diameter) upwind along the turbine shaft axis. The scanning patterns were achieved through the use of two different wedge-shaped optical prisms with deflection angles (from the zenith) 15 and 30 degrees, respectively.

While the wind turbine was operating the lidar was scanning the incoming field in a conical pattern in front of the rotor plane. This way it was possible to acquire real-time measurements of the radial wind speed in various heights. In terms of 10-min average values, it was possible to reconstruct the wind profile, with a resolution of 1 m, for an atmospheric layer ranging between ~40 and ~90 m.

A methodology was tested for the calculation of the yaw misalignment (θ_w) of the wind turbine, based on the assumption that the wind blows homogenously towards the whole rotor area of the wind turbine. This is expected to happen when the turbine is not affected by wakes of adjacent wind turbines or when there is no horizontal wind shear. The presence of a wake would lead to variations in the radial wind speed values, which could misinterpreted as a change of the wind direction. Additionally the wind direction is considered that it can be changing with height and therefore the calculation of the angle θ_w is done in several height layers. A detailed description of the method used can be found in [4].

For the verification of the results of this method data from the wind vane installed on top of the wind turbine as well as combined data from a met mast (wind vane) and from the NM80 wind turbine's control system were used. Figure 2 presents the yaw misalignment as measured from each one of the three aforementioned approaches, on the 30th of April 2009 between 01:00 and 03:30 am. It is expected that for the given period the wind flow is undisturbed from wind turbine wakes. It can be observed that the lidar is following relatively well the wind direction fluctuations measured from the wind vane on the nacelle. However when comparing with the met mast it appears a good correlation at the first hour, which is followed by a deviation of approximately 10 degrees, for the rest of the period. It has to be noted that the met mast was placed ~300 m away from the wind turbine.

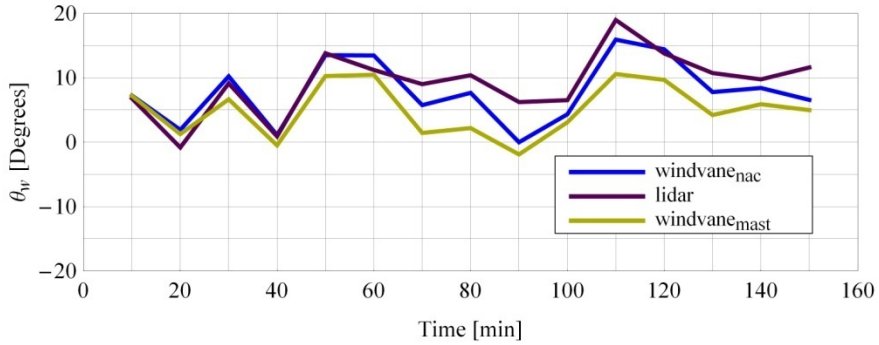

Figure 2 Yaw misalignment angle relative to the 10-min averaged mean wind direction measured by: 1) the upwind looking lidar (purple), 2) the wind turbines own nacelle-mounted wind vane behind the rotor (blue), and 3), the wind vane mounted at hub height in the nearby met-mast (yellow).

Using the yaw misalignment values of the wind turbine and the lidar's radial wind speed measurements it is possible to estimate the horizontal wind speed. Figure 3 presents such results, where it is observed a clear distinction between of the wind speed at different height layers, as expected for the stable atmospheric conditions which characterize this period. The knowledge of the horizontal wind speed along the rotor plane can be important both in the terms of power curve analysis as well as optimizing the power production of the wind turbine, through the implementation.

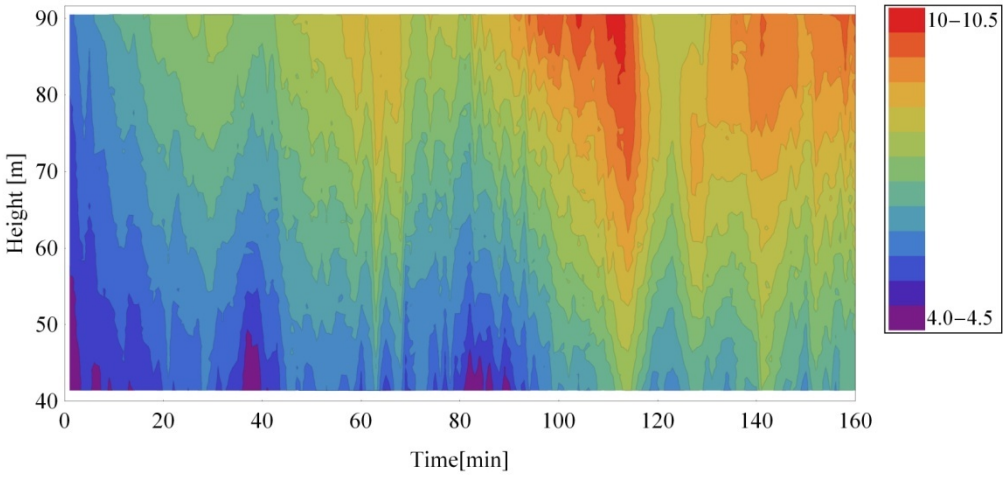

Figure 3 Horizontal wind speed measurements as derived from the ZephIR lidar, during the period between 01:00 and 03:00 on the 2009-04-30.

3. Conclusions

The results of this experiment demonstrate that a forward-looking spinner-mounted lidar is indeed able to measure wind components upwind at multiple sampling points distributed on a conically scanned circle in the rotor plane of a wind turbine. This knowledge is important for the understanding of the wind turbine's operation, of the wind field conversion in electrical energy and of the optimum modifications and improvements in the design and control of a wind turbine, in order to improve its efficiency.

Concluding, the integration of the lidar in the spinner of a wind turbine is proven very useful in the research of the incoming wind towards the rotor plane. Furthermore this innovative measurement concept offers the potential of active control of a wind turbine through a wind lidar. Incorporation of remote sensing wind data into the turbine control system can lead to improved energy yield and load reduction, through yaw, rpm and pitch control. However several parameters have to be taken into account during the lidar data processing, such as meteorological conditions (e.g. rain, fog and clouds), wake effects and terrain characteristics.

Further studies are planned that will include the investigation and modeling of the effect on the lidar measurements of the aforementioned parameters. Implementation of enhanced control algorithms utilizing real-time upwind measured wind data of different wind flow conditions is envisioned to contribute to the improvement of active control of wind turbines in the near future.

References

[1] Harris M., M. Hand and A. Wright, *"A Lidar for turbine control"*, Tech. Rep. NREL/TP – 500– 39154 National Renewable Energy Laboratory, NREL, Golden, Colorado, US, (2006).

[2] Harris M., D. J. Bryce, A. S. Coffey, D. A. Smith, J. Birkemeyer & U. Knopf, *"Advance measurement of gusts by laser anemometry"*, J. Wind Eng. 95, 1637 – 1647, (2007).

[3] D. A. Smith, M. Harris, A. S. Coffey, T. Mikkelsen, H. E. Jørgensen, J. Mann, and R. Danielian, "*Wind lidar evaluation at the Danish wind test site in Høvsøre*," Wind Energy, vol. 9, pp. 87–93, 2006.

[4] LIDAR Wind Speed Measurements from a Rotating Spinner: "*SpinnerEx 2009*", Angelou N, Mikkelsen T, Hansen KH, Sjöholm M, Harris M., Risø-R-1741(EN), (2010).

2.6 Doppler lidar mounted on a wind turbine nacelle

Nikolas Angelou, Jakob Mann, Mikael Sjöholm and Michael Courtney

1. Introduction

In the context of the UPWIND remote sensing working package, the potential of using a light detection and ranging (lidar) remote sensing instrument for the detection of the incoming wind flow in front of a wind turbine's rotor plane, was investigated. Such a system has the advantage of detecting the characteristics of the wind field, which the turbine will experience at a later stage [1]. Hence, offering the possibility of optimizing the power production, as well as mitigating the loads. Recent advancements of such applications include the calculation of the yaw misalignment of a wind turbine using wind lidar systems, which are either installed in the rotating spinner [2] or mounted on top of the nacelle of a wind turbine [3]. An important parameter for the interpretation and evaluation of a lidar system is the verification over which extent the instrument is capable of detecting the turbulent fluctuations of the wind speed. The objective of this experiment was the study of the turbulence attenuation induced in the lidar measurements, due to the spatial weighting average along the probe volume, through the analysis of the spectral characteristics of the lidar's wind speed measurements.

2. The experiment

For the purposes of this experiment a ZephIR prototype lidar was mounted on the nacelle of a V27 wind turbine (see Figure 1), which is installed inside the Risø DTU site area. The V27 wind turbine is a 225 kW model, with a hub height of 33.5 m and a rotor diameter equal to 27 m. The ZephIR prototype is a continuous wave (cw) wind lidar capable of acquiring wind speed measurements in different distance from the instrument.

Figure 1 ZephIR lidar's optical head mounted on the V27 wind turbine's nacelle.

The data analysis was focused on a time period, of approximately 20 hours, where the wind turbine was yawed in the direction where the line-of-sight of the lidar was pointing towards a meteorological mast (met mast), which could be found in the direction of 283° N and at a distance of 67.5 m (equivalent with 2.5 rotor diameters) away from the V27 wind turbine

The objective was to detect time intervals where the wind flow coincided with the line-of-sight of the lidar, thus minimizing any effects that the vertical component of the wind speed could have in the detection of the wind speed turbulence [4]. The lidar was operating in a staring mode and the focus distance was set to 67.5 m, which corresponded to the distance between the wind turbine and the met mast. The focal point of the lidar was expected to be approximately 1 m above the position of a USA-1 sonic anemometer; hence it can be assumed that the two instruments were measuring in almost the same location. Consequently it was possible to investigate both the correlation as well as the spectral characteristics of two different measurement concepts, a point (sonic anemometer) and a volume averaging (lidar).

3. Results

The regression analysis between the lidar and the sonic anemometer was performed using both 10-minutes and 10-Hz wind speed values, for this purpose the sonic anemometer measurements were projected to the line-of-sight of the lidar. Figure 2 presents the regression analysis plots for (a) the 10-minutes values acquired during a period of approximately 21 hours (12:20 2009/05/05 – 09:00 2009/05/06) and (b) for the 10-Hz values acquired during a 10-minutes period (16:40 – 17:40, 2009/05/05).

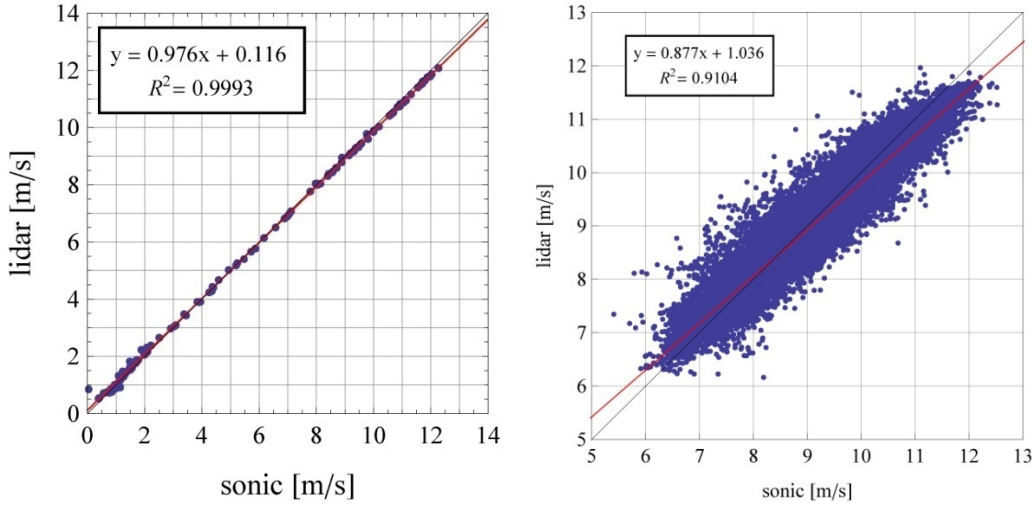

Figure 2 Regression analysis between the USA -1 sonic anemometer and ZephIR prototype wind speed measurements, for both 10-minutes (left) and 10-Hz values (right).

It was observed that the lidar was slightly underestimating the mean wind speed during a 10-minute period, in comparison with the USA-1 sonic anemometer. The two data sets presented a high correlation, which was described by the linear relationship $y_{lidar} = 0.976\ x_{sonic} + 0.116$, with a R^2 value of 0.9996. This observed offset could be explained by flow distortion around the Metek sonic anemometer is USA-1 type.

Regarding the 10-Hz data, it was observed that the lidar was overestimating the wind speed in the region of the lower wind speeds of this period (6 - 8 ms^{-1}), while underestimating in the region of 9 – 13 ms^{-1}. This phenomenon is caused by the filtering which has as an effect that the some of the wind speed fluctuations (either rapid increases or decreases) are being filtered out, due to the averaging over the lidar's probe volume. As a result a larger dispersion of the data was observed, thus decreasing the correlation to $R^2 = 0.9104$.

This turbulence attenuation was also observed when examining the turbulence spectra of the wind speed as measured from the ZephIR lidar and the USA-1 sonic anemometer (see Figure 3 a), where it can be seen that the amplitude of the wind speed fluctuations is being reduced above frequency values of ~0.03Hz. The spectral transfer function which describes the turbulence attenuation, which is induced in the lidar measurements, was estimated by means of spectral analysis using two different methods [5]. Figure 3b presents the calculated spectral transfer function in comparison with the theoretical model [6]. It was observed that the lidar was adequately measuring the turbulence fuctuations with wavenumbers below 0.01 - 0.03 m^{-1}. This limitation is attributed to the fact that the lidar measurements result from a convolution of the wind speed with a spatial weighting function, which acts in a similar fashion to a low pass filter [7].

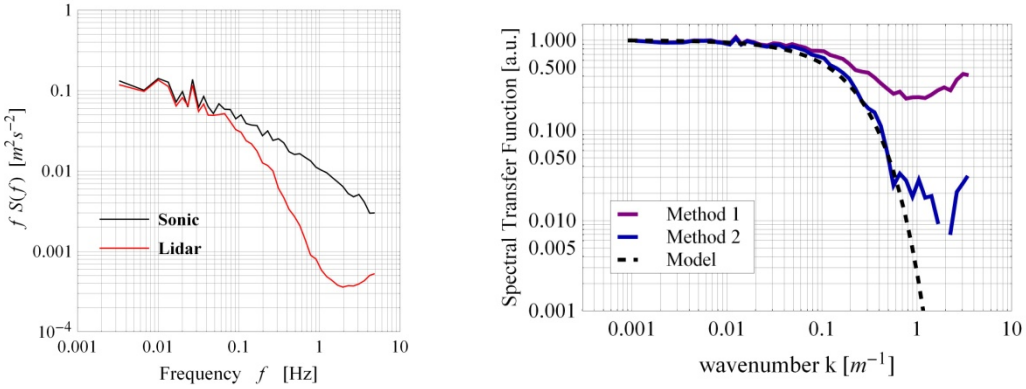

Figure 3 (a) Spectra of the wind speed turbulence as measured by the ZephIR prototype lidar (red line) and the USA-1 sonic anemometer (black line) and (b) The spectral transfer function as calculated following 2 different methods (blue and purple line) along with theoretical model (dashed).

4. Conclusions

In this experiment the theoretical expected limitations of a cw wind lidar capability in measuring wind speed turbulence, were tested. When attempting a regression analysis using 10 Hz mean values, it was observed a relative large dispersion of the data points, which is directly connected with the spatial filtering over the lidar's probe volume. The spectral transfer function, which describes this filtering, was calculated and good agreement was observed with the theoretical model. Moreover it was investigated the dependence of the spectral transfer function with the wind direction, as the relative offset between the direction of the line-of-sight and the wind direction increased, the larger was the noise amplitude in the higher frequencies and therefore the spectral transfer function was lifted up.

References

[1] Harris M., D. J. Bryce, A. S. Coffey, D. A. Smith, J. Birkemeyer and Knopf U., *Advance measurement of gusts by laser anemometry*, Journal of Wind Energy 95, 1637 – 1647, (2007).

[2] Mikkelsen T., Hansen K. H., Angelou N., Sjöholm M., Harris M., Handley P., Scullion R., Ellis G., and Vives G., *Lidar wind speed measurements from a rotating spinner*, Scientific Proceedings, EWEC, (2010).

[3] Dakin E., Pal A., Belen F., and Küpper M., *Boosting power production update*, Technical report, Catch the Wind, (2010).

[4] Mann J., Cariou J. P., Courtney M., Parmentier R., Mikkelsen T., Wagner R., Lindelöw P., Sjööholm M., and Enevoldsen K.. *Comparison of 3D turbulence measurements using three staring wind lidars and a sonic anemometer*, Meteorologische Zeitschrift, 18(2):135-140, (2009).

[5] Doppler lidar mounted on a wind turbine nacelle – UPWIND deliverable D6.7.1, Angelou N., Mann J., Courtney M., Sjöholm M., Risø-R-1757(EN), (2010).

[6] Sjöholm M., Mikkelsen T., Mann J., Enevoldsen K., and Courtney M., *Spatial averaging effects on turbulence measured by a continuous-wave coherent lidar*. Meteorologische Zeitschrift, 18:281-287, (2009).

[7] Smalikho I. N., *On measurement of dissipation rate of the turbulent energy with a cw Doppler lidar*, Atmospheric and Oceanic Optics, 8:733-793, (1995).

2.7 Lidar Measurements of Wake Dynamics

Ferhat Bingöl, Jakob Mann and Gunner C. Larsen

Abstract
The vast majority of wind turbines are today erected in wind farms. As a consequence, wake generated loads are becoming more and more important. Here we present a new experimental technique to measure the instantaneous wake deficit directly, thus allowing for quantification of the wake meandering as well as the instantaneous wake expansion expressed in a meandering frame of reference. The experimental results are used as a preliminary verification of the basic conjecture of a wake meandering model that essentially considers the wake as a passive tracer.

1. Introduction

While the time averaged wake behind a wind turbine has been studied extensively in recent times [1, 2, 3], due to its significant implications for energy production, studies of the dynamics of the wake, which may be of crucial importance for turbine loadings are more rare. The power production will also be marginally altered by the wake dynamics.

Here we present a new experimental technique to measure the instantaneous wake deficit directly, with the final goal of verifying wake models. The wind energy lidar (Light Detection and Ranging), ZephIR, was developed primarily to obtain vertical profiles of the wind vector. Comparisons with several tall, meteorological masts have already proven the instrument to be accurate in this respect over flat terrain [4, 5, 6]. Mounting the ZephIR lidar on a wind turbine nacelle has exciting scientific and technical perspectives and this is the first time a lidar has been mounted on a wind turbine to measure the downstream flow field. We have mounted the system on the back of the nacelle of a small wind turbine such that it views the downwind flow. Techniques are developed to move the laser beam across the wake horizontally and vertically. The wind speed is measured nearly 136 times per second. The instrument is focused in the range from one to ten rotor diameters downstream making it possible to study the meandering, shape, widening and attenuation of the wake deficit. The experiment is conducted primarily to test the simple hypothesis that the wake deficit is advected passively by the larger than rotor size eddies in the atmospheric flow, and that the wake at the same time widens gradually, primarily due to mixing caused by small scale atmospheric turbulence [7].

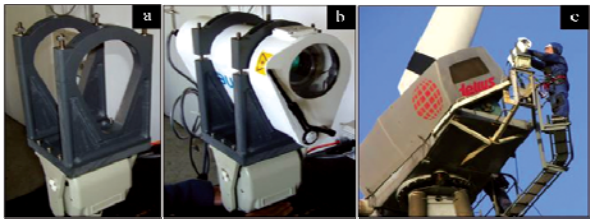

Figure 1: Adaptation in three steps: (a) Tilt and pan head is combined with a holder; (b) The lidar head is mounted on it; (c) The lidar is mounted behind the Tellus turbine looking downstream.

2. Wake meandering

The conceptual model for the meandering wake adopted here is based on the fundamental assumption that the transport of wakes in the atmospheric boundary layer can be modelled by considering the wakes to act as passive tracers driven by the large-scale turbulence structures. Modelling of the meandering process consequently includes considerations of a suitable description of the "carrier" stochastic transport media as well as of a suitable definition of the cut-off frequency defining large-scale turbulence structures in this context. For the stochastic modelling of wake meandering, we imagine a wake as constituted by a cascade of wake deficits, each "emitted" at consecutive time instants in agreement with the passive tracer

analogy [7]. We then describe the propagation of each "emitted" wake deficit, the collective description of which constitutes the wake meandering model.

Adopting Taylor's hypothesis, the downstream advection of the wake deficits are assumed to be controlled by the mean wind speed of the ambient wind field. With this formulation the wake momentum in the direction of the mean flow is invariant with respect to the prescribed longitudinal wake displacement. This is a considerable simplification allowing for a straight forward decoupling of the wake along wind deficit profile (and its expansion) and the wake transportation process.

As for the dynamics in the lateral and vertical directions, each considered wake cascade element is displaced according to the large-scale lateral and vertical turbulence velocities at the position of the particular wake cascade element at each time instant.

3. Instrumentation

The British company QinetiQ started working on a low cost lidar some years ago. The first prototype instrument was bought by Risø DTU in 2004 and has been used in various experiments since. The original design of the ZephIR Prototype was as a vertical scanning tool facilitating focusing of the laser beam at different heights between 5 and 200 m. At the given altitude it scans a circular pattern with a cone angle of 30.4◦ by means of an optical wedge from which the horizontal wind speed can be derived as described in [8].

The first tests to assess the quality of the instrument were performed at the Risø DTU Høvsøre Test Centre in Denmark at the end of 2004 and beginning of 2005 [9]. The studies showed very good correlation with Risø cup anemometer measurements.

In 2005 the instrument was adapted to wind turbine wake measurements by a series of upgrades. First the software was adjusted to achieve faster measurements. Subsequently, hardware upgrades and extensions improved the versatility of the instrument thus making it useful in very different type of experimental set-ups [10]. One of the important ideas in this respect was to remove the wedge from the device and turn it into a straight shooter scanner. The lidar does not need calibration for wind speed measurements, but focus distance calibration is needed to be sure that the instrument is focusing at the requested position. This calibration has been done at Risø.

Mounting the lidar onto nacelle has been done previously [11] with the aim of investigating possibilities for controlling the wind turbine based on upstream wind measurements. The lidar head was fixed, and measurements were performed in only one single spatial point at hub height. Our experiment is the first time a lidar has been used to measure downstream. The lidar moves and collects data at different locations in the downstream flow, and there is no intention to control the wind turbine with this data.

4. Software adaptations

Various kinds of software adaptations have been performed varying from signal processing and acquisition to Doppler spectra analysis. The ZephIR is a continuous wave lidar based on the Doppler shift effect. The focus distance of the instrument determines the measurement range. The light scatters off aerosols which are assumed to move with speed of air. However, in the range there might be other objects that do not move with the wind like rain drops or snow. If the objects are distributed inhomogenously, like in the presence of clouds, the wind may not be measured at the point of focus. Some analyses of these and additional problems have been presented in previous studies [5, 6, 9, 12]. The general conclusion on the issue is that the instrument is more reliable in dry weather with a higher concentration of aerosols in the air. Also, the focus range grows roughly with the square of the focus distance [10] therefore, even if we have tested our measurement technique at as large as 170 m, we preferred to use the measurement below 60 m focus distances to make our final remarks. The process of calculating the wind speed from the lidar signal has three steps illustrated in Figure 1 with data collected in this experiment. Firstly, a certain amount of data is acquired from the lidar and read as a stream of bytes. After that an averaged spectrum is generated by splitting this data into a number of equal parts, Fourier transforming, taking the absolute square and

finally averaging. The result is a single averaged spectrum with the peak value is directly proportional to the wind speed.

5. Working Modes

The conventional conical scanning mode is designed for measurements of spatially averaged wind vectors, whereas the purpose here is to record instantaneous wind speeds at many locations. In the first experiment the wedge was dismounted. This transforms the lidar device into a straight shooter, which measures the wind speed in the direction it is pointed. A tilt and pan head, which was originally designed for security cameras, was modified (Figure 1a), and the lidar head was mounted on it (Figure 1b). The head can move between ±35◦ in pan and ±15◦ in tilt. However, only the pan movement has been utilized in the experiment, and tilt is adjusted to align the laser beam parallel to the land surface. The recording process is controlled by a PC. The pan movements have been synchronized with the velocity measurements simply by measuring the pan position exactly at the same time the wind speed is measured, and a time stamp for the each measurement is recorded. The modified instrument has been mounted on the wind turbine looking downwind (Figure 1c). The lidar head is approximately at 29 m a.g.l. which is the hub height. The second part of the ZephIR – i.e. the laser source and process computer - is located in a shelter at the foot of the turbine and can be remotely controlled over a local area network.

After adaptation of the prototype ZephIR, three working modes have been developed including configurations with as well as without the wedge (Figure 3). The modes are described in detail in the following subsections.

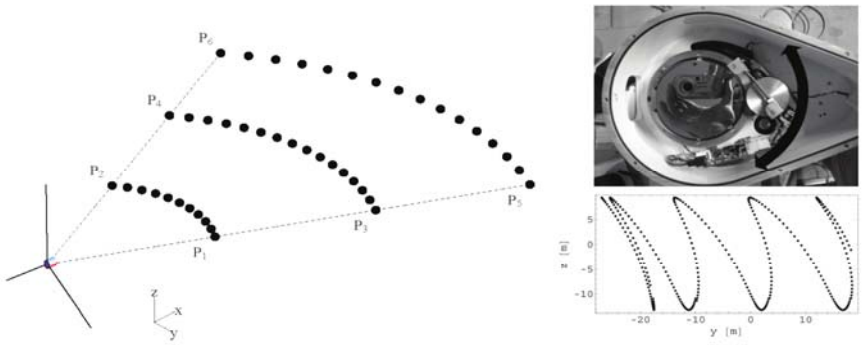

Figure 2: 1D modes without the wedge: (Left) Line Scan Mode focuses to a single distance, while panning between ±30°, the dots symbolized. Movement is continuous between two points; for example from P1 to P2 back and forth. However, Deep Line Scan Mode focuses to various programmed distances while panning. After every each line scan the lidar stops collecting data and focus to a new distance; for example, P1 to P2 - focus change - P3 to P4 - focus change - P5 to P6 and so on. The lidar can focus up to 200 m. After that it turns back to P1. 2D mode with the wedge: (Right-Top) The physical upgrade of the wedge mechanism. The wedge moves in arrow direction back and forth. (Right-Bottom) A sample of the Sphere Scan Mode pattern associated with a focus distance of 58 m. The horizontal axis is the lateral deflection (in meters) associated with the pan positions (±25◦), and the vertical axis is the vertical deflection (in meters) associated with the constrained wedge rotation. Each full 2D pattern scan might end up with different point positions, but they will always be within the same boundaries [13].

6. Test Site

The test site is a relatively flat and homogeneous terrain located at Risø DTU Roskilde, Denmark, and it is being used simultaneously also for other experiments. The dominant wind direction is´around 289◦ . The experimental set-up consists of the lidar system mounted on the

Tellus wind turbine along with two meteorological masts dedicated to wind field reference measurements.

The test turbine is a stall regulated, three bladed, Tellus 95 kW [14]. The hub height is 29.3 m, and rotor diameter is 19 m. The tilt is 5◦ . There are two gears with rotor rotational speeds of 36.6 and 47.9 rpm. For wind speeds exceeding 6 m/s second gear is activated. The rotor rotates anti clockwise when viewed from upwind location. The tower height is 29.18 m. The reference mast (MM2) is situated 36 m from the test turbine in a westerly direction. This mast is 33 m high and equipped with wind speed and wind direction sensors in various heights to supply mean wind speed data as well as instantaneous wind direction data that can be suitably averaged to filter away the fast fluctuating part of the wind direction signal associated with the small scale turbulence. The older reference mast (MM1) is situated 114 m from the test turbine in a north-western direction, considered too far away to be useful in this experiment, other than rainfall measurement.

A second turbine, Nordtank 500 kW, is placed approximately 70 m north of the test turbine. The hub height is 36 m, and the rotor diameter is 41 m. This turbine is not a part of the experiment, but its wake interferes with our experiment for certain wind directions. The positions of the turbines and the meteorological masts at the site are shown in Figure 3. The data from turbines and meteorological masts are collected into one single synchronized MySQL database to facilitate data analysis. The combined database includes 17 channels of data originating from three different measuring campaigns in May 2005, November 2005 and February 2006, respectively. The signals are recorded using up to four synchronized measurement PCs.

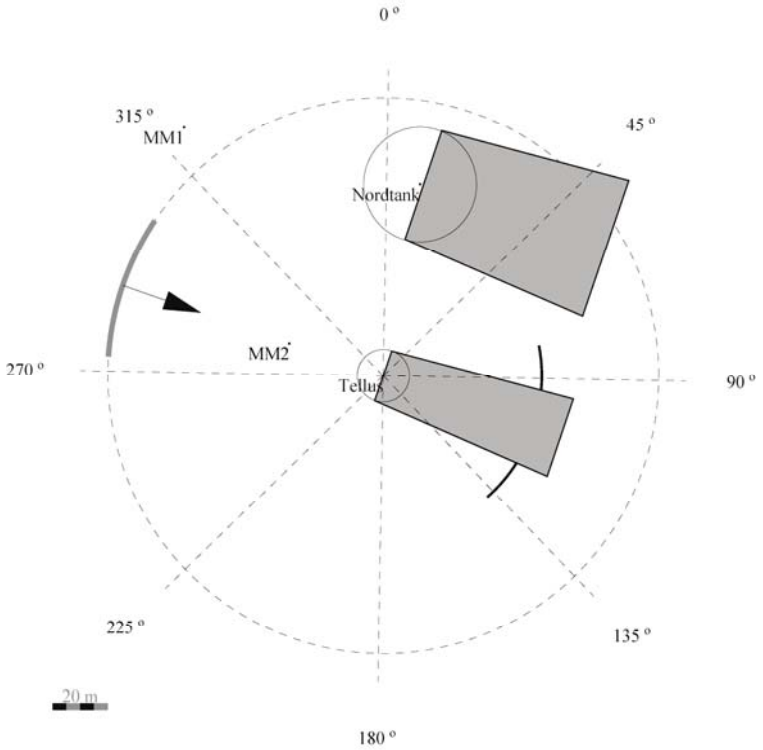

Figure 3: Shown are the positions of the two masts (MM1 and MM2) and two wind turbines (Nordtank and Tellus). Gray arc on the left denotes the selected wind direction sector. All represented data in this paper are from this sector while the Tellus nacelle position is in the same direction. The sector is 30◦ wide, between 274◦ and 304◦ , thus centering the primary reference mast, MM2. The gray with black edge area behind the Tellus is the possible wake width up to 70 m downstream according to the N. O. Jensen wake model [15] likewise for the

Nordtank wake. Black arc on the right behind the Tellus turbine is the example lidar Line Scan measurement at 58 m focus distance.

7. Results

The first data of Line and Deep Line Scanning modes has been collected in 2005. The wake behind the wind turbine is observed as illustrated in Figure 4. Four focus distances have been selected, and from each station nearly 300 data points are collected corresponding to 2.5 seconds.

In the closest focus distance all measurements are within the wake, but further downstream the wake as well as the undisturbed wind on the sides of the wake can be seen. At the end of 2005, after the mast MM2 was erected, it was possible to test the wake meandering hypothesis with synchronized wake and reference data. Each 10 minutes of Line Scan data are put into a density plot side-by-side in gray scale (Figure 5) indicating the measured wind speed. The light grey areas are high wind speeds, whereas dark areas are low wind speeds. The red line is the model prediction of the wake deficit position based on the spatially averaged instantaneous inflow direction. This direction is the average from the three wind vanes on the MM2 minus the measured orientation of nacelle, e.g. the yaw position.

With the selected data and model representation, it is easy to see the wake movements as well as the correlation between the predicted instantaneous wake position and measured instantaneous wake position. The model of the wake dynamics assumes the wake deficit to be advected in the mean wind direction with the mean wind speed and advected in the lateral direction with the large scale lateral turbulence component [7]. Assuming Taylor's hypothesis, the "driving" lateral velocities are perfectly correlated with the filtered wind direction measurements at the reference meteorological mast, however, delayed with the transportation time from the mast to the downstream point of interest. Thus, for the present case, where the meteorological mast is 36 m upstream the turbine, the expected delay is the time for an air parcel to move 36 m plus the focus distance. The delay has been calculated as the sum of two contributions. The first contribution is the time for an air parcel to travel the 36 m from the reference mast to the position of the Tellus turbine. For this contribution the transportation velocity is taken as the free mean wind speed. The second contribution is the time for an air parcel to move from the turbine to the downstream focus distance. The associated transportation velocity is taken as the reduced wind speed behind the turbine as based on the N. O. Jensen wake model [15]. Notice that this is not strictly in accordance with the passive scalar hypothesis, but the introduction of a reduced velocity increased the correlation between the measured wake position and the modelled.

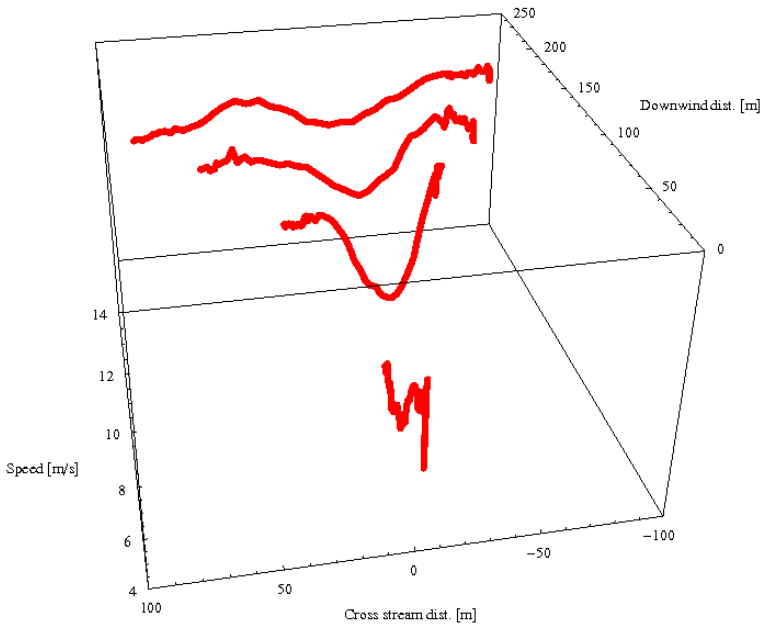

Figure 4: Deep Line Scan; data is collected from four different focus distances ranging from 1 rotor diameter to 9 rotor diameter (19 m, 76 m, 130 m and 176m). The initial wake is of the same size as the rotor and widens gradually downstream.

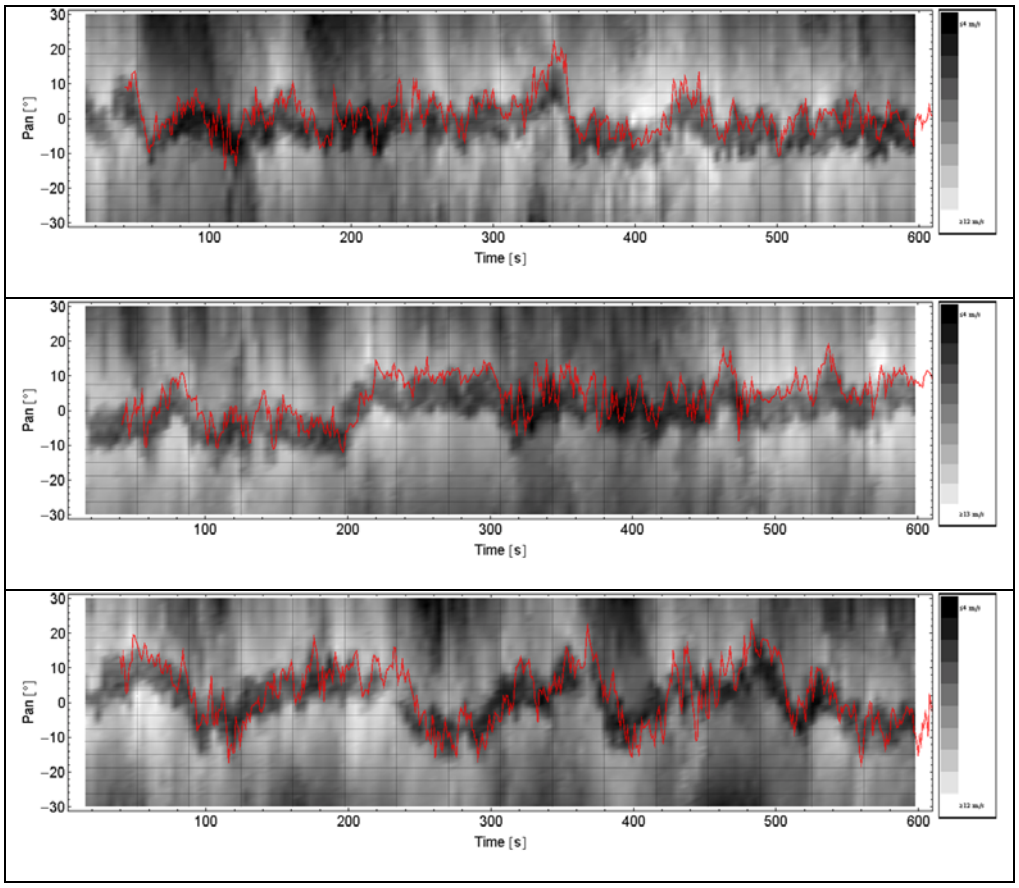

Figure 5: Line Scan data plotted in gray scale as function of time. Rotor diameter is 19 m. Low wind speed is shown as black and higher wind speed is shown as white. Focus distance is 3 diameters (58 m). The red line is the model prediction of the wake deficit position based on the spatially averaged instantaneous inflow direction. This direction is the average from the three wind vanes on the MM2 minus the measured orientation of nacelle. The ten minutes data are from 2005-Nov-15.

8. Conclusion

We have developed a new measurement technique that allows both for a 1D and a 2D scanning of the instantaneous longitudinal wake velocity. Using this technique, we resolve the wake expansion in the moving frame of reference as well as the movements of the wake coordinate system.

Resolving the wake meandering dynamics allowed us to verify a basic assumption for dynamic wake modelling – i.e. that the wake deficit is advected passively by the larger than rotor size eddies in the inflow. We do not see the self induced meandering reported in some situations in [2], only meandering attributed to ambient large scale turbulence. The reason for the difference is probably that the thrust coefficient in the wind tunnel experiments by [2] is much larger than in our full scale experiment. The present initial investigations support the passive scalar hypothesis for the investigated turbine except that the advection speed is a bit less than the speed of the ambient air.

Acknowledgement

This chapter has been written based on the journal article "Lidar Measurements of Wake Dynamics Part I: One Dimensional Scanning" [16]. More detailed information about the experimental setup can be found in refered article. The project is supported by the Danish Energy Agency grant under the project "Dynamic Wake Model for detailed aeroelastic Simulations of Wind Turbines in Farms" (33030-004) and was funded in part by the European Commission in the framework of the Non Nuclear Energy Programme Sixth Framework, Contract TREN07/FP6EN/S07.73680/038641 (TOPFARM - NextGeneration Design Tool For Optimisation Of Wind Farm Topology And Operation).

References

[1] Barthelmie, R. J., Folkerts, L., Rados, K., Pryor, S. C., Larsen, G. C., Frandsen, S. T.,Lange, B., and Schepers, G. Comparison of wake model simulations with offshore windturbine wake profiles measured by SoDAR. J. Atmos. Ocean. Technol. 23, 7 (July 2006),888–901.

[2] Medici, D., and Alfredsson, P. H. Measurements behind model wind turbines: Further evidence of wake meandering. Wind Energy 11, 2 (2008), 211–217.

[3] Vermeer, L. J., Sørensen, J. N., and Crespo, A. Wind turbine wake aerodynamics. ProgressIn Aerospace Sciences 39, 6-7 (Aug-Oct 2003), 467–510.

[4] Antoniou, I., Jørgensen, H. E., Mikkelsen, T., Frandsen, S. T., Barthelmie, R. J., Perstrup, C., and Hurtig, M. Offshore wind profile measurements from remote sensing instruments. In European Wind Energy Conference and Exhibition / Athens - Greece (2006).

[5] Smith, D. A., Harris, M., Coffey, A. S., Mikkelsen, T., Jørgensen, H. E., Mann, J., and Danielian, R. Wind lidar evaluation at the Danish wind test site Høvsøre. Wind Energy 9, 1-2 (Jan-Apr 2006), 87–93.

[6] Courtney, M., Wagner, R., and Lindel¨w, P. Testing and comparison of lidars for profile and turbulence measurements in wind energy. IOP Conference Series: Earth and Environmental Science 1 (2008), 012021 (14pp).

[7] Larsen, G. C., Madsen, H. A., Thomsen, K., and Larsen, T. Wake meandering – a pragmatic approach. Wind Energy 11 (2008), 377–395.

[8] Mann, J., Dellwik, E., Bingöl F., and Rathman, O. Laser measurements of flow over a forest. IOP Conference Series: Earth and Environmental Science 1 (2008), 012050 (5pp).

[9] Antoniou, I., Jørgensen, H. E., Mikkelsen, T., Petersen, T. F., Warmbier, G., and Smith, D. Comparison of wind speed and power curve measurements using a cup anemometer, a lidar and a sodar. In European Wind Energy Conference and Exhibition / UK (November 2004), EWEC, p. 47–51.

[10] Bingöl, F. Adapting laser Doppler anemometer into wind energy. Master's thesis, Technical University of Denmark, 2005. MEK-FM-EP 2005-02.[11] Harris, M., Hand, M., and Wright, A. Lidar for Turbine Control. Tech. Rep. NREL/TP-500-39154, National Renewable Energy Laboratory, 2005 Wind Energy

[11] Bingöl F., Mann, J., and Foussekis, D. Lidar error estimation with WAsP Engineering. IOP Conference Series: Earth and Environmental Science 1 (2008), 012058 (9pp).

[12] Trujillo, J. J., Bingöl F., Mann, J., and Larsen, G. C. Lidar measurements of wake dynamics, Part II : Two dimensional scanning. Wind Energy (2008). Submitted for publication as second part of this paper.

[13] Vestas. Vedligeholdelsesmanual. Tech. rep., DWT, 1995.

[14] Jensen, N. O. A note on wind generator interaction. Tech. Rep. Risø-M-2411, Risø National Laboratory, 1984. http://www.risoe.dk/rispubl/vea/veapdf/ris-m-2411.pdf.

[15] Bingöl F., Mann, J., and Larsen, G. C. Lidar Measurements of Wake Dynamics Part I: One Dimensional Scanning Wind Energy (2008) Volume 13, Issue 1, pages 51–61, January 2010 doi:10.1002/we.352

2.8 Lidar and wind profile

Alfredo Peña

1. Introduction

Wind lidars are originally made for the observation of the vertical wind speed profile. The ZephIR continuous wave (cw) lidar was the first wind lidar which measured wind speed and direction profiles up to 200 m AGL avoiding the flow distortion effects that the traditional instruments suffer when mounted on structures. The wind speed performance of the ZephIR compared to cup anemometers at several heights up to about 100 m showed high agreement ($R^2 \approx 1$ and slopes of linear regressions close to 1) from first studies over land [1] and over the sea [2].

Cup anemometer wind speeds were combined with ZephIR measurements at Nysted [3] and at Horns Rev [4] to reproduce offshore wind profiles up to ≈ 160 m AMSL. Although the campaign at Horns Rev showed good agreement with the theory, measurement range limitations were found due to the contamination of the lidar's Doppler spectra by clouds, resulting later in cloud correction algorithms.

Since wind profile retrieval within 30--200 m, where large wind turbines operate, is of great interest, cloud, fog and mist contamination is a serious concern. Therefore, the role of the aerosol profile on the lidar's probe volume has become more important, particularly its influence on the wind shear.

Pulsed lidars, like the WindCube and Galion, offer instantaneous wind profile observation up to ≈ 200 m, but the range depends on the amount of aerosols in the atmosphere, which is proportional to the signal-to-noise ratio (SNR). [5] described the neutral wind profile and [6] the diabatic wind profile, both for homogenous and flat terrain up to 300 m AGL, using WindCubes to extend wind observations from cup and sonics at Høvsøre, Denmark.

2. Wind profile theory

Mixing-length theory introduced by [7] is here chosen for modeling the local wind shear $\partial U / \partial z$ as,

$$\frac{\partial U}{\partial z} = \frac{u_*}{l} \tag{1}$$

where U is the mean horizontal wind speed, z the height above the ground, u_* the local friction velocity and l the local mixing length.

Surface layer

In the surface layer, covering $\sim 5-10\%$ of the atmospheric boundary layer (ABL), the surface-layer mixing length l_{SL} is given as,

$$l_{SL} = \kappa z \phi_m \tag{2}$$

where κ is the von Kármán constant (≈ 0.4) and ϕ_m the dimensionless wind shear from Monin-Obukhov similarity theory (MOST) [8], defined as,

$$\phi_m = \frac{\kappa z}{u_{*_o}} \frac{\partial U}{\partial z} \tag{3}$$

where u_{*_o} is the surface-layer friction velocity. ϕ_m varies for unstable and stable conditions, respectively, as,

$$\phi_m = (1 - az/L)^p \tag{4}$$

$$\phi_m = 1 + bz/L \tag{5}$$

where a, b and p are empirical constants ([9];[10]) and L is the Obukhov length,

$$L = -\frac{u_{*o}{}^3 T_o}{\kappa g \overline{w'\Theta_v{}'}_o} \tag{6}$$

where T_o is the mean surface-layer temperature, g the gravitational acceleration and $\overline{w'\Theta_v{}'}_o$ the surface-layer kinematic virtual heat flux. Assuming $u_* = u_{*o}$ and $l = l_{SL}$ in Eq. (1) and combining it with Eqs. (2) and (3), the integration with height of Eq. (1) gives the surface-layer wind profile,

$$\frac{U}{u_{*o}} = \frac{1}{\kappa}\left[\ln\left(\frac{z}{z_o}\right) - \psi_m\right] \tag{7}$$

where z_o is the surface roughness length and ψ_m is the diabatic correction of the wind profile, derived from the integration of ϕ_m [11]. For neutral conditions $\phi_m = 1$ and $\psi_m = 0$, resulting in the well-known logarithmic wind profile.

Figure1 illustrates the average dimensionless wind profiles observed for different stabilities over flat and homogenous terrain at Høvsøre. Each average wind profile is computed by classifying the individual 10-min wind profiles into stability classes, based on L as performed in [12] and [6]. Eq. (7) fits well the observations in the surface layer and the observations start to departure from the surface-layer wind profile at ~ 100 m for near-neutral conditions and ~ 60 m for very stable conditions.

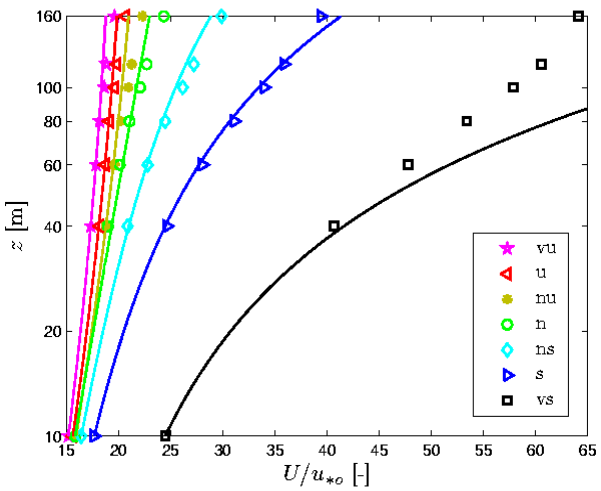

Figure 1 Wind profiles for different stability classes at Høvsøre. Markers indicate the observations and solid lines the predictions using Eq. (7). Legend: vu (very unstable), u (unstable), nu (near unstable), n (neutral), ns (near stable), s (stable), and vs (very stable).

The wind profile is a function of z_o and z/L only. In the surface layer and over flat and homogenous land, Eq. (7) fits well the average observations and the wind profile can easily be studied because z_o does not vary significantly. However, the boundary-layer height z_i starts to play a more important role as the height increases.

Marine surface layer

z_o over water is not constant and mainly depends on wind stress, waves, and fetch. The scaling U / u_{*o} was for constant z_o values. Using the simple parametrization of [13],

$$z_o = \alpha_c \frac{u_{*o}^2}{g} \tag{8}$$

where α_c is the Charnock's parameter (≈ 0.012), the scaling U / u_{*o} produces wind profiles that do not converge onto a straight line. [14] then suggested the following scaling for the marine wind profile,

$$\frac{U}{u_{*o}} + \frac{1}{\kappa} \ln\left[1 + 2\frac{\Delta u_{*o}}{\overline{u_{*o}}} + \left(\frac{\Delta u_{*o}}{\overline{u_{*o}}}\right)^2\right] = \frac{1}{\kappa}\left[\ln\left(\frac{z}{\overline{z_o}}\right) - \psi_m\right] \tag{9}$$

where $\Delta u_{*o} = u_{*o} - \overline{u_{*o}}$, i.e. Δu_{*o} is a *fluctuating* surface-layer friction velocity equal to the difference between the observation u_{*o} and the ensemble average $\overline{u_{*o}}$. $\overline{z_o}$ is a mean roughness length parameterized as Eq. (8), but replacing u_{*o} with $\overline{u_{*o}}$. Eq. (9) differs from Eq. (7), because it adds a dimensionless wind speed, the left term in square brackets in Eq. (9), allowing the wind profiles to converge onto a straight line for the same stability class.

Boundary layer

The surface-layer wind profile was derived assuming an infinitively growing length scale. At ~ 100 m AGL, this assumption might not be valid. There are many suggestions for l in the ABL. [15] and [16] limited the growth of l and proposed neutral mixing-length models, used to numerically compute the ABL wind profile. [17] proposed a similar model to that of [15], but in which l decreases slowly beyond the surface layer. [12] proposed a model, which assumes that the top of ABL acts as the ground and l has a zero value at that ABL level.

Analytical models for the ABL wind profile can be derived by integrating with height Eq. (1). This was performed by [12] and [6] for the diabatic flow over flat land and homogeneous terrain, [18] for diabatic flow over the sea, and [19] for neutral flow over flat and homogeneous land.

3. Comparison with observations at great heights

Marine observations

Cup and ZephIR combined measurements up to 161 m AMSL, within a sector where the upstream flow is free and homogeneous at the Horns Rev wind farm, were compared to wind profile models in [18] showing good agreement. The neutral and unstable wind profile models are identical to those used for the surface layer, Eq. (7). For the stable wind profile, a correction is applied to the stability parameter to take into account z_i:

$$\frac{U}{u_{*o}} = \frac{1}{\kappa}\left[\ln\left(\frac{z}{z_o}\right) - \psi_m\left(1 - \frac{z}{2z_i}\right)\right] \tag{10}$$

Figure 2 illustrates the results using the scaling proposed in [14].

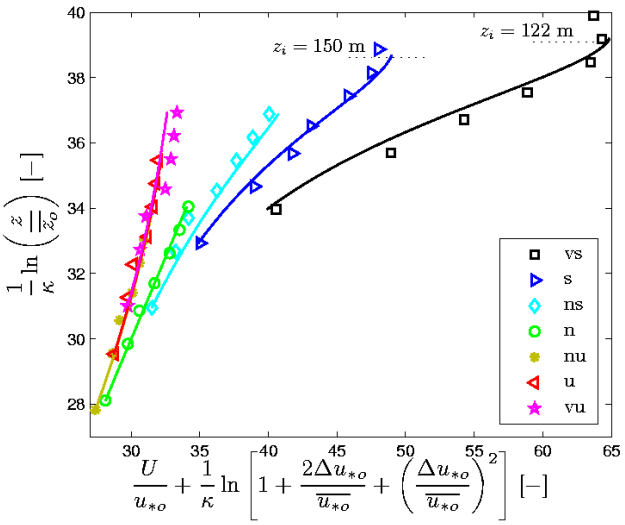

Figure 2 Wind profiles for different stabilities from combined lidar/cup observations at the Horns Rev wind farm. Markers indicate the observations and solid lines the predictions using Eq. (7) for unstable and neutral conditions and Eq. (10) for stable conditions.

The stable z_i was estimated in [18] by use of the [20] formula,

$$z_i = C\frac{u_{*o}}{|f_c|} \tag{11}$$

where C is a constant (≈ 0.15) and f_c is the Coriolis parameter. Eq. (11) is valid for neutral conditions only, so for stable conditions a lower C is used.

Neutral observations over flat land

Near-neutral wind speed cup/WindCube combined observations up to 300 m AGL, within an homogenous upwind sector at Høvsøre, were compared in [19] to a set of neutral wind profile models:

$$U = \frac{u_{*o}}{\kappa}\ln\left(\frac{z}{z_o}\right) \tag{12}$$

$$U = \frac{u_{*o}}{\kappa}\left[\ln\left(\frac{z}{z_o}\right) + \frac{1}{d}\left(\frac{\kappa z}{\eta}\right)^d - \left(\frac{1}{1+d}\right)\frac{z}{z_i}\left(\frac{\kappa z}{\eta}\right)^d - \frac{z}{z_i}\right] \tag{13}$$

$$U = \frac{u_{*o}}{\kappa}\left[\ln\left(\frac{\sinh(\kappa z/\eta)}{\sinh(\kappa z_o/\eta)}\right) - \frac{z}{z_i}\frac{\kappa z}{2\eta}\right] \tag{14}$$

$$U = \frac{u_{*o}}{\kappa}\left[\ln\left(\frac{z}{z_o}\right) + \frac{z}{l_{MBL}} - \frac{z}{z_i}\left(\frac{z}{2l_{MBL}}\right)\right] \tag{15}$$

which correspond to the logarithmic wind profile, an analytical solution from the mixing-length model of [15] ($d = 1$) and [17] ($d = 5/4$), a solution using the mixing-length model of [16], and the model of [12], respectively. d controls the growth of l, η is the limiting value for l in the upper atmosphere, and l_{MBL} is a middle boundary-layer length scale.

η has been parameterized as $\eta = D\dfrac{u_{*o}}{|f_c|}$, where [15] suggested $D = 63\times10^{-4}$ and from the analysis of [17] and assuming $\mathrm{Ro} = 5.13\times10^{5}$, where Ro is the surface Rossby number, $D = 96\times10^{-4}$. Then, combining η's definition above with Eqs. (12)--(15), the ratio $u_{*o}/|f_c|$ can be replaced by z_i/C from Eq. (11). l_{MBL} was parameterized by [12] based on observations at Høvsøre. The results are illustrated in Figure 3. The models have a better agreement with the observations beyond the surface layer (~ 80 m). The logarithmic wind profile fits well the measurements within the surface layer only.

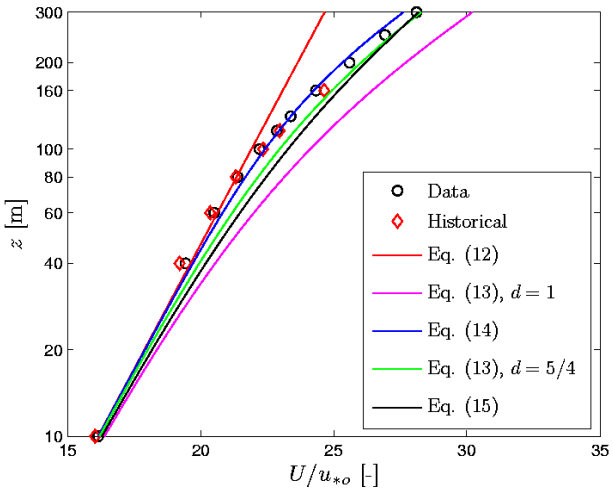

Figure 3 Neutral wind profile at Høvsøre. Markers indicate combined lidar/cup observations (Data) and the mean wind profile from about 3 years of cup observations (Historical). Solid lines indicate the predictions using C=0.15, $D = 73\times10^{-4}$, 58×10^{-4}, and 100×10^{-4} for Eq. (13) with d=1, Eq. (14), and Eq. (13) with d=5/4, respectively.

Diabatic observations over flat land

Combined cup/Windcube measurements up to 300 m AGL, within an homogenous upwind sector and for different stabilities at Høvsøre, were compared in [6] to diabatic wind profile models. These were derived by extending the surface-layer length scale of the mixing-length models of [15], [17], and [12] to account for stability using MOST. For example, using the models of [15] and [17], the wind profile is given as,

$$U = \frac{u_{*o}}{\kappa}\left[\ln\left(\frac{z}{z_o}\right) - \psi_m + \frac{1}{d}\left(\frac{\kappa z}{\eta}\right)^d - \left(\frac{1}{1+d}\right)\frac{z}{z_i}\left(\frac{\kappa z}{\eta}\right)^d - \frac{z}{z_i}\right] \tag{16}$$

$$U = \frac{u_{*o}}{\kappa}\left[\ln\left(\frac{z}{z_o}\right) + b\frac{z}{L}\left(1 - \frac{z}{2z_i}\right) + \frac{1}{d}\left(\frac{\kappa z}{\eta}\right)^d - \left(\frac{1}{1+d}\right)\frac{z}{z_i}\left(\frac{\kappa z}{\eta}\right)^d - \frac{z}{z_i}\right] \tag{17}$$

for unstable and stable conditions, respectively.

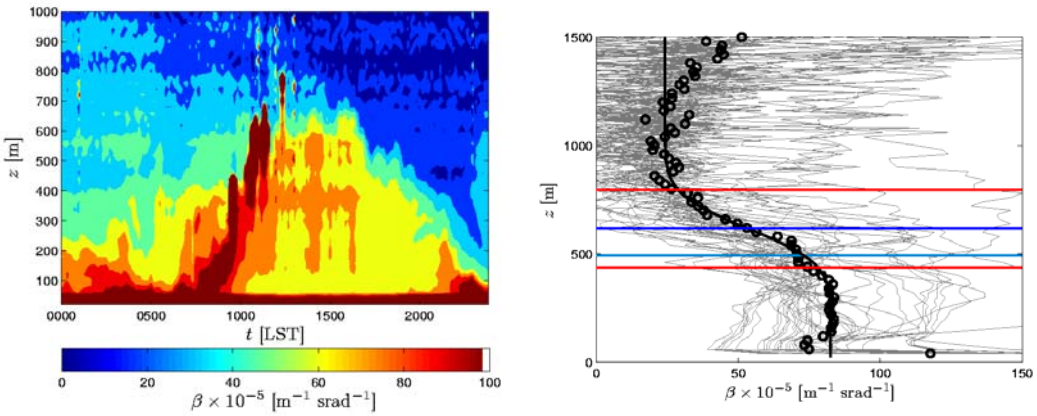

Figure 4 Left: Ceilometer observations of the aerosol backscatter coefficient β during a convective day at Høvsøre. Right: Aerosol backscatter profile from ceilometer measurements at Høvsøre for neutral conditions. The gray lines show the aerosol profiles, the markers the average aerosol profile, the black line the fit function from [21], and the horizontal lines the estimation of z_i from the fit function (blue), the entrainment zone depth (red lines), and the estimation of z_i from Eq. (11) (cyan).

η was parameterized in [6] using Rossby-number similarity as,

$$\eta = \frac{\kappa z_i}{\left[d(1+d)\right]^{1/d}}\left[\left(\left[\ln\left(\frac{u_{*o}}{f_c z_o}\right) - A\right]^2 + B^2\right)^{1/2} + 1 - \ln\left(\frac{z_i}{z_o}\right)\right]^{-1/d} \quad (18)$$

where A and B are the integration constants. z_i was estimated from Eq. (11) for neutral and stable conditions and from observations of the aerosol backscatter coefficient from a Vaisala CL31 ceilometer for unstable conditions. Figure 4 (left) illustrates the behavior of the aerosol backscatter coefficient β during a day where most of the unstable profiles were measured. During daylight time (1000--1800 LST), the aerosols reached 600--700 m marking the unstable z_i. In [6], aerosol backscatter profiles observed simultaneously with the wind profiles for each stability class are used to estimate z_i. The results for the neutral stability class are illustrated in Figure 4 (right). z_i is estimated using the modified error function suggested by [21] and good agreement was found when compared to the estimation from Eq. (11) for neutral conditions.

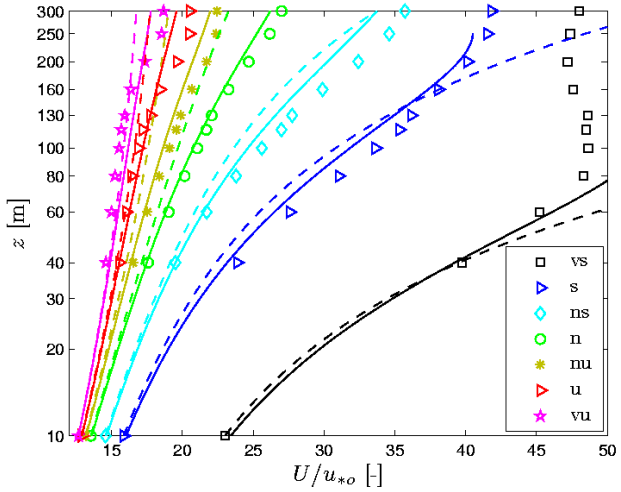

Figure 5 Wind profiles observed for different stability classes at Høvsøre, Denmark. The markers indicate the combined lidar/cup anemometer observations, the solid lines the predictions using Eqs. (16) and (17) with d=5/4, and the dashed lines the predictions from Eq. (7). Legend as in Fig. 1.

Figure 5 illustrates the comparison of the models in Eqs. (16) and (17) with *d=5/4*, the surface-layer wind profile, Eq. (7), and the wind speed observations for the number of stabilities also used in Figures 1 and 2. As with the neutral observations, surface-layer scaling fits well the observations within the surface layer only. The wind profile model, which limits the value of the length scale, corrects for the departures of the observations beyond the surface layer. Similar results were obtained in [6] using Eqs. (16) and (17) with *d=1* and the wind profile models in [12].

4. Summary and Conclusions

- Ground-based remote sensing instruments are useful for the study of the wind profile in and beyond the surface layer and for the improvement of the meteorological models.
- Over flat land and homogenous terrain and over the sea, the surface-layer wind profile fits well the observations for a wide range of stabilities within the surface layer only. For the analysis of wind profiles over water a new scaling should be added in order to account for the variable z_o.
- Combined lidar/cup measurements up to 160 m AMSL at the Horns Rev offshore wind farm are well predicted by wind profile models that limit the value of the length scale where the z_i becomes an important parameter.
- Near-neutral combined lidar/cup measurements up to 300 m AGL at Høvsøre departure from the logarithmic wind profile beyond the surface layer. Simple analytical models, which limit the value of the length scale, predict such departure and fit well the observations.
- Wind profile models, extended for diabatic conditions, are compared to combined lidar/cup measurements up to 300 m AGL at Høvsøre for a number of stabilities. The models, which limit the growth of the length scale, agree better with the observations compared to the surface-layer wind profile, which under- and over-predicts the wind speed beyond the surface layer. The models also depend on z_i, estimated under neutral and stable conditions using surface-layer turbulence measurements and under unstable conditions using ceilometer observations of the aerosol backscatter profile.

References

[1] Smith D. A., Harris M., Coffey A. S., Mikkelsen T., Jørgensen H. E., Mann J., and Danielian R. (2006) Wind lidar evaluation at the Danish wind test site in Høvsøre. Wind Energy 9:87—93

[2] Kindler D., Oldroyd A., MacAskill A., and Finch D. (2007) An eight month test campaign of the QinetiQ ZephIR system: Preliminary results. Meteorol. Z. **16**:479—489

[3] Antoniou I., Jørgensen H. E., Mikkelsen T., Frandsen S., Barthelmie R., Perstrup C., and Hurtig M. (2006) Offshore wind profile measurements from remote sensing instruments. Proc. of the European Wind Energy Conf., Athens

[4] Peña A., Hasager C. B., Gryning S.-E., Courtney M., Antoniou I., Mikkelsen T. (2009) Offshore wind profiling using light detection and ranging measurements. Wind Energy **12**:105—124

[5] Peña A., Gryning S.-E., Mann J., and Hasager C. B. (2010b) Length scales of the neutral wind profile over homogeneous terrain. J. Appl. Meteorol. Climatol. DOI:10.1175/2009JAMC2148.1

[6] Peña A., Gryning S.-E., and Hasager C. B. (2010a) Comparing mixing-length models of the diabatic wind profile over homogeneous terrain. Theor. Appl. Climatol. **100**: 325—335

[7] Prandtl L. (1932) Meteorologische Anwendung der Strömungslehre (Meteorological application of fluid mechanics) Beitr. Phys. Atmos **19**:188—202

[8] Monin A. S. and Obukhov A. M. (1954) Osnovnye zakonomernosti turbulentnogo peremeshivanija v prizemnom sloe atmosfery (Basic laws of turbulent mixing in the atmosphere near the ground). Trudy Geofiz. Inst. AN SSSR **24**(151):163—187

[9] Businger J. A., Wyngaard J. C., Izumi Y., and Bradley E. F. (1971) Flux-profile relationships in the atmospheric surface layer. J. Atmos. Sci. **28**:181—189

[10] Högström U. (1988) Non-dimensional wind and temperature profiles in the atmospheric surface layer: a re-evaluation. Bound.-Layer Meteorol. **42**:55—78

[11] Stull R. B. (1988) An introduction to boundary layer meteorology, Kluwer Academic Publishers, 666 pp

[12] Gryning S.-E., Batchvarova E., Brümmer B., Jørgensen H., and Larsen S. (2007) On the extension of the wind profile over homogeneous terrain beyond the surface layer. Bound.-Layer Meteorol. **124**:251—268

[13] Charnock H. (1955) Wind stress over a water surface. Quart. J. Roy. Meteorol. Soc. **81**:639—640

[14] Peña A. and Gryning S.-E. (2008) Charnock's roughness length model and non-dimensional wind profiles over the sea. Bound.-Layer Meteorol. **128**:191—203

[15] Blackadar A. K. (1962) The vertical distribution of wind and turbulent exchange in a neutral atmosphere. J. Geophys. Res. **67**:3095—3102

[16] Panofsky H. A. (1973) Tower Micrometeorogy. Haugen D. A. (Ed.) Workshop on Micrometeorolgy. American Meteorology Society, 151—176

[17] Lettau H. H. (1962) Theoretical wind spirals in the boundary layer of a barotropic atmosphere. Beitr. Phys. Atmos. **35**:195—212

[18] Peña A., Gryning S.-E., and Hasager C. B. (2008) Measurements and modelling of the wind speed profile in the marine atmospheric boundary layer. Bound.-Layer Meteorol. **129**:479—495

[19] Peña A., Gryning S.-E., Mann J., and Hasager C. B. (2010b) Length scales of the neutral wind profile over homogeneous terrain.J. Appl. Meteorol. Climatol. DOI: 10.1175/2009JAMC2148.1

[20] Rossby C. G. and Montgomery R. B. (1935) The layers of frictional influence in wind and ocean currents. Pap. Phys. Oceanogr. Meteorol. **3**(3):101 pp

[21] Steyn D. G., Baldi M., and Hoff R. M. (1999) The detection of mixed layer depth and entrainment zone thickness from lidar backscatter profiles. J. Atmos. Ocean. Technol. **16**:953--959

2.9 Windscanner

Torben Mikkelsen, Mike Courtney and Jakob Mann

1. Introduction

It is a scientific challenge to measure and understand the three-dimensional and time varying wind field as it passes through and interacts with the huge rotor of a modern wind turbine. Using traditional wind measurements made by anemometers mounted on meteorological masts, it is practically impossible to acquire the necessary 3-D wind information. Our present comprehension of the turbulent wind flow and its interaction with wind turbines is correspondingly limited.

A windscanner is a new measurement technology developed within the WindScanner Research Infrastructure development project and aiming at becoming a joint European Research In frastructure facility (ESFRI Road map uptake 2010). Built from sets of portable laser Doppler wind profilers, Windscanners can sense the 3D wind vector field at points 10-250 metres away at sampling rates up to 500 Hz.

2. Method

The wind Lidar (light detection and ranging) technology is already well-established in the wind energy field. Durable and sturdy wind lidars are now commercially available, built from standard fibre-based telecommunications components. This has brought down their size, power consumption and cost (available for around €200,000 each, perhaps less in the future). To be used as scanners, commercial wind lidar must be equipped with steerable scan heads, a technology that has been developed and patented recently by Risø DTU.

The WindScanner measurement technology is based on single (for homogeneous flow) or alternatively a tri-axial configuration. One to three laser beams are fired upwards and reflected by particles in the moving air. The Doppler Effect shifts the reflected laser beam's wavelength slightly and from this, the speed and direction of the wind vectors is deduced.

Figure 1: Tri-axial configuration wind scanner

For the single axis configuration, the basic principle is the same as for a commercial lidar but the scan head developed by Risø DTU allows much more complex scanning pattern for the laser beam resulting in a more detailed description of the wind field. For the case of the tri-axial configurations, three lidar units will be used simultaneously (see figure 1). The three units will be synchronized in order to get the laser beam to cross in a single measurement volume while scanning the air to describe the whole wind field.

Two types of wind scanner are currently developed in this project: a short-range WindScanner and a long-range WindScanner.

The *Short-range WindScanners* are powered by Natural Power ZephIR wind lidars and will measure 3D wind and turbulence fields at remote distances within the range 10-250 meters (see Figure 2).

Figure 2: Short Range WindScanner 2010

The *Long-range WindScanners are* powered by Leosphere Wind Cubes and will measure 3D flow and turbulence at ranges from 100 meters to 5 km (see Figure 3).

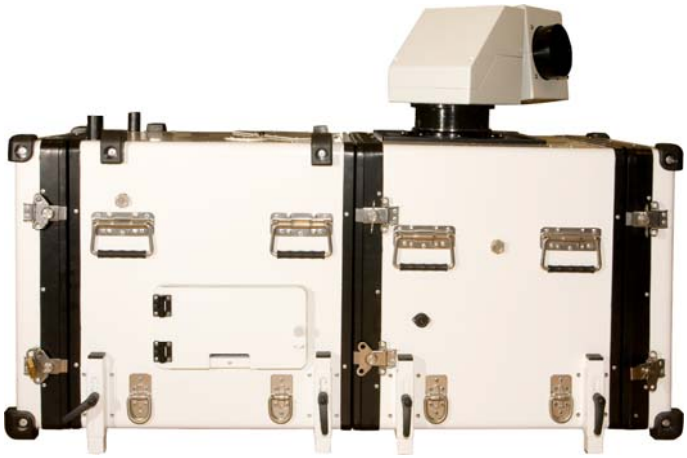

Figure 3: Long-Range WindScanner 2010

WindScanners can operate offshore from stable and floating platforms. The scientific questions addressed off shore will focus on turbulent shear created by individual turbines and turbine parks in order to assess the potential impact on additional turbines to be erected in the vicinity. It is essential to understand these issues in order to estimate the profitability of very large future offshore wind parks.

Furthermore, full-scale experimental research in 3D atmospheric wind and turbulence over complex terrain will be conducted.

3. Conclusions

The WindScanner research infrastructure under establishment at Risø DTU will enable measurements of 3D wind fields around large individual wind turbine rotors or within or behind wind turbine arrays and parks, both on and offshore.

It is designed to radically improve our ability to scan and measure the complex three-dimensional structure of wind fields in the real atmosphere, and consequently, improve our fundamental understanding of the complex geophysical flows characteristic of the turbulent wind fields surrounding wind turbines in the atmospheric boundary layer.

The main aim of the WindScanner is to provide new data and new insight that can by used to improve computer models used for designing and siting of wind turbines.

References

www.windscanner.dk**;** www.windscanner.eu

3 SoDAR

3.1 The Bistatic Sodar ”Heimdall”

Torben Mikkelsen, Hans E. Jørgensen and Leif Kristensen

1. Introduction

With the increased exploitation of wind energy, remote sensing of wind profiles in the atmospheric boundary layer has come in focus as an attractive alternative to the operation of tall instrumented masts for wind energy siting and assessment studies. Project “Heimdall” describes a feasibility study conducted at Risø in the period 2001-2003 of the investigation of a new continuous wave (CW) bi-static configured sodar, initiated with the aim of investigating and improving the measuring accuracy of sodar remote sensing at heights ranging between 50 and 150 meters, during the often strong wind conditions in a neutrally stratified atmospheric conditions, characteristic for wind energy applications.

The switching between transmitting and receiving for the monostatic sodar means that it is impossible to operate it in a continuous mode. For this instrument one duty circle consists of the transmitting a short sound pulse, followed by the receiving of the back-scattered returns. The distance to the traveling sound pulse is monitored by so-called range gating. In other words, a monostatic sodar sound pulse probes the atmosphere along the axis of the transmitter/receiver antenna. This is not the case for a bi-static sodar. A bi-static sodar has two or more base stations on the ground in order that the transmitter and the receiver are separated from one another. Here the atmosphere is probed in the rather limited vicinity of the intersection between the axes of the transmitter and the receiver. So far bi-static sodars have been operated in the same way as monostatic sodars, but with a bi-static operation it is possible to operate in a continuous mode.

2. Theoretical background

The cross section for sound scattering

The specific sound scattering cross section, i.e. the total cross section per unit solid angle and volume was derived by [1].Based on the notation consistent with [2], we evaluated this quantity in the case of isotropic turbulence

$$\eta(\gamma) = \frac{5}{9\Gamma(1/3)2^{17/3}} k^{1/3} \frac{\cos^2(\gamma)}{\sin^{11/3}(\gamma/2)} \left\{ \frac{C_T^2}{T^2} + \frac{22}{3} \frac{C_V^2}{c^2} \cos^2(\gamma/2) \right\}. \quad (1)$$

where k is the wavelength and γ the scattering angle.

According to (1), the scattering cross section pertaining to velocity fluctuations is zero for $\gamma = \pi = 180\circ$. In other words, there is not backscattering from velocity fluctuations. This means that monostatic sodars are useful only when there are temperature fluctuations. In situations with neutral temperature stratification the signal quality in a monostatic sodar is pure. The scattering from temperature fluctuations is zero only for $\gamma = \pi/2 = 90\circ$ for which the scattering from velocity fluctuations is also zero.

For a bi-static sodar with e.g. $\gamma \sim 135\circ$ both temperature and velocity fluctuations have about their maximum contribution to the total scattering cross section. This configuration will, all considered, give nearly the strongest possible return signal.

We see that there are two advantages in using a bi-static sodar:

1. The instrument can operate with a turbulence scattered return signal even when the atmosphere is neutrally stratified, because in general $\eta\_V > 0$ in this situation, and
2. It can be operated in a continuous mode, because the transmitter and the receiver are separated.

The bi-static sodar equation

Here we follow the approach in described [3], [4], and [5] to derive the *sodar equation* which tells how much acoustic energy is received by a microphone at a certain distance from a loud speaker.

A bi-static sodar consists of a transmitter T, which is a powerful loudspeaker, and a sound receiver R. They are located a certain distance 2*d* from one another. The monochromatic sound from T has a wavelength of about 20 cm or less and this means that just a few meters from T or R we are in the far-field zone where the sound pressure is inversely proportional to the square of the distance *r* from T or R (if the last is used as a speaker). However, the transmission and reception are not isotropic. Each are characterized by an angle ψ from the axis of T or R. If we let the emitted power be P_T then the power flux, per unit solid angle, from T at the distance *r* will be

$$F_T(r,\Psi) = \frac{P_T}{r^2} F_T(\Psi) e^{-\beta r} \quad (2)$$

where $F_T(\Psi)$ is the so-called directivity of the transmitter and β the attenuation coefficient (of the order of $\sim 10^{-3}\,\mathrm{m}^{-1}$).

The received power is a function of the total distance the sound has traveled from T to R. Calling this distance 2*a*, the attenuation is $\exp(-2a\beta)$.

The transmitter and the receiver are installed in such a way that they intersect in a vertical plane. In order to include the attenuation in the calculation of the power received by R, we look for the foci of points where the travel distance from T to R is the same, namely 2*a*. These foci are an axi-symmetric ellipsoid with the major half-axis *a* and the two half minor axes $(a^2 - d^2)^{1/2}$. The sodar equation obtained with these notations was used to determine the received power by R as a function of time when a short pulse was emitted from T. This is obtained by integrating over θ and φ and interpreting *a* as a measure of time, which is possible because the time *t* elapsed after the time of emission of the sound pulse t_0 is $t = 2a/c + t_0$ [3, 4, 5].

3. Instrument Description

The basic design of the Heimdall instrument is a sound transmitter and a sound receiver. They both have an antenna disk with identical geometry to direct and receive the sound from a rather confined spatial domain. The disks are designed to satellite reception and are almost circular, with the largest diameter equal to 1.2 m and the smallest a little less than 1 m. In the foci of these antenna disks there are a speaker and a microphone, respectively. The transmitter is shown in Fig. 1. The directivity of each antenna have a pronounced central main lobe and the nearest side-lobe at about 10◦ from the axis is reduced by a factor 0.0025 (26 dB) compared to the main lobe. We have not determined the directivity for our antenna disks but relied on measurements carried out on a similar disk by Handwerker (1999). The speaker is a 30 W electric-power Paso TR30-TW horn. The total power of sound is 1.58 W for 30 W electric-power input in the frequency range 1–2 kHz.

Figure 1. The Heimdall sodar transmitter at Risø. The speaker is located in the focus of the antenna disk.

This corresponds to about PT = 100 WSr^{-1}, i.e. the sound power per unit solid angle, in the direction of the axis (±15◦). The horn is operated with a sine-signal input in the range 2–4 kHz. The geometry of the receiver antenna R is identical to the transmitter T except that the horn is replaced by a sensitive microphone, Brüel&Kjær type 41451, including a 4669-c preamplifier with an adjustable gain at 9, 10, 20. . . 60 dB, and a Brüel&Kjær type 5935-1 power supply.

4. Results

The Heimdall sodar was tested adjacent to the Risø 123 m meteorological mast. The axis of the transmitter T was vertical while that of the receiver R has an inclination of $\pi/4$ in plane of the transmitter axis and the 60 m baseline between T and R. This configuration allows the velocity component in this plane at the height 60 m. The signal is sampled in consecutive periods of T = 1 s where each period was digitized with the digitization period $\Delta t = T / N = 2^{-14} \approx 6.1 \times 10^{-5}$ s , corresponding to the number $N = 214$ data points. Before the 32 bit FFT a Hanning window was applied. The highest frequency, the Nyquist frequency, is $2^{13} \approx 8.2 \times 10^{3}$ Hz . Using the smoothing option of the signal analyzer, the spectra, updated every second, were weighed exponentially backwards in time with a 10 s time constant. Figure 2 shows an example of a Doppler spectrum, zoomed into the interesting range. The transmitter frequency was in this case 3960 Hz which explains the pronounced narrow maximum at this frequency. The Doppler spectrum shows a narrow peak at the unavoidable transmitter frequency, which actually serves as the reference frequency, and a broad maximum. Its width is partly due to the turbulence inside the sampling volume at the intersection.

It is essential to separate the “real” Doppler spectrum due to the atmospheric scattering and the background. This background noise is large when the wind speed is high. Figure 3 shows an example of a background spectrum with no transmission from T. The wind speed is about 12–15 ms^{-1}.

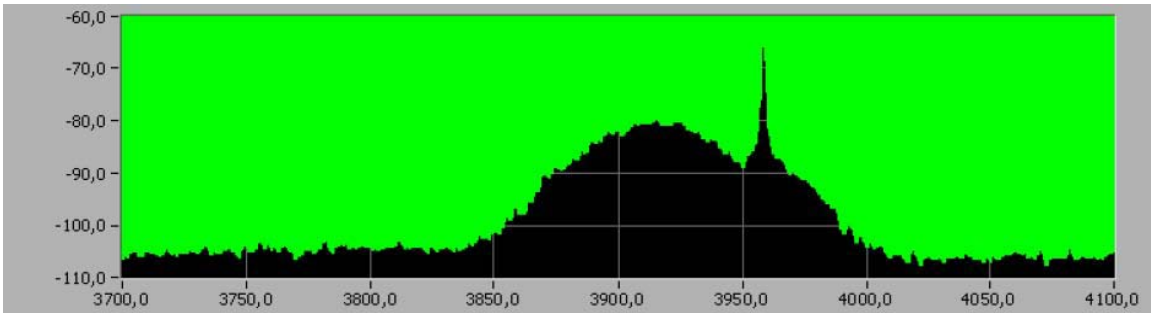

Figure 2. Doppler spectrum. The abscissa is the frequency in Hz and the ordinate the spectrum in dB units. The narrow peak at 3960 Hz is the directly transmitted frequency while the broad maximum centered at about 3910 Hz represents the velocity Doppler shift. Using (3) we find that this Doppler shift corresponds to about 6 ms^{-1}. The anemometer at the Risø mast at 60 m showed that the velocity component T-R plane was about 5 ms^{-1}.

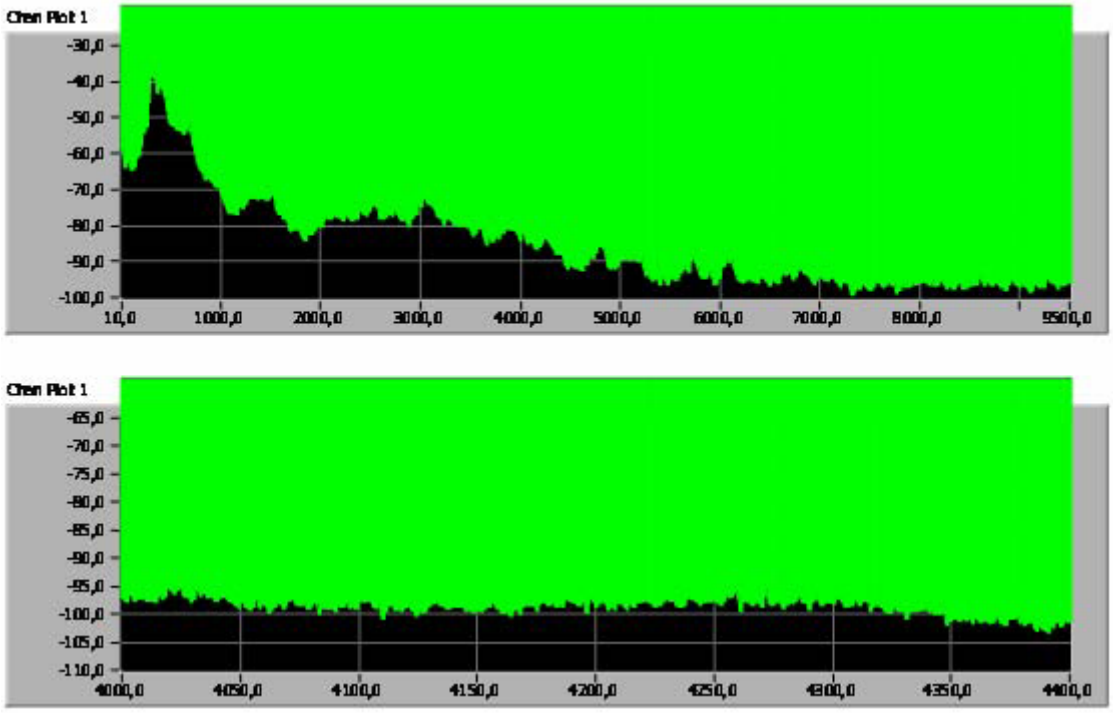

Figure 3. Noise spectra at wind speeds in the range 12–15 ms^{-1}. The top frame shows the recorded spectrum and the lower frame the same spectrum, zoomed in at the important frequency range.

5. Conclusions

We have demonstrated that it is possible to obtain measurements plane projections of velocity, continuous in time, by using a bi-static sodar. The plane is defined by the two axes of the transmitter T and the receiver R. We have tacitly assumed that this plane is vertical. However, this need not be the case. The scattering cross section (1) shows that turbulent fluctuations in both temperature and velocity contribute as scattering agents. The efficiency depends on the scattering angle γ. Neither the velocity nor the temperature fluctuations contribute for $\gamma = 90^\circ$ and at $\gamma = 180^\circ$ (backscattering) the velocity fluctuations are inactive. However we can make good use of both types of turbulent fluctuations by using $\gamma = 135^\circ$.

The Doppler velocity is obtained as a volume average, defined the intersection between the main lobes of the directivities of the transmitter T and the receiver R. The sodar equation (58) gives the power of the received signal as a function of the position of the scattering eddy in the elliptical coordinates a, φ, θ. We see that the sound attenuation parameter β enters at

this point. It has to be specified as a function of the surface-layer parameters T and RH and of the frequency. As we have seen, it is advantageous from a signal-strength point of view to have $\gamma = 135^{\circ}$. The Heimdall sodar was only realized as a single-component, single legged bistatic sodar, and it has not been tested thoroughly or used in practical operation. We have used the sodar equation to estimate the expected received power as a function of the transmitted power. Even though the received power was higher that the power expected from a nonostatic configuration, the measured power has an order of magnitude lower that the theoretically estimated power so, even considering the experimental uncertainties, this discrepancy seems unacceptable and requires a more thorough investigation. The inaccuracy of the received power does not in itself present a problem when determining Doppler shifts due to atmospheric motion. However, it is useful to be able to predict a realistic signal-to-noise ratio from the sodar equation. There are three major sources of noise:

1. The receiver gets a very strong signal at the transmitter signal frequency from direct transmission. Since it is essentially monochromatic this noise can easily be identified and, in fact, be used as a reference.

2. The receiver spectrum may contain a broad maximum due to scattering of side lobe sound. These are usually not as pronounced as the maximum due to the main lobe.

3. Strong winds create noise which is almost white in the frequency domain of interest. The noise increases with the wind speed.

The noise problems always make it a challenge to construct a reliable automated sodar system for wind speed determination which could be based on a digital technique as used here or an analogue technique like tracking of the spectral maximum by a phase-locked-loop circuit analyzer.

References

[1] Tatarskii, V. I. (1967), *The Effects of the Turbulent Atmosphere on Wave Propagation*, Israel Program for Scientific Translations, Jerusalem, Israel; National Technical Information Service No. TT 68-50464, U.S. Department of Commerce, Springfield, VA.

[2] Lumley, J. L. & Panofsky, H. A. (1964), *The Structure of Atmospheric Turbulence*, John Wiley & Sons, Inc., New York.

[3] Kristensen, L., Coulter, R. L. & Underwood, K. H. (1978), Sodar geometry, *in* 'Proc. Fourth Symp. on Meteorological Observations and Instrumentation', American Meteorological Society, Denver, CO, pp. 391–395.

[4] Kristensen, L. (1978), On sodar technigues, Technical Report R-381, Riso National Laboratory.

[5] Neff, W. D. & Coulter, R. L. (1986), Acoustic remote sensing, *in* D. H. Lenschow, ed., 'Probing the Atmospheric Boundary Layer', American Meteorological Society, Boston, MA, chapter 13, pp. 201–239.

4 Classic mast measurement technologies

4.1 Influence of flow distortion due to the mast on boom mounted cup anemometers

Petter Lindelöw-Marsden

1. Introduction

Cup anemometers mounted on booms experience flow distortion from the mast structure. These distortions affect the wind speed measurement. The effect of flow distortion due to the mounting boom and the tower was examined in the nineties [1,2] and guidelines based on flow modeling are available for example in the IEC standard for power performance measurements [3]. However, indications of underestimation of the flow distortion has recently been reported and correction and in-field calibration methods have been proposed [4,5].

2. Observations

The examined tower has an equilateral triangular cross-section. The western side of the tower is pointing at nominally 3°, with due north defined as 0. At 80 m height the sides are 1.9 m long and the three round legs have a diameter of 140 mm. The round cross-bracing have a diameter of 48 mm. The cross-bracing is made with a 23° angle from horizontal. The boom diameter is 50 mm and is fixed to the tower with two clamps with a 15 cm diameter. Two P2546A cup anemometers, IEC class 1.31A, are mounted on booms at 80 m height according to the IEC standard. The booms protrude 4.1 m from the tower. The booms are nominally pointing close to the south and east-south-east (ESE) direction, referred to as 183° and 123° with due north being 0°.

The ratio of the horizontal wind speed measurement taken by two cup anemometers pointing in different directions are seen in Figure . The cup ratio is not always centered round one. This phenomenon can be explained by the uncertainty in the cup calibration and can be taken into account by an in-field calibration

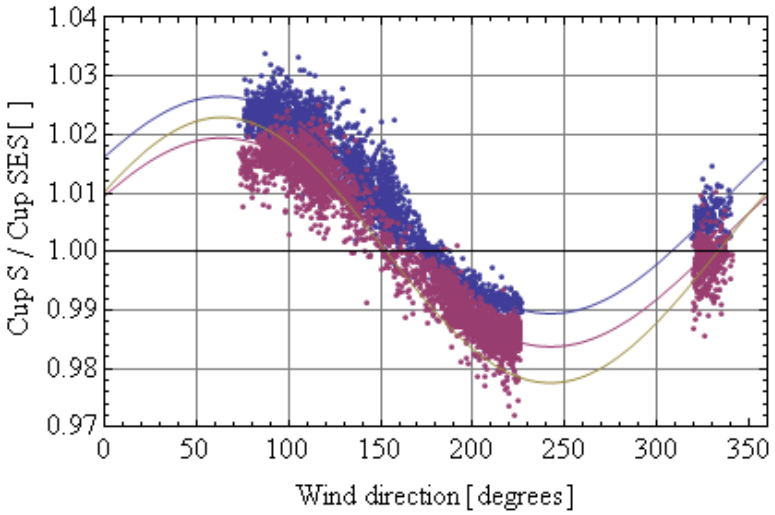

Figure 1 Cup ratio vs wind direction in the first, purple, and third period, blue. Also included is the fitted cup ratio obtained for the nominal boom directions taken from the geometric center. The green line shows the fitted cup ratio of the later data set without using in-field calibration.

3. Model

The model of the ratio of the wind speed measured by two cups can be expressed as

$$\frac{u_1}{u_2} = \frac{u + \Delta u_1}{u + \Delta u_2} = G_{diff} \frac{\left(1 - A\cos\left(\theta - \alpha_1 - \beta_1\right)\right)}{\left(1 - A\cos\left(\theta - \alpha_2 - \beta_2\right)\right)} \tag{1}$$

where u is the free horizontal wind speed, u_1 is the wind speed measured by one cup and u_2 is the wind speed measured by the other, G_{diff} is the relative gain difference between the two cup anemometers, A is the amplitude of the error due to tower flow distortion, θ is the wind direction, α is the offset relatively to the nominal direction β.

4. Results

The extracted parameters for three different sets of cups are shown in Table 1. The Amplitude of the flow distortion expected from the IEC standard is 1.1%.

Period	(α_1,α_2)	A [%]	G_{diff} []	$\frac{\sum res^2}{N}$
First	(10°,-1°)	1.53 ± 0.01	1.0007 ± 0.0001	$8.7 \cdot 10^{-6}$
Second	(12°,1°)	1.82 ± 0.01	1.0048 ± 0.0001	$8.4 \cdot 10^{-6}$
Third	(9°,-3°)	1.56 ± 0.02	1.0072 ± 0.0001	$9.2 \cdot 10^{-6}$

Table 1: Extracted parameters for the experimentally estimated correction formula together with their average squared residuals. The ± signifies the 90 % confidence interval of the least square fit.

To show on the impact of flow distortion corrections, the difference between the wind speed measured by the S and ESE pointing cups are compared before and after correction formulas are applied, see Figure 21 and Figure2.

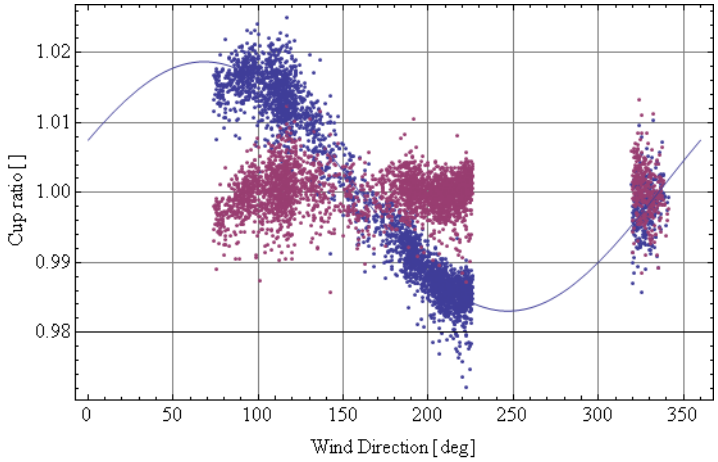

Figure 2: Observed cup ratio, blue, and after correction, red, for the first period.

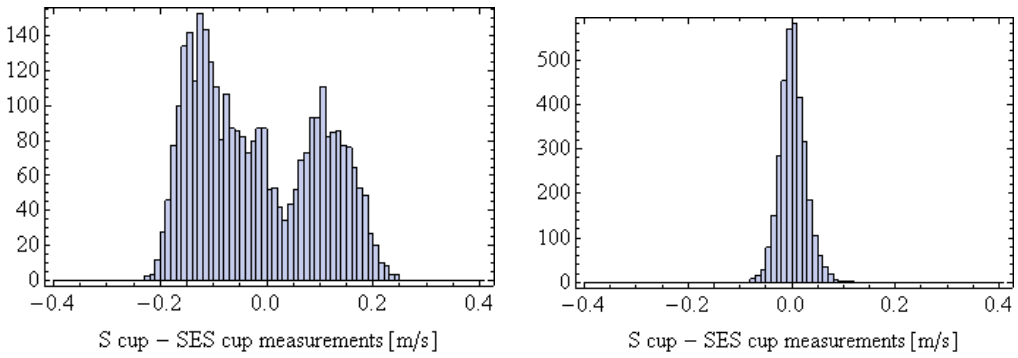

Figure 3: Histogram over the difference of the 10 minute horizontal wind speed measurements taken by the south and the east-southeast pointing cup anemometers during the first period. As observed, top, and after corrections, bottom.

5. Conclusion

The wind speed measurements taken by two cup anemometers, mounted according to current IEC guidelines, on a lattice tower with booms at the same height but with different pointing directions are observed to deviate, depending on wind direction, in a sinusoidal pattern with up to 3%. The deviation is considered to mainly be caused by flow distortion around the tower.

The flow distortion effect on the individual cup anemometers is extracted by fitting a modeled error to the measured cup ratio and wind direction. The measurement error is estimated to reach up to ± 2%. The errors are on average about 75% larger than those predicted from the IEC standard for power performance measurements.

The uncertainty in the wind speed measurement taken by a boom mounted anemometer can be significantly reduced by the method proposed in this article. The proposed correction method is estimated to reduce the standard uncertainty in the measurement due to the flow distortion to less than 0.5%.

References

[1] Maribo Pedersen B, Hansen K, Øye S, Brinch M and Fabian O, Some experimental investigations on the influence of the mounting arrangement on the accuracy of cup-anemometer measurements, Journal of Wind Engineering and Industrial Aerodynamics 1992; 7: 373-383.

[2] Hansen M and Pedersen B, Influence of the meteorology mast on a cup anemometer, Journal of Solar Energy Engineering 1999; 121: 128-131.

[3] IEC 61400-12-1. Wind turbines-Part 12-1: Power performance measurements of electricity producing wind turbines, 2005

[4] Filippelli M and Mackiewicz, P, Experimental and Computational Investigation of Flow Distortion Around a Tubular Meteorological Mast, Proc. CanWEA Conference, 2005

[5] Lindelöw. P, Uncertainties in wind assessment with LIDAR, Risø Report, Risø-R-1681(EN), ISSN 0106-2840, ISBN 978-87-550-3735-9, 2009

4.2 Quantification of Linear Torque Characteristics of Cup Anemometers with Step Responses

Troels Friis Pedersen

1. Introduction

The standard IEC61400-12-1 on power performance measurement [1] requires cup anemometers to be classified according to the normative Annex I. An informative Annex J proposes methods for determination of physical characteristics such as aerodynamic torque characteristics. The described method uses wind tunnel measurements where a thin rod is attached to the cup anemometer rotor and extended to the outside of the flow. Here a torque sensor and a motor are connected with the rod. The torque is then measured for typical wind speeds and rotational speeds of the cup anemometer. The torque measurements are normalized to obtain a generalized torque coefficient curve that is normally not linear. Meanwhile, if the torque coefficient above and below equilibrium speed ratio (tunnel calibration condition) both can be approximated to linear curves going through the equilibrium speed ratio point, then it might be possible to determine the linear curves with two step responses, one starting from below and one from above tunnel wind speed. This paper describes an investigation of the consequences of making classification of cup anemometers with such partial linearised torque coefficient curves. The investigation is described in further detail in the report [5].

2. Basic torque characteristics of cup anemometers

The generalised torque coefficient curve of a cup anemometer [1, annex J] is defined as the torque coefficient versus the speed ratio. The torque coefficient is related to the aerodynamic rotor torque as:

$$C_{QA} = \frac{Q_A}{\frac{1}{2}\rho A R u^2}$$

The speed ratio λ is defined as:

$$\lambda = \frac{\omega R}{U - U_c}$$

In case the torque coefficient curve can be assumed linear on either side of the equilibrium speed ratio the torque coefficient can be expressed as:

$$\begin{cases} \lambda \le \lambda_0 : C_{QA} = \kappa_{low}(\lambda - \lambda_0) \\ \lambda > \lambda_0 : C_{QA} = \kappa_{high}(\lambda - \lambda_0) \end{cases}$$

Where $\lambda_0 = \frac{R}{A_{cal}}$ is the equilibrium speed ratio.

When determining the torque relations we consider the friction in bearings being negligible. Thus the calibration coefficients relates to the speed ratio as:

$$U = A_{cal}\omega + B_{cal} = \frac{A_{cal}N}{2\pi}f + B_{cal} = \frac{R}{\lambda_0}\omega + U_c$$

3. Linearized torque characteristics of a typical cup anemometer

The analysis is based on measurements of torque coefficients made in the FOI wind tunnel by Jan-Åke Dahlberg in the ACCUWIND project [2]. The cup anemometers that were considered are shown in table 1 with some details.

Tablel 1 Main data of cup anemometers analysed in ACCUWIND project [2]

	NRG	RISØ	THIES-FC	VAISALA	VECTOR
Cup diameter (mm)	51	70	80	54	51
Projected cup area A (mm^2)	2000	3850	5030	2290	2040
Rotor diameter (mm)	191	186	240	184	155
Radius to cup centre R (mm)	70	58	80	65	52
Pulses/rev	2	2	37	14	25
Rotor inertia I (kg m^2)	$1.01 \cdot 10^{-4}$	$0.992 \cdot 10^{-4}$	$2.8888 \cdot 10^{-4}$	$0.6141 \cdot 10^{-4}$	$0.441 \cdot 10^{-4}$

The torque coefficient curves from [2] were linearized on either side of the equilibrium speed ratio, forced through the point of equilibrium speed ratio. The linearized torque coefficient data are shown in table 2 together with derived time constants from inertia in table 1 and with a standard air density of 1.23kg/m^3.

Table 2 Linearised torque coefficient data from linearization of Main data of cup anemometers analysed in ACCUWIND project [2]

	NRG	RISØ	THIES-FC	VAISALA	VECTOR
Equlibrium speed ratio λ_0	0.28461	0.29653	0.28022	0.28964	0.26177
Slope at low speed ratios κ_{low}	-6.5282	-4.9590	-4.6520	-4.8867	-6.6914
Slope at high speed ratios κ_{high}	-6.3595	-6.2140	-5.6901	-4.7652	-6.3128
Ratio $\frac{\kappa_{low}}{\kappa_{high}}$	1.0265	0.7980	0.8176	1.0255	1.0600

4. Classification of cup anemometers with linear torque

The torque coefficient curves from the ACCUWIND project [2] were applied for classification according to the standard IEC61400-12-1 [1]. The results with the full torque coefficient curves and tilt response data measured in the FOI wind tunnel were compared with the results using the linear torque coefficient data from table 2. The results are shown in Table 3.

Table 3 Classification of Risø P2546a using Cm curves or two linearized curves

	Class A	Class A linearized	Class B	Class B linearized
Risø P2546	1.39628	1.39404 (-0.16%)	5.09301	5.0887 (-0.09%)
Thies First Class	1.78074	1.76010 (-1.17%)	3.87461	3.89775 (+0.59%)
Vector	1.82939	1.84430 (+0.81%)	4.48396	4.26761 (-5.07%)
Vaisala	2.22558	2.14491 (-3.63%)	11.9380	11.8207 (-0.98%)
NRG Max40	2.41664	2.52689 (+4.36%)	8.28358	7.98579 (-3.73%)

The comparison of classification results from table 3 shows very good results. The largest deviation is 5.07% on the classification value. Considering that other uncertainties are significant in the whole classification process, this is an indication that linearized torque coefficient curves can be considered sufficient for classification.

5. Step response measurement procedures

There are two standards that consider step response measurements.

The recommended practice document IEA-11 [3] considers step response measurements in order to determine the time constant and the distant constant. The step response model used in the IEA-11 document is described as:

$$u(t) = u_0 + \Delta u\left(1 - \exp\left(-\frac{t - t_0}{\tau}\right)\right)$$

In IEA-11 a linear fitting of a conversion of the step response function is proposed:

$$\ln\left(1 - \frac{u(t) - u_0}{\Delta u}\right) = -\frac{t - t_0}{\tau}$$

The standard ISO 17713-1 [4] on wind tunnel test methods for rotating anemometer performance describes step response measurements in order to determine the distance constant. The model used is described as:

$$V_t = V_f\left(1 - \exp\left(-\frac{t}{\tau}\right)\right)$$

And the distance constant is determined from:

$$L_F = V\tau$$

The standard requires 10 step response measurements made at 5m/s and 10m/s. The time constant τ is determined from data measured between 30% and 74% of the tunnel wind speed, and the distance constant is determined by multiplying the tunnel wind speed with the time constant.

When we want to determine torque coefficient characteristics from step response measurements we have to find an appropriate method for determination of the slopes of the torque coefficient curves below and above the equilibrium speed ratio. Theoretical considerations documents and derive such a procedure [6]. The result is that the slopes can be derived as:

$$\kappa = -\frac{2I(u_0 + \Delta u - U_c)}{\rho A R^3 (u_0 + \Delta u)^2 \tau}$$

6. Step response measurements – an example

An example of a step-up response made by WindGuard is shown in figure 1. The cup anemometer is a Risø P2546 and the tunnel wind speed is 5m/s. Using the IEA-11 fitting procedure we get the logarithmic expression as function of time as shown in figure 2.

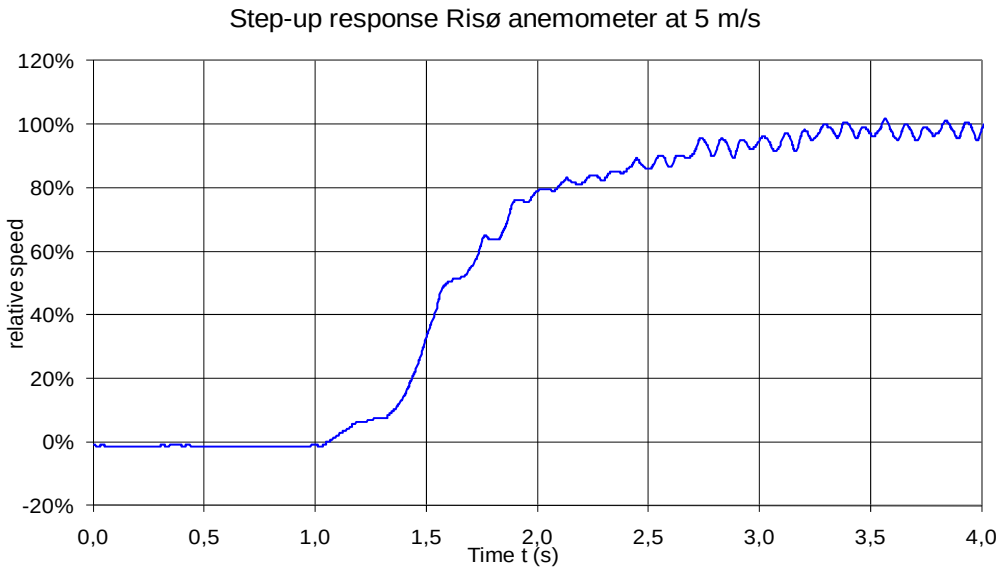

Figure 1 Step-up response of Risø P2546 cup anemometer at 5m/s tunnel wind speed

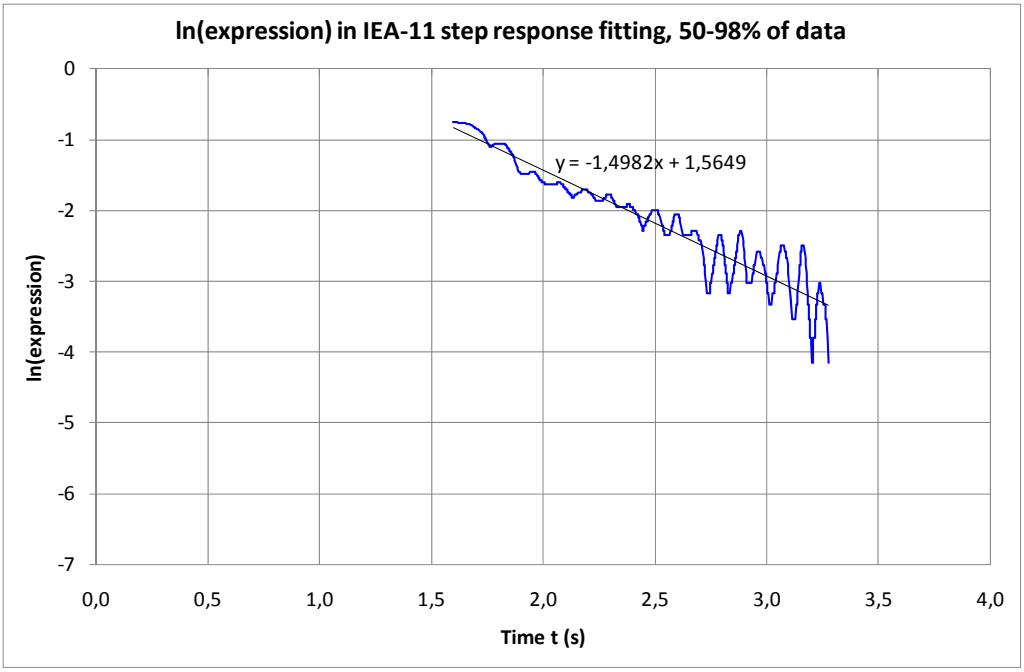

Figure 2 ln-expression from IEA-11 step response fitting procedure using 50-98% of step-up data

Figure 3 shows a speed-down response of the same Risø cup anemometer, first speeded up to 200%, and figure 4 shows the ln-expression for a relative speed range of 150-102%, which seems to cover quite well the essential part of the step response.

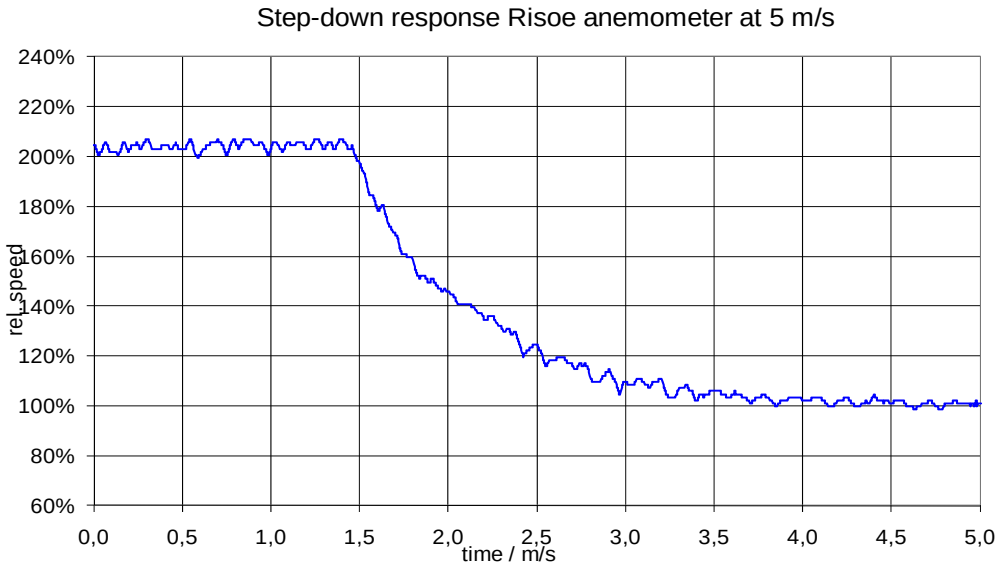

Figure 3 Step-down response of Risø P2546 cup anemometer at 5m/s tunnel wind speed

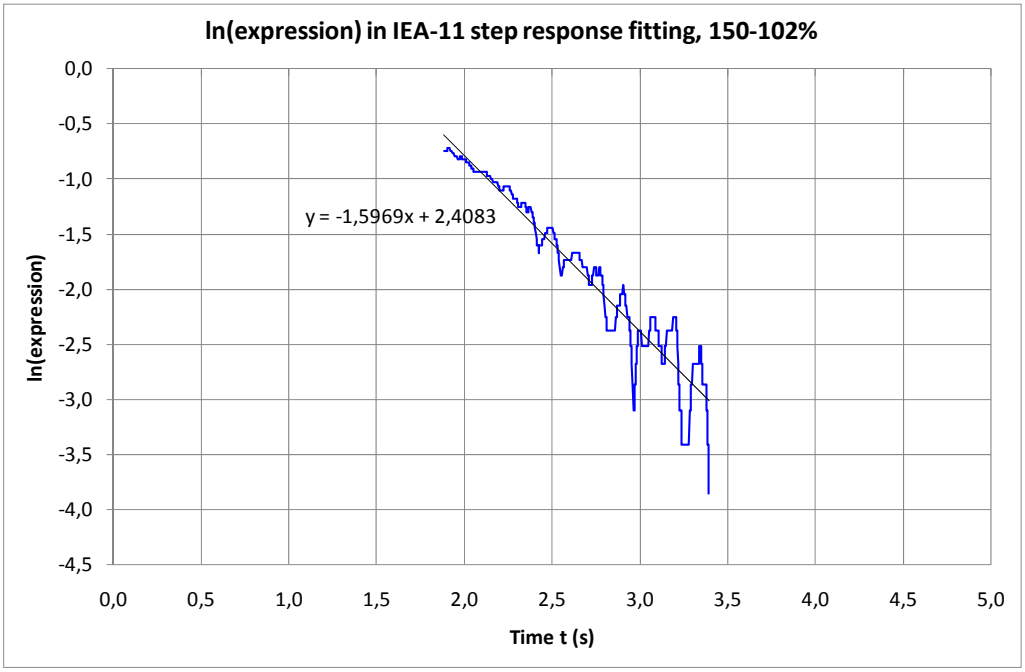

Figure 4 ln-expression from IEA-11 step response fitting procedure using 150-102% of step-down data

The step responses were performed more than once. Table 4 shows the results, where they are compared with the values from linearization of the torque curves from the ACCUWIND project.

Table 4 Slopes of linear torque coefficient curves for Risø P2546 cup anemometer determined with torque measurements according to [2] and with step responses

Risø torque coefficient slopes	Torque measurements ACCUWIND linearised	Torque measurements step responses	Ratio step/ACCUW
Equlibrium speed ratio λ_0	0.29653		
Slope at low speed ratios κ_{low}	-4.9590	-3.493	0.704
Slope at high speed ratios κ_{high}	-6.2140	-4.088	0.658
Ratio $\frac{\kappa_{low}}{\kappa_{high}}$	0.7980	0.8545	1.071

From table 4 it is seen that the step response method gives about 30% lower torque coefficient slopes than the linearized torque from the measurements in the ACCUWIND project. The torque coefficient slope values are proportional to the rotor inertia and the slopes of the ln-expressions, but reverse proportional to the time constants. The reason for the difference might be due to additional inertia in the rotating test equipment during the tests, but the cause has not been identified. The deviation is slope ratios is only 7%. It can be shown that the maximum overspeeding (at high frequencies) is only dependent on the ratio between the slopes of the torque coefficient curves. In this case it might be satisfactory for the classification only to know the ratio with a good accuracy.

7. Conclusions

The step response model of the IEA-11 document intrinsically leads to linear torque coefficient curves for step responses from low or high speed ratios. The slopes of the linear torque coefficient curves can thus be determined from the step response time constants. The intercept of the linear torque coefficient curves, which is the equilibrium speed ratio, is

determined from the normal wind tunnel calibration gain value. The standard ISO 17713-1 recommends step response data in the speed ratio range 30-75% to be used. This seems to be in a range that is outside of the usual range being used in classification according to IEC61400-12-1. In practice, a range closer to equilibrium speed ratios should be used; 50-98% for speed-up step responses and 150-102% for speed-down step responses. The step response measurements can satisfactorily determine linear torque coefficient characteristics of cup anemometers with the only assumption that the friction in bearings is negligible with respect to determination of aerodynamic torque characteristics. Meanwhile, slope values were found to be about 30% too low. The step response method may be improved by adding more inertia to the rotor to extend the data and to reduce torque ripples due to the cups, and by determining the rotor inertia with high accuracy.

References

[1] IEC 61400-12-1, 2005 Wind turbines – Part 12-1: Power performance measurements of electricity producing wind turbines

[2] Pedersen TF, Dahlberg J-Å, Busche P, "ACCUWIND – Classification of Five Cup Anemometers According to IEC61400-12-1", Risø-R-1556(EN), May 2006

[3] IEA-11 Wind Speed Measurement and Use of Cup Anemometry, Recommended Practices for Wind Turbine Testing and Evaluation, 1999

[4] ISO 17713-1, 2007 Meteorology – Wind Measurements – Part 1: Wind tunnel test methods for rotating anemometer performance

[5] Pedersen TF, "Quantification of Linear Torque Characteristics of Cup Anemometers with Step Responses", Risø-I-3131(EN), February 2011

5 Power performance measurement

5.1 Influence of shear

Rozenn Wagner

1. Introduction

Power performance measurement is central to the wind industry since it forms the basis for the power production warranty of the wind turbine. The power curve measurement has to be realised according to the IEC 61400-12-1 standard [1]. The power curve is obtained with 10 minutes mean power output from the turbine plotted against simultaneous 10 minutes average wind speeds. The standard requires the wind speed to be measured by a cup anemometer mounted on top of a mast having the same height as the turbine hub and located at a distance equivalent to 2.5 rotor diameters from the turbine.

Such a plot usually shows a significant spread of values and not a uniquely defined function. The origin of the scatter can mainly be grouped to four categories: the wind turbine operation and maintenance, lack of correlation due to mast distance, sensor uncertainties and the wind characteristics. Within the last group, the current standard only requires the wind speed at hub height and the air density measurement. However, other wind characteristics can influence the power production like the variation of the wind speed with altitude (i.e. wind speed shear). The influence of wind speed shear on the power performance was shown in several studies: some based on aerodynamic simulations [2] others based on measurements [3],[4].

A major issue is to experimentally evaluate the wind speed shear. The wind speed profile is usually assumed to follow one of the standard models such as the logarithmic or power law profiles. However, these models are true for some particular meteorological conditions, and therefore they cannot represent all the profiles that can be experienced by a wind turbine. Measurements are then a better option but are also challenging. Indeed characterising the speed profile in front of the rotor of a multi-megawatt wind turbine requires measurements of wind speed at several heights, including some above hub height, i.e. typically above 100m. Remote sensing instrument such as lidar or sodar then appear as a very attractive solution.

This chapter starts with a description of the influence of the speed shear on the power performance of a multi-megawatt turbine. The challenge of describing the speed profile is then discussed followed by a description of an experiment using a lidar to characterise the speed profile. This is followed by the introduction of the definition of an equivalent wind speed taking the wind shear into account resulting in an improvement of the power performance measurement. Finally, some recommendations about remote sensing instruments are given to successfully apply this method.

2. Shear and turbine aerodynamics

When the flow is axial and homogeneous, i.e. the wind speed is the same at any point, the wind speed seen from a given point on one of the wind turbine blades is the same for any azimuth position. The angle of attack and the relative wind speed are therefore independent on the blade azimuth position (the nacelle tilt is ignored for simplification here), and so is the resulting tangential force. On the contrary, if the flow in front of the turbine presents a shear (vertical variation of the horizontal wind speed), the wind speed seen by a given point on a rotating blade varies with the azimuth position of the blade, so does the tangential force on all blades which affects the resulting torque, see Figure 1.

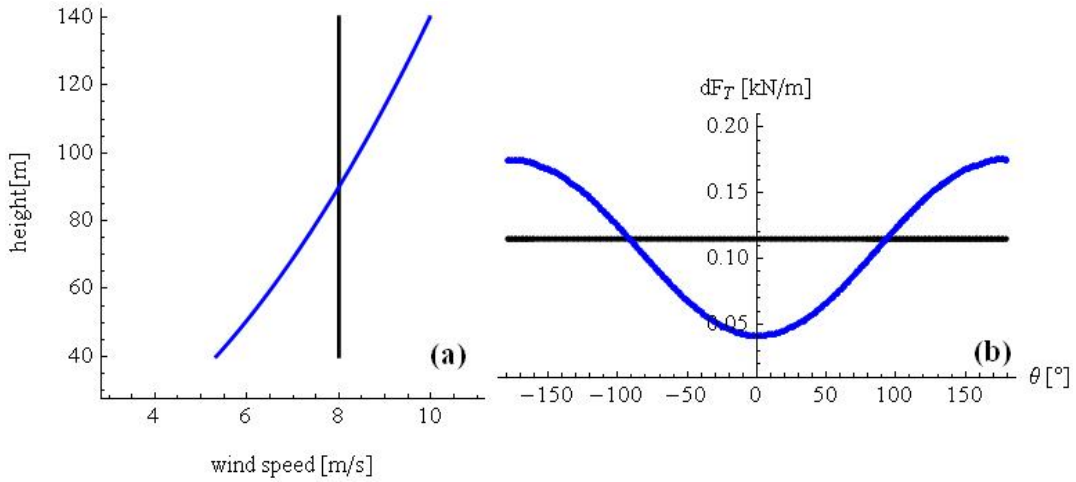

Figure 1 (a): Constant wind speed profile at 8m/s (black), power law profile with a wind speed at hub height (90m) of 8 m/s and a shear exponent of 0.5; Local tangential force for one blade at a radius of 60m obtained with HAWCAero simulations for the 2 wind speed profiles shown in (a).

The power law profile in Figure 1 (a) is not linear and the tangential force in Figure 1 (b) is not sinusoidal. Therefore different power output can be obtained for the same wind speed at hub height depending on the complete wind speed profile affecting the rotor, i.e. the speed profile between the lower and higher tip heights, see Figure 2.

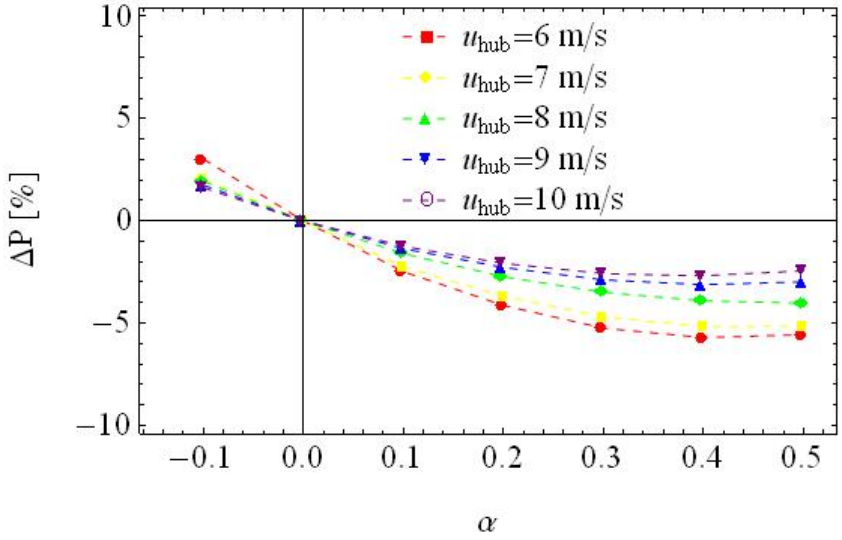

Figure 2 Relative difference in power output (simulated with HAWC2Aero) between a constant free wind speed profile and a power law profile with the same wind speed at hub height, shown as a function of the shear exponent. The simulated power output of the wind turbine is smaller for a power law profile than for a constant profile and the magnitude of the difference depends on the wind speed at hub height.

3. Equivalent wind speed

One of the main differences between a sheared inflow and a uniform inflow, regarding power production, is the kinetic energy flux conveyed by each profile. According to this idea, an "equivalent wind speed" was defined based on the kinetic energy flux of the flow going through the rotor swept area, assuming horizontal homogeneity of the flow. This wind speed is equivalent to the wind speed of a profile constant with height giving the same kinetic energy flux the actual profile (not constant). Contrary to the traditional power curve, which depends on only one wind speed (at hub height), the use of this equivalent wind speed results in a power curve accounting for the influence of shear.

This method was first tested with aerodynamic (BEM) simulations of a MW wind turbine subjected to various shears [2]. The use of the equivalent wind speed was found to reduce the scatter due to vertical shear in the power curve.

4. Experimental validation of the method

The major challenge in the experimental application of the equivalent wind speed method is to characterize the speed profile in front of the wind turbine. As lidars measure the wind speed at several heights, it enables us to measure the horizontal wind speed profile in front of the wind turbine rotor. Better than a hub height mast, with a lidar, measurements can be taken up to the highest tip height, i.e. nor assumptions neither extrapolation are needed above hub height. A good approximation of the kinetic energy flux can thus be obtained.

A lidar was installed in front of a MW wind turbine in order to measure the upcoming wind speed profile. The power curves scatter plot obtained with the equivalent wind speed derived directly from the lidar measurements presented less scatter than the traditional power curve obtained with measurements at hub height only, see Figure 3. This method therefore results in a power curve which is less dependent on the shear than the current standard power curve. It is to be noted though that it is not completely independent of the shear as the power performance of the turbine does not depend only on the kinetic energy flux but also on the response of the turbine to various shear conditions.

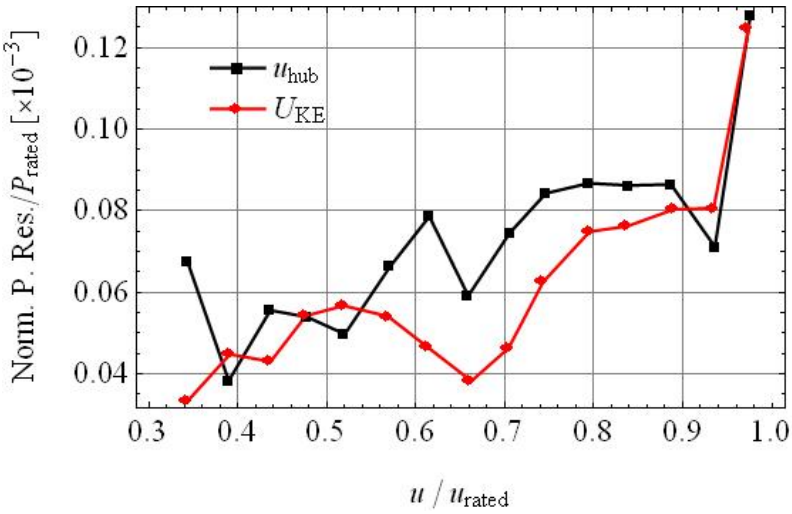

Figure 3 Scatter (quantified as the normalized residuals) in the power curves obtained with the wind speed at hub height only and the equivalent wind speed (derived from lidar wind speed profile measurement). The use of the equivalent wind speed reduce decreases the scatter due to shear in the power curve.

5. Conclusions

As it is less dependant of the shear, this power curve is more repeatable, i.e. nearly identical power curve can be obtained for various shear conditions, e.g. various seasons and/or various locations. Such a power curve not only facilitates the comparison of the performance of various turbines, but also improves the AEP prediction. Indeed the AEP prediction at a site potentially selected to build a wind farm is usually based on a power curve measured prior to the installation of the turbines at another site.

Furthermore, the reduction of scatter in the power curve results in the decrease of the category uncertainty in power curve measurement (according to IEC 61400-12-1 definitions). However the combined uncertainty in power curve measurement was not reduced because the reduction in category A uncertainty was counterbalanced by an increase in the category B wind speed measurement uncertainty. This is due to the fact that the wind speed was measured by a lidar, of which, as an instrument recently introduced to wind energy, the

measurement uncertainty was defined relative to the uncertainty of cup anemometers, and also that the category B uncertainty due to wind shear in IEC 61400-12-1 is not taken into account.

References:

[1] IEC 61400-12-1 Power performance measurements of electricity producing wind turbines, Ed.2 , 2005

[2] Wagner R., Antoniou I., Pedersen S.M., Courtney M.S. and H.E. Jørgensen, 2009: *The influence of the wind speed profile on wind turbine performance measurements*, Wind Energy, **12**:348-362.

[3] Elliott DL and Cadogan JB, *Effect of wind shear and turbulence on wind turbines power curve*, EWEC 1990

[4] Sumner J and Masson M, *Influence of atmospheric stability on wind turbine power performance curves*, Journal of solar energy engineering, 128:531—538,2006

5.2 Turbulence normalization combined with the equivalent wind speed method

Rozenn Wagner and Julia Gottschall

1. Introduction

The power performance of a wind turbine has to be measured according to the IEC 61400-12-1 standard [1]. The power curve is obtained with 10 minute mean power output from the turbine plotted against simultaneous 10 minute average wind speeds. The standard only requires the wind speed the wind speed at hub height and the air density (derived from temperature and pressure measurement). However it has been shown that other characteristics of the wind field influence the power performance measurement too. These parameters are the wind shear (see chapter 3.1) and the turbulence intensity [1, 2]. Turbulence intensity (TI) is defined as the ratio between 10-minute standard deviation and mean wind speed.

2. Effect of the turbulence intensity

When the wind speed fluctuates around the rated wind speed, the power extracted is limited to the rated power. Therefore only "negative fluctuations"' (i.e. the instantaneous wind speeds below rated speed) of the wind are transformed into power fluctuations. Consequently, 10 minute mean power obtained with a given turbulence intensity is generally smaller than the power that would be obtained with the same mean wind speed and a laminar flow (TI=0%), and the mean power decreases as the turbulence intensity increases, see Figure 1. In the same way, as the wind speed fluctuates around the cut-in wind speed, only the positive fluctuations are transformed in power fluctuations. Therefore, near the cut-in wind speed, the mean power is expected to increase with the turbulence intensity. Between the cut-in and rated speeds, the turbine is expected to respond to any wind speed fluctuations (positive or negative). Within the wind speed range where the C_P is nearly constant, the turbine power increases with the turbulence intensity as the power is then proportional to the cube of the wind speed. Moreover, according to BEM simulations (with HAWC2Aero), the scatter increases around the mean power curve with the turbulence intensity.

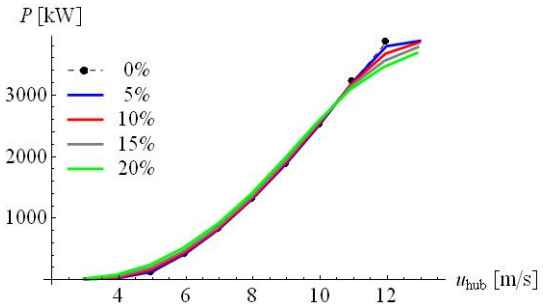

Figure 1 Mean power curves for various turbulence intensities

The effect of the turbulence intensity on the power curve can be seen as the combination of one effect on the mean power curve that varies with the turbulence intensity (especially around rated speed) and one effect on the scatter that increases with the turbulence intensity. The scatter in the power curve results from both effects as it usually results from a distribution of various turbulence intensities.

3. Equivalent wind speed and turbulence

The effects of turbulence intensity on the power curve cannot be taken into account with a simple definition of equivalent wind speed similar to the one used to account for the shear in chapter 2.2 [2]. Albers suggested a method aiming at representing the non linear relation between the 10 minute mean power and the 10 minute mean wind speed [1]. This method is

based on the fact that the 10 minute average of the power is not linearly related to the mean wind speed but to the wind speed distribution during the considered 10 minute and the shape of the power curve.

4. Description of Albers' method

The model is based on the assumption that the wind turbine follows the same power curve at each instant. This power curve is the curve that should be theoretically obtained with 0% turbulence intensity. According to this assumption, the power output of the turbine for any turbulence intensity can be simulated by:

$$P_{sim}(v,TI)=\int_{v=0}^{\infty} P_{0\%}(v)\, f(v)\, dv \qquad (1)$$

where $P_{0\%}(v)$ is the power given by the 0%-TI power curve for the wind speed v, and f(v) is the wind speed distribution within the 10 minutes. This distribution is assumed to be Gaussian, denoted by $f(v)=N(v,\sigma^2)$, it only depends on the 10 minute wind speed average, v, and variance, σ^2. The variance here is given by $\sigma^2 = v^2 \times TI^2$. Albers' method therefore consists of 2 steps:

The estimation of the 0%-TI power curve;

The simulation of the power curve for a chosen turbulence intensity: TI_{target}.

Step1: definition of the 0%TI power curve

The 0%-TI power curve is derived from a few parameters characteristic of the turbine: the rated power, the cut-in wind speed and the maximum C_P [1]. The values taken for these parameters are tuned with an iterative process in order to minimize the error between the simulated mean power curve and the measured mean power curve. The simulated mean power curve is the power curve obtained by applying (1) to each wind speed bin (i.e. the wind speed bins used to average the power curve as described in the IEC 61400-12-1 standard) statistics: $P_{sim}(v_i, TI_i)$ where v_i is the bin-averaged speed and TI_i is the bin-averaged turbulence intensity in the i^{th} bin.

Step2: Simulation of the power output with TI_{target}

Once the 0%-TI power curve has been determined, each 10 minute measured power output is corrected for the TI_{target} by applying the formula:

$$P^{(10)}_{TI_{target}}(v^{(10)}_{meas}) = P^{(10)}_{sim}(v^{(10)}_{meas}, TI_{target}) + P^{(10)}_{meas} - P_{sim}(v^{(10)}_{meas}, TI^{(10)}_{meas}) \qquad (2)$$

where $P^{(10)}_{meas}$ and $v^{(10)}_{meas}$ are the simultaneous measured 10 minute mean power and wind speed and $TI^{(10)}_{meas}$ is the 10 minute measured TI. $P^{(10)}_{sim}(v^{(10)}_{meas}, TI^{(10)}_{means})$ is the power output expected if the assumption that the turbine follows the 0% TI power curve at each instant was true. But there is actually a difference between the actual power output and the simulated power output as the power curve is influenced by other parameters than the turbulence intensity such as the speed shear for example. Albers' method can only reduce the scatter due to the distribution of the turbulence intensity during the power curve measurement. Figure 2 shows the measured power curve scatter plot, the simulated power curve for $TI_{target}=10\%$ and the predicted power curve scatter plot for $TI_{target}=10\%$

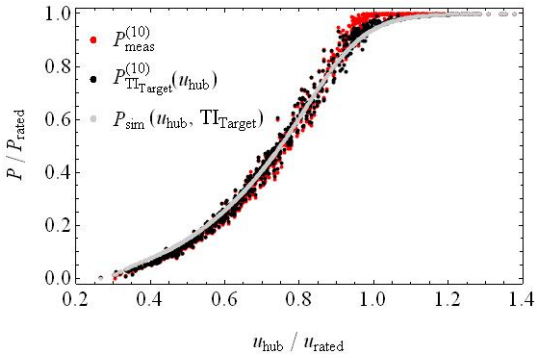

Figure 2 Measured power curve scatter plot ($P^{(10)}_{meas}$), simulated power output for $TI_{target} = 10\%$ ($P^{(10)}_{sim}(v^{(10)}_{meas}, TI_{target})$), resulting simulated power curve scatter plot ($P^{(10)}_{TI_{target}}$).

5. Combination with the equivalent wind speed

Albers' method was designed to normalise the standard power curve to a chosen TI: TI_{target}. On the other hand, the equivalent wind speed method (described in section 2.2) "normalizes" the power curve for the effect of shear, the combination of these two methods would result in a power curve less sensitive to the wind characteristics, and therefore less dependent on the site and season.

The turbulence normalisation changes the power value whereas the equivalent wind speed method changes the wind speed. It is therefore quite simple to combine both method in order to obtain a power curve less sensitive to shear and turbulence intensity.

Albers' method was initially designed to normalise the standard power curve, i.e. based on wind speed measurements at hub height, for the turbulence intensity. In order to compare the results to those obtained by combining Albers' method with the equivalent wind speed, the turbulence normalisation was applied to both power curves: with hub height wind speed and with equivalent wind speed. Therefore for a given TI_{target} value, four results can be compared:

	Measured power	Normalised power
u_{hub}	Standard power curve	Alber's method
U_{eq}	Equivalent wind speed power curve	Combined method

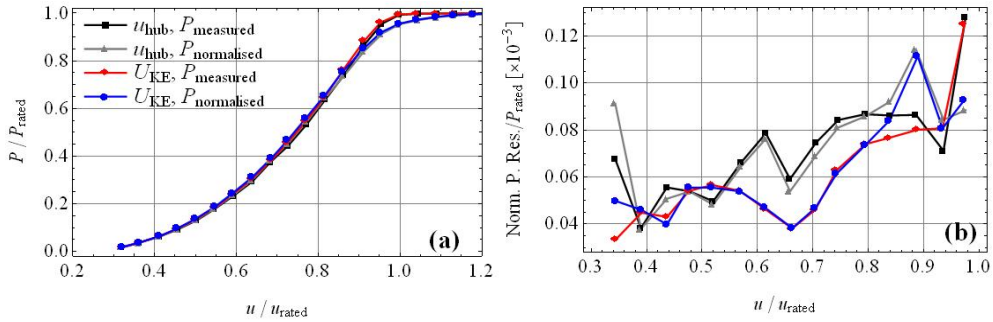

Figure3 Mean power curve and scatter in the power curve obtained with wind speed measurements at hub height and equivalent wind speed, both with and without turbulence normalisation using Albers' method

The power curve obtained by combining both the equivalent wind speed and Alber's turbulence normalization presents both a modification of the shape of the mean power curve (due to the different TI) and a reduction of the scatter around the mean power curve (scatter due to the shear).

6. Conclusions

The equivalent wind speed method reduces scatter due to shear also when the power has been normalised for the turbulence intensity according to Albers' method for turbulence normalization, except near rated speed where the mean power curve slope is significantly changed.

The mean power curve obtained with the combination of both methods is less sensitive to shear and is representative for a given TI. Such a power curve can give a better representation of the power curve that would be obtained at another site, with different wind shears and turbulence intensities from the power curve measurement site. In this sense, it is transferable from one site to another. Therefore it would give a better Annual Energy Production (AEP) estimation.

References

[1] Kaiser K, Hohlen H, Langreder W, *Turbulence correction for power curves*, EWEC 2008

[2] Albers A, *Turbulence normalisation of wind turbine power curve data*, EWEC 2010

[3] Wagner R, *Accounting for the speed shear in wind turbine power performance measurement*, PhD thesis (chapters 4 and 9), 2010.

5.3 Generics of nacelle anemometry

Troels F. Pedersen

1. Introduction

The generic influence of the flow induction on nacelle anemometry was studied lately by Sten Frandsen. He published a paper at the EWEC conference 2009 in Marseille [1] with five co-authors, including the author of this article. The paper was the last work of Sten Frandsen on nacelle anemometry, which was a dedicated topic in his large variety of research. He sadly passed away autumn 2010. This article is an extract from his paper.

Nacelle anemometry is the state of the art wind measurement method for turbine regulation and performance verification. The option of using the nacelle anemometer when determining the power curve of a wind turbine is attractive since it is much cheaper than erecting a separate meteorological mast and simpler since all data signals are already recorded in the wind turbine's control and data recording system. In particular, the consequences of the effect of rotor flow induction must be dealt with, but also the local flow distortion over the nacelle where nacelle anemometry is positioned is necessary to consider in turbine regulation and performance verification. Thus, if the power changes it must a priori be expected that the rotor flow speed changes, even if the free wind speed is unchanged. In that case the calibration of the nacelle anemometer is changed, effectively introducing an error to the test. In the paper of Sten Frandsen [1], previous investigations of nacelle anemometry is reviewed, the relevance of Betz theory is investigated by means of CFD computations, and the generic errors caused by the rotor flow induction is evaluated, estimated and exemplified.

1.1 Review of nacelle anemometry

Nacelle anemometry as an option for power performance verification was identified in the beginning of the 1990'ies, where some developers and manufacturers started to apply nacelle anemometry in the contect of commercial contracts. The method included the calibration of the nacelle anemometer, already installed on the top of the nacelle of the wind turbine, against an unobstructed met mast at a reasonably flat location in the wind farm. The method was first mentioned in 1994 [2], which deals with trends in power performance measurement techniques and recommendations with respect to positioning of the wind sensor on the nacelle is presented. In the mid 1990'ies the concept was assessed in several European research projects. Antoniou [3,4] investigated nacelle anemometry on a 1MW wind turbine by positioning the nacelle anemometer at different height above the nacelle and he made conclusions on the technique when the anemometer was in the wake of the blade root and behind the profiled blade. Another investigation [5,6,7] considered basic problems with nacelle anemometry and stipulated the uncertainty of the method. Yet another project [8] considered measurements on several different turbines throughout All assessments of the method have so far concluded that the method was acceptable when carefully addressing all aspects of the procedure. In 2007 an alternative wind measurement concept to nacelle-mounted anemometry, the spinner anemometer, was proposed, [9], the concept taking advantage of the less complicated flow field in front of the rotor. The international standardization organisation International Electrotechnical Commission decided in 2006 that the nacelle anemometry method was ripe and the decision resulted in a draft in 2008 [10], where past experience are condensed and the procedure to apply is given in detail. Following international review and revisions the standard is expected to be issued ultimo 2009.

1.2 Specific background

By convention, the power curve is the electric power plotted against the wind speed at hub height, measured at a location undisturbed by the wind turbine itself. Partly also by convention data are pre-averaged over 600 sec. The mentioned upcoming IEC standard [10] gives detailed directions for the procedure to employ, including specifications on how to calibrate the nacelle anemometer so that the free flow speed can be deduced from the reading of the nacelle anemometer. Obviously, the nacelle anemometer is mounted on top of the nacelle at some vertical distance from the nacelle and some distance from the wind turbine

rotor. In short, the calibration of the nacelle based-anemometer is made by correlating the reading from the nacelle anemometer in fairly flat, non-complex terrain with the free-flow wind speed measured in a met mast 2-3 rotor diameters upwind of the wind turbine.

However, the effect rotor induced flow is a priori correlated to the effect we want to estimate, namely rotor power. According to simple Betz theory [11] the speed of the flow passing through the rotor is the average of the free wind speed and the wind speed in the wake some distance downwind of the rotor. And further, the rotor flow speed is linked closely to the power output. Therefore, if the power changes it must a priori be expected that the rotor flow speed changes, even if the free wind speed is unchanged. In that case the calibration of the nacelle anemometer is not the same as it were beforehand. In the following we try to shed light on the generic effect rotor induction.

2. Flow induction at rotor

Most often, the end product of the performance test is the annual energy output of the wind turbine, conditioned on specific characteristics of the wind speed climate,

$$E_{AEP} = 8760 \cdot P_m \quad \text{where} \quad P_m = \int_0^\infty p(u) f(u) du \tag{1}$$

where $f(u)$ is the frequency distribution of wind speed at hub height at the specific wind turbine site. The number 8760 is the number of hours per year.

The purpose of the field test of the power curve by means of nacelle anemometry is to identify and quantify possible deviations relative to the warranted power curve, $\delta_p(u) = p(u) - p_{warranted}(u)$. However, when determining δ_p, the principle itself of nacelle anemometry affects the result so that the deviation has an error attached to it, $\delta_p^* = \delta_p + \delta_{p,error}$. In the following, we quantify the error in the deviation, $\delta_{p,error}$, introduced by nacelle anemometry.

2.1 Betz and nacelle anemometry

In the formulation of the theory for an ideal, infinitely fast rotating propeller, Betz (1920) finds that the wind speed in the wake of the rotor is $(1-2a)u$ and in the rotor plane

$$v = (1-a)u \tag{2}$$

where u is the undisturbed free wind speed and a is a quantity denominated induction factor. Thus, v is the mean of upwind and downwind wake wind speed.

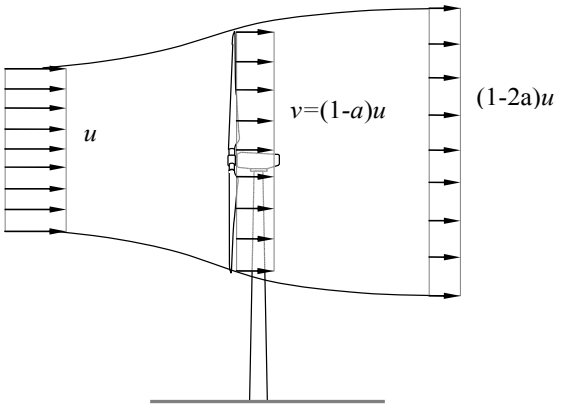

Figure1 Stream tube of wind turbine rotor.

Further, Betz deduces that the power curve and power coefficient of the rotor is related to the undisturbed wind speed and induction factor by

$$C_P = 4a(1-a)^2 \tag{3}$$

$$p = ½\rho u^3 A_R 4a(1-a)^2 \tag{4}$$

Consider now the scenarios outlined in the following. A specimen of a wind turbine series is tested in terrain complying with the appropriate standard, and the *reference* power $p_0(u)$, corresponding to the free wind speed u, and the corresponding nacelle anemometer wind speed v are measured and an induction factor a is determined,

$$v = (1-a)u \Rightarrow \quad a = 1 - \frac{v}{u} \tag{5}$$

Next, another specimen of the wind turbine series is sold and installed at a *field site*. In order to check its productive capacity relative to the reference turbine, a *met tower* is erected to measure the free wind speed and together with measured power and nacelle wind speed, these determine a power curve point and an induction factor:

$$p(u) = p_0(u) + \delta_p = p_0\left(1 + \frac{\delta_p}{p}\right) \tag{6}$$

$$v_1 = \big(1 - (a + \delta_a)\big)u \;\Rightarrow\quad a_1 = a + \delta_a = 1 - \frac{v_1}{u} \tag{7}$$

where u is the free wind speed (same as in the reference case), δ_p is the increase in power relative to the reference case, v_1 is the wind speed in the rotor plane and δ_a is the change in the induction factor relative to the reference case. With fixed free wind speed *u,* the change in power may be related to the change in induction factor:

$$\delta_p \approx \frac{\partial p}{\partial a}\cdot\delta_a + \frac{\partial p}{\partial u}\cdot 0 = \frac{\partial p}{\partial a}\cdot\delta_a, \tag{8}$$

where

$$\frac{\partial p}{\partial a} = 6\rho u^3 A_R(\tfrac{1}{3} - a)(1-a)$$

.

Thus, the change of the power curve relative to the reference power curve is

$$\delta_p \approx 6\rho u^3 A_R(\tfrac{1}{3} - a)(1-a)\delta_a \tag{9}$$

.

Now, assume that during the field test the wind speed is determined *only by means of the nacelle anemometer*. The reading of the nacelle anemometer is still v_1 and with no new information available on the calibration of the nacelle anemometer, the induction factor is assumed to be the one deduced previously from the reference test. Thus, the free wind speed will be estimated as

$$u_1 = \frac{v_1}{1-a} \tag{10}$$

The estimate of power output is unchanged, $(p_0 + \delta_p)$, and therefore the PC estimate at wind speed u_1 is

$$p_1(u_1) = p_0 + \delta_p \quad . \tag{11}$$

In order to compare directly with the field test result, where a met mast was available, the immediate result must be extrapolated from the presumed free wind speed u_1 to the actual free wind speed u ,

$$p_1(u) = p_1(u_1) + \delta_{p,error} = p_0 + \delta_p + \delta_{p,error} \tag{12}$$

By differentiating for fixed nacelle wind speed v and by assuming the change in induction "small", the extrapolation distance $\delta_u = u_1 - u$ is found:

$$\delta_u \approx \frac{\partial u}{\partial a}\delta_a = -\frac{u}{1-a}\delta_a \quad \text{since} \tag{13}$$

$$\frac{\partial u}{\partial a} = \frac{\partial}{\partial a}\left(\frac{v}{1-a}\right) = -\frac{v}{(1-a)^2} = -\frac{u}{1-a}$$

For a specific wind turbine the test assumption is that power is solely a function of hub height free wind speed, and therefore also the induction factor is a function of wind speed only, $a = a(u)$. Therefore, the error introduced by the nacelle anemometry technique may be estimated as

$$\delta_{p,error} \approx \delta_u \frac{dp}{du} \quad , \tag{14}$$

where

$$\begin{aligned} \frac{dp}{du} &= \frac{d}{du}\left(\tfrac{1}{2}\rho u^3 A_R 4a(1-a)^2\right) \\ &= 6\rho u^2 A_R\left[a(1-a)^2 + (\tfrac{1}{3}-a)(1-a)u\frac{da}{du}\right] \end{aligned} \tag{15}$$

The derivative $\frac{da}{du}$ can in principle only be estimated from the measured complete power curve. However, it appears from a typical power curve, that the second term in the hard bracket of Eq. (15) is insignificant compared to the first term. Therefore,

$$\frac{dp}{du} \approx 6\rho u^2 A_R a(1-a)^2 \quad . \tag{16}$$

Thus, combining eqs. (13,14 and 16) we get

$$\begin{aligned} \delta_{p,error} &\approx 6\rho u^2 A_R a(1-a)^2 \frac{u}{1-a}\delta_a \\ &= 6\rho u^3 A_R a(1-a)\delta_a \end{aligned} \tag{17}$$

It seems appropriate to relate the error to the real deviation δ_p of the field power curve from the reference power curve:

$$r_{p,error} = \frac{\delta_{p,error}}{\delta_p} \approx \frac{6\rho u^3 A_R a(1-a)\delta_a}{6\rho u^3 A_R(\tfrac{1}{3}-a)(1-a)\delta_a} \Rightarrow$$

$$r_{p,error} \approx \frac{a}{\frac{1}{3}-a}. \tag{18}$$

Thus, if by means of the nacelle anemometry technique a deviation from the reference power curve is measured, then the technique itself exaggerates the deviation by $100 \cdot \frac{a}{\frac{1}{3}-a}\,\%$. The exaggeration increases dramatically when the induction factor approaches its optimal value

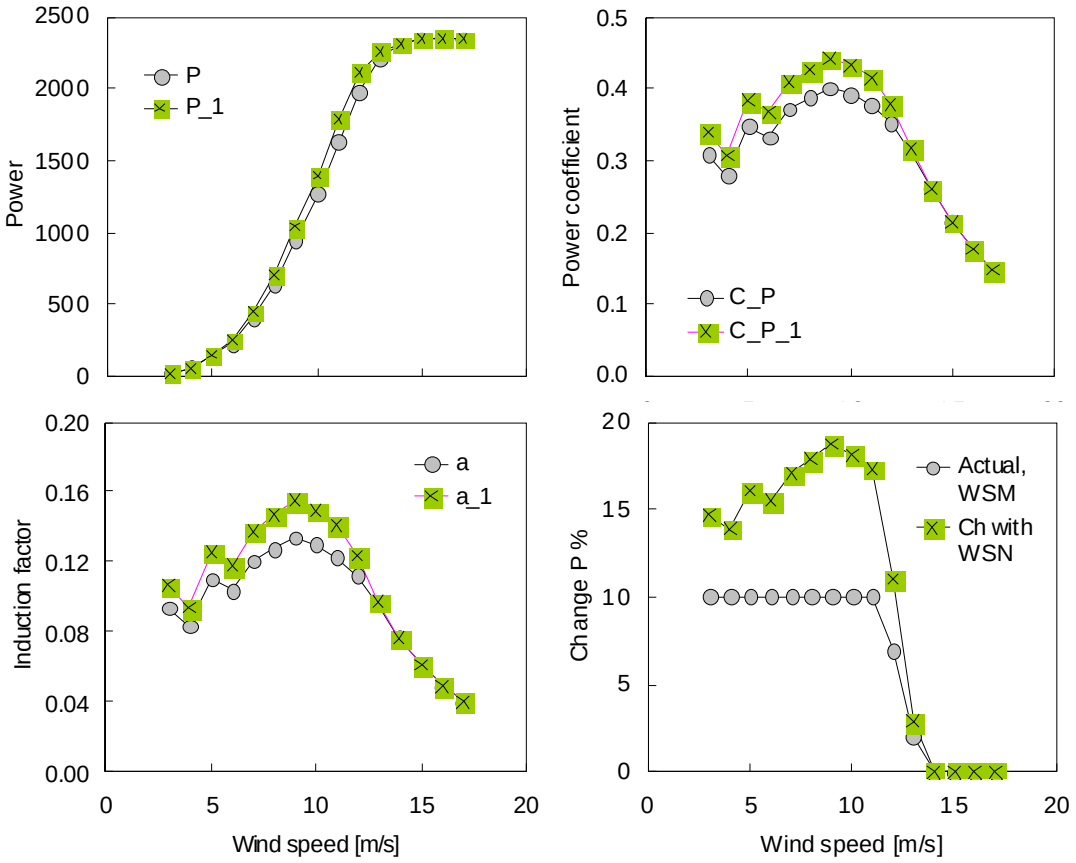

Figure 2 Illustration of reference measurement and measurement at a field site, indexed "1". top left) power curves measured with met tower; top right) corresponding power coefficient curves; bottom left) corresponding induction factor, and bottom right) difference in power from the reference measurement to the field site with standard technique (including met mast WSM and with only the application of nacelle anemometry, respectively – the difference between the two curves corresponds to Eq. (22).

$\frac{1}{3}$. The consequences of this result are illustrated in Figure 1.

The paper [1] relates the theoretical derivations of the influence of the induction to CFD computations on a 500kW Nortank and a 2MW turbine. It is here remarked that the 1-D Betz distributions largely correspond to the computed values using averaged interference factors. This strongly supports the idea that Eq. (18) is a relatively exact measure of the overall bias error.

3. Conclusions

The generic problems related to the use of the nacelle anemometer for determination of the power curve of a wind turbine was investigated. The following was noted:

- The flow induction caused by the rotor depends on wind speed *and* power and thus a problem concerning the nacelle anemometer's calibration persists, being increasingly worse with increasing rotor efficiency.
- The error related to the flow induction is by nature a bias error and may be estimated by means of a combination of the data recorded for the power curve and of 1-D Betz theory adjusted and thereby enhanced by more comprehensive aerodynamic calculations
- The rotor induction close to the hub is most often significantly less, which counter the induction error
- The radial transient in induction factor close to the hub – and therefore potentially close to the position of the nacelle anemometer – is high and may make it difficult to determine the error to be compensated for.
- In all, it is believed that nacelle anemometry is a viable option, given that careful investigation of and correction for the error caused by induction is made *in addition* to the directions made in the present draft of the standard for nacelle anemometry power curve measurements.

References

[1] Frandsen S, "The Generics of Wind Turbine Nacelle Anemometry", EWEC2009 Marseille

[2] Pedersen TF, "Trends in power performance measurement standards", AWEA'94

[3] Antoniou I, Pedersen TF, "Nacelle Anemometry on a 1MW Wind Turbine: Comparing the power performance results by use of the nacelle or mast anemometer", Risø-R-941(EN), August 1997

[4] Frandsen, S. (ed.); Antoniou, I.; Chaviaropoulos, T.; Dahlberg, J.A.; Derrick, A.; Douvikas, D.; Dunbabin, P.; Hansen, J.C.; Hunter, R.; Kanellopoulos, D.; Kapsalis, G.; Kristensen, L.; Aagaard Madsen, H.; Mortensen, N.G.; Ruffle, R., "Power performance assessment. Final report". (Risø National Laboratory, Roskilde, 1999) 205 p

[5] Dahlberg, J.-A.; Frandsen, S.; Aagaard Madsen, H.; Antoniou, I.; Pedersen, T.F.; Hunter, R.; Klug, H., "Is the nacelle mounted anemometer an acceptable option in performance testing?". In: Wind energy for the next millennium. Proceedings. 1999 European wind energy conference (EWEC '99), Nice (FR), 1-5 Mar 1999. Petersen, E.L.; Hjuler Jensen, P.; Rave, K.; Helm, P.; Ehmann, H. (eds.), (James and James Science Publishers, London, 1999) p. 624-627

[6] Dahlberg, J.-A.; Frandsen, S.; Aagaard Madsen, H.; Antoniou, I.; Pedersen, T.F.; Hunter, R.; Klug, H., "Is the nacelle mounted anemometer an acceptable option in performance testing?". In: Wind energy for the next millennium. Proceedings. 1999 European wind energy conference (EWEC '99), Nice (FR), 1-5 Mar 1999. Petersen, E.L.; Hjuler Jensen, P.; Rave, K.; Helm, P.; Ehmann, H. (eds.), (James and James Science Publishers, London, 1999) p. 624-627

[7] Frandsen, S.; Antoniou, I.; Hansen, C.J.; Kristensen, L.; Aagaard Madsen, H.; Chaviaropoulos, B.; Douvikas, D.; Dahlberg, J.A.; Derrick, A.; Dunbabin, P.; Hunter, R.; Ruffle, R.; Kanellopoulos, D.; Kapsalis, G., "Redefinition power curve for more accurate performance assessment of wind farms", Wind Energy (2000) 3 , 81-111

[8] Frandsen, S.; Antoniou, I.; Hansen, C.J.; Kristensen, L.; Aagaard Madsen, H.; Chaviaropoulos, B.; Douvikas, D.; Dahlberg, J.A.; Derrick, A.; Dunbabin, P.; Hunter, R.; Ruffle, R.;

[9] Albers A, Klug H, Westermann D, "Power Performance Verification", EWEC'99

[10] Pedersen TF, et.al. "Spinner Anemometry - An Innovative Wind Measurement Concept", EWEC2007 Milan

[11] IEC CD 61400-12-2 “WIND TURBINES – Part 12-2: Power performance of electricity producing wind turbines based on nacelle anemometry”, 88/325/CD, 2008-07-18

[12] Betz, A. „Der Maximum der theoretisch mölichen Ausnützung des Windes durch Windmotoren“, 1920, Zeitschrift für das gesamte Turbinenwesen, Heft 26, Sept. 26, pp. 307-309

5.4 Nacelle anemometry

Babak Diznabi

1. Introduction

In complex terrains or wind farms, the use of a met mast for power estimation is difficult and in some cases is impossible. Therefore increasing the accuracy of the nacelle anemometers for data collection came into consideration in order to use them for power performance estimation. However, collection of accurate wind speed data over the nacelle of the wind turbine is one of the most problematic elements in conducting wind turbine power performance tests. The problem is due to the changes in the wind flow characteristics as it passes through the rotor and over the nacelle of the wind turbine. The origin of these changes is a combination of many effects on the wind flow. Some of these effects originate from the nacelle geometry, blade roots, rotor loads and the yaw error of the wind turbine during operation.

Choosing the appropriate position for installing the wind sensor on the nacelle can increase the accuracy of the nacelle anemometry measurements. This can be done by understanding the behavior and the mentioned effects on the wind flow over the nacelle.

The perspective of this project was to analyze the wind flow conversed through a wind turbine rotor and over the nacelle. The aim was to use these analyses along with the IEC nacelle anemometry recommendations [[2]] to explore a feasible position for wind speed nacelle anemometry.

Analyses of the wind flow in front and behind the rotor over the nacelle were carried out on the NORDTANK wind turbine located at the Risø DTU test site.

2. Experimental part

In this experiment several sensors at different positions were used. The following measurements are considered to describe the wind flow at different positions:

- At hub height in front of the wind turbine near the rotor plane;
- At the rear end of the nacelle;
- At four intermediate positions between the two above positions.

The measurements are carried out with the following wind speed sensors:

- One cup anemometer on the met mast
- One Gill-R3 sonic anemometer on the calibration mast
- One spinner anemometer fixed on the hub of the wind turbine
- Two METEK sonic anemometers (ME1 and ME2) on the nacelle of the wind turbine

Figure 6 shows the setup for this experiment. Sonic anemometer ME2 is installed at four different places on the nacelle in different periods of measurement. Figure 7 shows the placements of ME2 together with other sensors on the nacelle of the *NORDTANK* wind turbine.

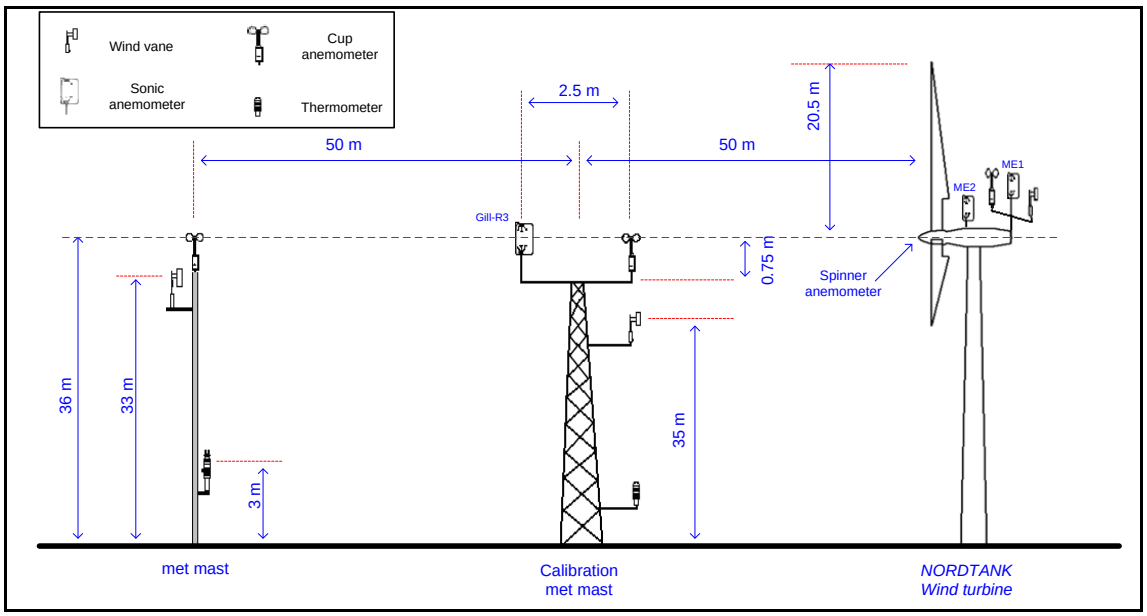

Figure 6: Simple sketch of the main instruments which is used in this project.

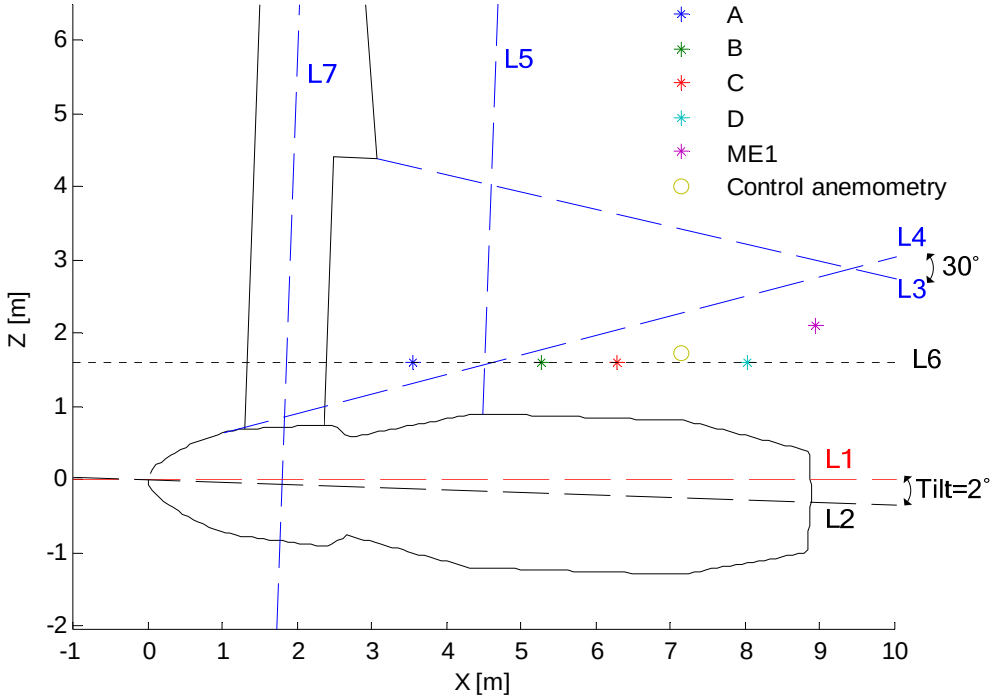

Figure 7: Placement of ME1, control anemometry and ME2 on the nacelle.
The recommended region from IEC is shown here (the triangle between L5, L4 and L3). The placements of ME2 are at positions 'A', 'B', 'C' and 'D'.

3. Data analyses

Three different analyses are made at each chosen position of ME2.

3.1 Analysis with mean values

Figure 8 to Figure 10, shows the general behavior of the wind flow over the nacelle. Figure 8 shows the horizontal wind speeds measured by ME2 at three different positions (A, B and C) versus the free wind speed derived from the spinner anemometer, DFWSh. As it is shown in this figure, there is a speed-down over the nacelle up to 10m/s and after this point there is speed-up over the nacelle. Figure 9 shows that the flow over the nacelle at these measurement points is downward. And Figure 10 shows that the flow is rotating counter to rotor rotation.

The last two observations can be investigated by considering the coordinate system shown in Figure 11.

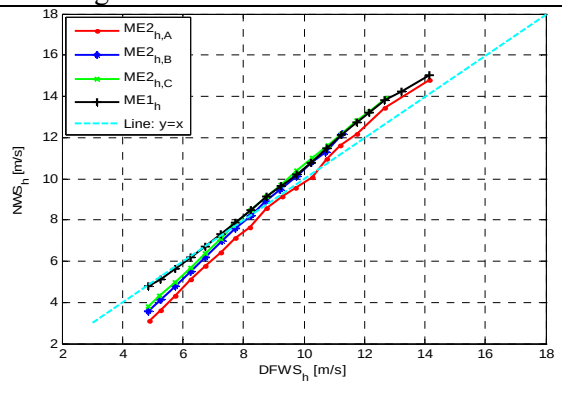

Figure 8: NWS_h (Horizontal wind speed) measured at different positions versus $DFWS_h$ (Derived free wind speed).

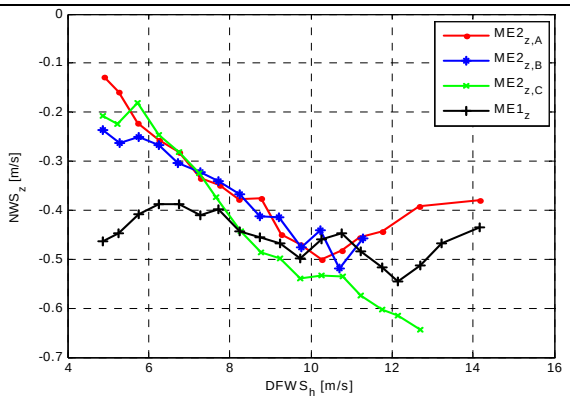

Figure 9: NWS_z (Vertical wind speed) measured at different positions versus $DFWS_h$ (Derived free wind speed).

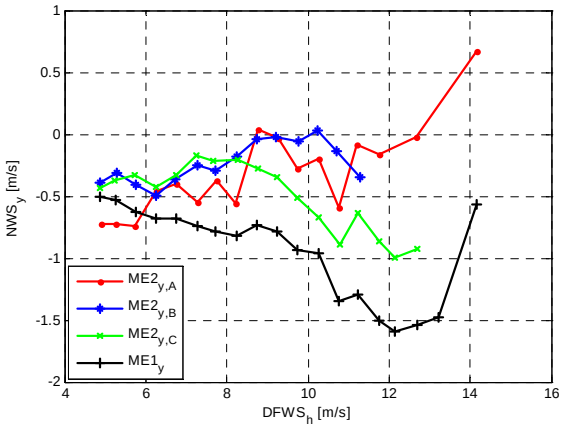

Figure 10: NWS_y (Latitude wind speed) measured at different positions versus $DFWS_h$ (Derived free wind speed).

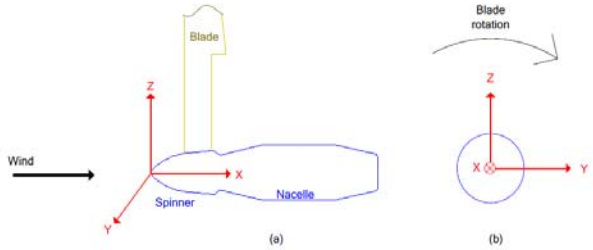

Figure 11: Left hand coordinate system used in this project. (a) : The side view of the nacelle. (b) : In front view of the nacelle (upstream view).

3.2 Turbulence Intensity analysis

The second analysis is based on the turbulence intensity calculations for each position. Figure 12 shows how the turbulence intensity is increasing from the spinner to point A and decreasing from point A to the end of the nacelle.

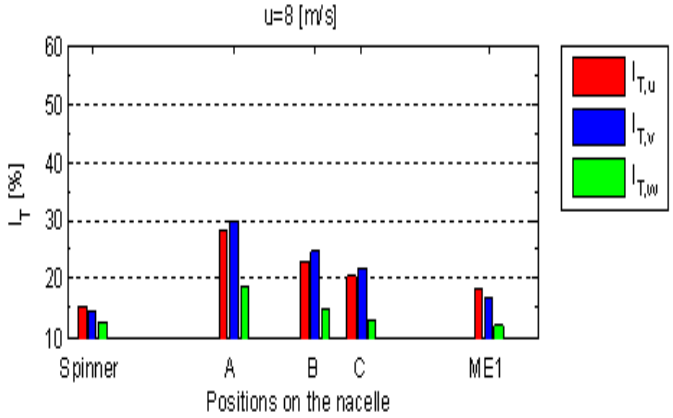

Figure 12: The change of turbulence intensities from the spinner to ME1.

3.3 Time series analysis

The third analysis concerns the time series data. In this analysis the local effect of the nacelle geometry and the blade roots on the wind flow are discussed.
It is shown how the local blade root affect on the wind flow at different positions will vary with changing the horizontal wind speed, inclination angle and yaw error. The main investigation of this analysis was that from position 'A' to ME1 the effects of the blade roots on the measurements decreases.

4. Validation of the nacelle anemometer placement

In order to validate the proper position for nacelle anemometry, the error of the horizontal wind speed calibration and AEP is considered. Table 2 shows these errors at different positions on the nacelle. The minimum error is corresponding to point B in both cases. As it is shown in Figure 7, B is the closest position to the IEC nacelle anemometry recommended area.

Position	error of horizontal wind speed calibration %	Error of AEP %
A	1.2111	8.8
B	0.5078	6.7
C	0.8402	6.7
ME1	0.9755	8.6

Table 2: The error of the horizontal wind speed calibration and AEP for each position.

5. Conclusions

The wind flow over the nacelle and in front of the rotor of the *NORDTANK* wind turbine was analyzed using measurements from various anemometers. This gives us an insight into the behavior of the wind flow passing through the rotor and over the nacelle.

A cup anemometer and an ultra sonic anemometer measure the wind flow on the met masts in front of the wind turbine. A spinner anemometer measures the wind flow on the hub of the wind turbine. An ultra sonic anemometer, which is placed on four different positions obtained by actuator disc modeling simulation, measures the wind flow over the nacelle. Another ultra sonic anemometer measures the wind flow at the rear end of the nacelle.

Analyses are carried out on the average data of wind speeds, turbulence intensity and time series data from the mentioned positions.

The average data analysis shows that the wind flow is spinning counter to the rotor rotation, with a downward direction, at the chosen positions above the nacelle.

The turbulence intensity analysis shows that it increases rapidly through the rotor and then decreases gradually toward the end of the nacelle.

By using time series analysis the local blade root effect and the rotor wake effect on the measured wind flow is investigated. The results show that the blade root effect is significantly high at the position on the nacelle near the blades. It then decreases through the rear end of the nacelle while the rotor wake effect increases. This demonstrates a level of inverse proportionality between the blade root effect and the rotor wake effect between the rotor and the end of the nacelle.

The measured horizontal wind speed at each chosen position on the nacelle is calibrated and the Annual Energy Production, AEP, is estimated based on each position's measurements. By analyzing the measurements and the error of the AEP estimation for each position, an appropriate position for mounting the anemometer on the nacelle is chosen. This chosen position conforms to the International Electrotechnical Commission, IEC, nacelle anemometry recommendations [[2]].

References

[1] Diznabi, B. (Master thesis March 2009) Investigation of the flow in relation to nacelle anemometry. Denmark: Technical University of Denmark, Risø National Laboratory for Sustainable Energy, Division of Wind Energy.

[2] International Electrotechnical Commission (2008) Power performance of electricity producing wind turbines based on nacelle anemometry, IEC 61400-12-2 CD Part 12-2

5.5 Spinner anemometry as an alternative to nacelle anemometry

Troels Friis Pedersen

1. Introduction

The state of the art of measuring wind on wind turbines is based on nacelle anemometry. In nacelle anemometry wind speed and wind direction are measured with sensors mounted on the upper side of the nacelle behind the rotor. Typically the sensors comprise a redundant pair of cup anemometers and wind vanes or a couple of 2D sonic sensors, see Figure 1. Nacelle anemometry provides input to the control system for yaw control, for start up and shut down, and is also used for power performance verification. Meanwhile, nacelle anemometry is hampered by the fact that it is positioned behind the rotor [1]. Nacelle anemometry measures wind that is influenced by: the wakes of the blade roots, the blade root vortices, the boundary layer over the nacelle, and the mounting arrangement of the nacelle anemometry. These effects can be calibrated for to a certain extent, but nacelle anemometry is also dependent on accurate adjustment at mounting. If the effect is significant, as indicated in Figure 2, it leads to losses in electric power and increased loads.

Figure 1 Arrangement of nacelle anemometry on the back of the nacelle of modern wind turbines. The instruments are typically mounted on a reasonably solid support structure with lightning protection covering the instruments and with redundant mounting of instruments

Figure 2 Often seen in the landscape: wind turbines that deviate significantly in yawing direction

2. Wind measurement in front of the rotor

With the so-called “spinner anemometer” the wind is measured on the wind turbine spinner in front of the rotor. Measurement of wind in front of the rotor avoids most of the flow distortion effects that is inherent in nacelle anemometry. Due to the rotation, the flow angle wind measurements also become insensitive to mounting inaccuracies. In front of the rotor, the wind is almost undisturbed by the rotor and the nacelle. The spinner does distort the wind flow, but in this case the distortion of the flow is an integrated part of the measurement principle, and cannot therefore be considered a disturbance. A flow distortion is, on the other hand, due to the blade roots, but thanks to the almost potential flow regime in the nose of the

spinner and around the blade roots, the influence is considered an integrated part of the concept in the same way as the spinner itself.

The concept of the spinner anemometer was first presented at EWEC2007 [2]. The idea to use the spinner arose from the shape of the nose of a pitot-tube, which is often spherical. Instead of measuring flow speed with differential pressure measurements directional wind speed is measured with sonic sensors, which has the advantage that flow components due to rotation are cancelled out. A spinner anemometer thus typically consists of three 1D sonic wind speed sensors mounted on the spinner as shown in Figure 3.

The flow over the spinner was investigated by CFD (Ellipsys code) [3]. Directional wind speeds were determined in the three fixed positions above the boundary layer over the spinner surface, see Figure 3. When the wind angle of attack on the spinner changes, the three wind speeds at the sensors change. This systematic change is used to measure the wind angles of attack. The principle can be easily understood by studying Figure 4 for a 10º upwards inflow angle.

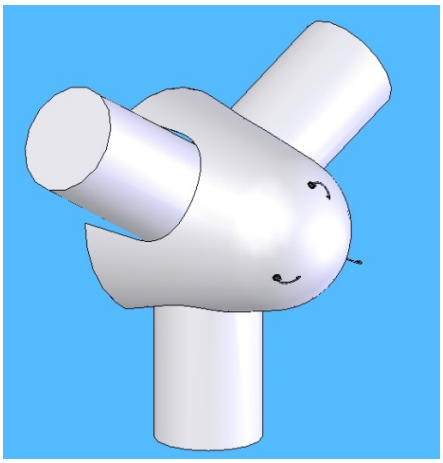

Figure 3 The concept of a spinner anemometer with three 1D sonic sensors mounted on the front part of the spinner. The spinner is in this figure shown with a spherical nose and a conical part.

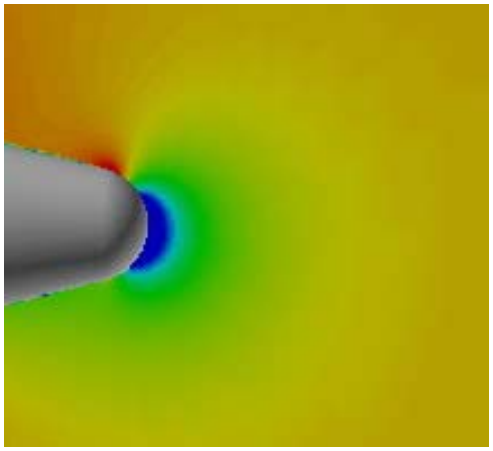

Figure 4 Wind speed contours around a rotational symmetric spinner without rotation (wind from the right). Wind is from the right and the air inflow angle is 10° from below. Notice the zero wind speed at the stagnation point at the nose (blue), the "free" wind speed (yellow-red) far in front of the spinner and at about 50° position over the surface of the spherical part, and the "overspeeding" (red) after the transition from spherical to conical part.

At an axial inflow to the spinner all three wind sensors measure the same wind speed. The "free" flow can then easily be determined by applying a constant to the average of the three measurements. When an off-axis wind speed is applied the three sensors experience a cosine shaped variation during a rotation, with each sensor offset by 120°. The flow wind speed over a small spinner, (S300), with the shape shown in Figure 4, was calculated with the ELLIPSYS code, showing the results as smooth curves in Figure 5.

The sensor wind speeds shown in Figure 5 can be found theoretically from derivation of the flow over a sphere. The signal of one sonic sensor can be expressed as a function of the inflow angle α and the inflow azimuth position φ at the location of the stagnation point on the spinner and the free wind speed U and two constants K_1 and K_2:

$$V_S = U(K_1 \cos\alpha + K_2 \sin\alpha \cos\varphi) \quad (1)$$

As seen in Figure 5, the average sensor wind speed over one rotation decreases with increasing inflow angle while the amplitude increases. In fact the average sensor wind speed

is reduced with the cosine to the yaw setting angle while the amplitude increases with the sine.

The ELLIPSYS calculated curves (smooth) in Figure 5 correspond very precisely to the theoretical curves (open dots) up to inflow angles at 60°. Only at 80° there is a significant deviation. In fact the analysis shows that the deviations decrease with the inflow angle. This is a characteristic that is in line with the purpose of the instrument; the smaller the yaw error, the more accurate the yaw error measurement.

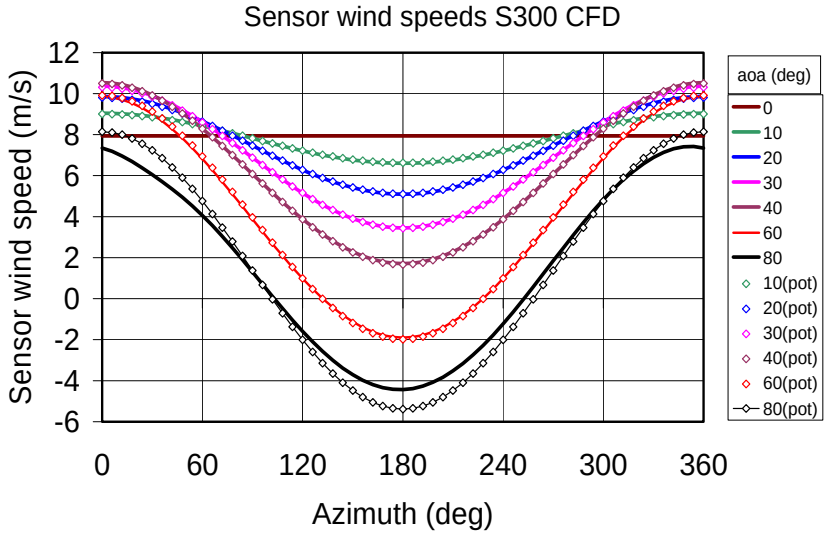

Figure 5 ELLIPSYS computed velocity distribution around the S300 spinner for 10m/s off-axis inflow at 0º, 10º, 20º, 30º, 40º, 60º, and 80º, smooth curves. Open dots represents theoretical values from formula 1.

With the expression in formula (1) for one sensor an expression can be found for each of the three sensors positioned at equidistant angles on the spherical nose. The inverse solution, to find the wind values from the sensor path air speeds, can then easily be derived. The yaw error and the flow inclination angle can be determined with only two instrument constants K_1 and K_2. K_1 is mostly connected to determination of the wind speed and K_2 is mostly connected to the flow angles. This makes calibration of the instrument just as simple as the gain and offset of a cup anemometer.

3. Free field comparison to 3D sonic anemometer

The S300 spinner anemometer was tested under field conditions at the Risø test site using the simple spinner anemometer algorithm with two constants, and with a rotational speed of 15rpm. A 3D Gill Windmaster sonic anemometer was mounted at same height and about three meters to the side of the spinner anemometer. The spinner anemometer and the sonic anemometer are shown in Figure 6. Figure 7, 8 and 9 show 100 seconds of time traces of the two wind sensors. The two sensors signals show quite comparable results.

Figure 6 Arrangement of the S300 spinner anemometer with "new" sensors in comparison with the sonic anemometer at Risø test site

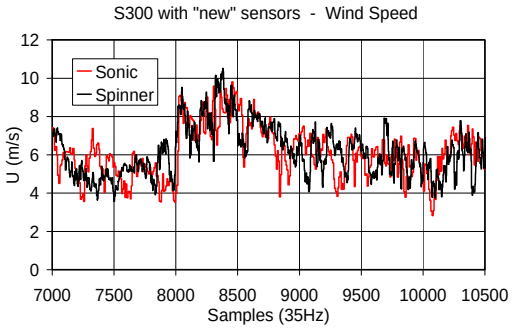

Figure 7 Comparison of measured wind speed at 35Hz sampling rate (100sec of data) of spinner anemometer and 3D sonic anemometer

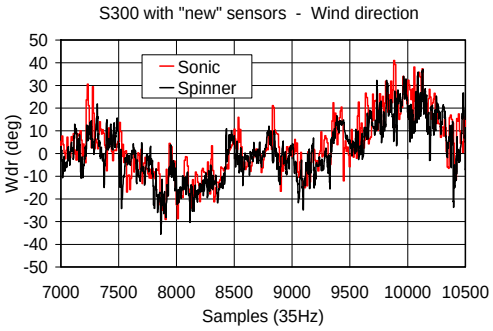

Figure 8 Comparison of measured horizontal inflow angle at 35Hz sampling rate

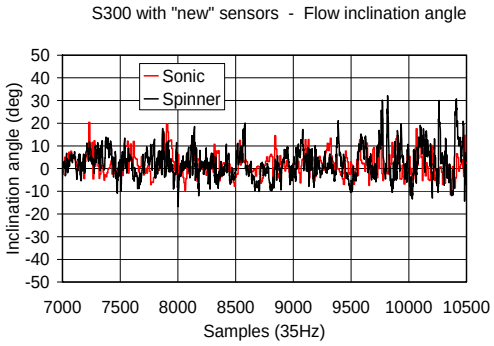

Figure 9 Comparison of measured vertical inflow angle at 35Hz sampling rate

4. Calibration of the spinner anemometer

There have been developed calibration procedures for the spinner anemometer. The key calibration factors of the spinner anemometer are the K_1 and K_2 factors, which are calibrated with a stopped rotor without rotor induction. The calibration can be made by CFD calculations or by field measurements. This calibration can be supplemented with an accredited traceable wind tunnel calibration and an internal spinner anemometer calibration to compensate for geometry deviations of the spinner and for sensor mounting.

5. Tests of spinner anemometers on wind turbines

The spinner anemometer has been tested on a 3,6MW wind turbine [4,5], see Figure 10. Yaw error measurements are shown in Figure 11. In this case the level of yaw error might lead to power losses in the order of 2%. The spinner anemometer has also been tested on turbines of different sizes.

Figure 10 The three 1D sonic wind sensors mounted on the 3,6MW wind turbine spinner at Risø DTU Høvsøre test site.

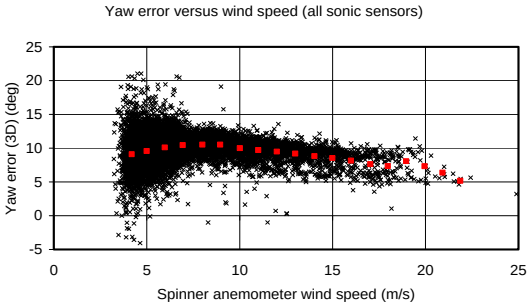

Figure 11 Yaw error of 3,6MW wind turbine (10min averages).

6. Further work

The spinner anemometer can be used for yawing of wind turbines, power performance verification, and for flow inclination measurements in complex terrain. A new project (EUDP Spinner-farm) has been started in 2009 which has the purpose to study yaw statistics of offshore wind turbines, to determine potential power losses due to yaw errors, and to verify power performance by nacelle/spinner anemometry.

7. Conclusions

The idea of using the spinner of a wind turbine for wind measurements has been investigated theoretically and experimentally. A spinner anemometer with a small spinner has been investigated in detail by wind tunnel tests and CFD, and the investigations confirm the ideas of the wind measurement concept. Spinner anemometers were tested on a 3,6MW wind turbine, and on a number of other wind turbines of different size, and the tests confirm that yaw errors can be measured accurately, and that wind turbine yawing can be improved.

References

[1] Frandsen S, Sørensen JN, Mikkelsen R, Pedersen TF, Antoniou I, Hansen K, 2009: The generics of wind turbine nacelle anemometry, EWEC2008 Marseille

[2] Pedersen TF, Madsen HA, Møller R, Courtney M, 2007: Spinner anemometry – an innovative wind measurement concept, EWEC2007 Milan

[3] Pedersen TF, Sørensen NN, Enevoldsen P, 2008: Aerodynamics and characteristics of a spinner anemometer, The Science of Making Torque from Wind

[4] Pedersen TF, Vita L, Sørensen NN, Enevoldsen P, 2008: Operational experiences with a spinner anemometer on a MW size wind turbine, EWEC2008 Marseille

6 Turbine loads and vibrations

6.1 Modal analysis techniques with point tracking videogrammetry

Uwe Schmidt Paulsen

1. Introduction

A new measurement technique of retrieving 3D positions in time and space has been developed at GOM, Germany and tested in collaboration with RISØ DTU on a 500 kW, 41 m Diameter wind turbine. Contributions as papers and workshop presentation [1,2,3,4] explain on the development of the method for deformation measurements from small objects to large objects. GOM has used the experience developed to encounter optical deformation measurements on a 100 m wind turbine. In USA[4] the technique adopted has been intensively used for analysis of simulated earth-quake impacts on a 55 kW turbine. The interest in using optical deflection measurements is to achieve a methodology, where testing shall be quick at less effort on large turbines with improved structural dynamics, bandwidth and accuracy input and that a wind turbine in a state of operation can be assessed in terms of Operational Modal Deflections (OMD) and Operational Modal Analysis (OMA).

The technique is based on that multiple cameras are observing distant light reflecting markers which enable optical, dynamic 3D analysis to determine position, motion and deformation calculation of structures and components. The Basic principle of photogrammetry is the geometrical triangulation in order to determine X,Y,Z-Coordinate of the centres of markers applied on the object, i.e. sub-pixel interpolation and finding the center of an Ellipse or Facet to 0.01 Pixel, to apply pattern recognition and to locate edges of ellipses or facets/subsets within each frame.

A review of literature within experimental testing of structures sensible to excitation of resonances shows in brief that analysis have advanced from signal- or system analysis techniques towards operational modal analysis. Analysis approaches such as physical modeling (mainly FEM) and system identification techniques: non-parametric, e.g. frequency peak picking, frequency domain decomposition, and parametric, e.g. ARMA, correlative function estimation, state space identification) are elements of modal testing [5, 6, 7, 8]. Though a flexible structure such as a 19 m wind turbine rotor blade can be modal analyzed by using acoustic or force excitation [9,10] and carrying out post simulations with software tools(such as ME'scope), accounting for noise input and robust estimation of modal frequencies, damping and mode shapes. However, there is still the entire wind turbine to consider under operational conditions. The structure is assembled from numerous flexible components, which makes the complete vibrant picture complex and a testing of the structure quite extensive in sensor instrumentation and analysis effort. A system analysis approach can provide answers in particular low frequency modes of the vibrant components. The technique of using the stroboscopic light effect on cam shafts triggered the idea to use this on wind turbines. [11] analyzed rotating shafts w.r.t. operating deflection shapes, and ways were identified to carry out this on the complete wind turbine structure when under normal operation. Laser vibrometry [12] has been used on rotating shafts for torsional deflection mode shape analysis.

GOM, with expertise in the field of optical and 3D measurement technique and digital image processing, has developed a method for measuring 3D motion of components with visible light (PONTOS) and improved this technique further for wind turbines of 100 m height during 2007. The present paper addresses on the potential with this method to obtain a modal signature of the wind turbine (height x width: 40m x 40m) in terms of dynamic behavior and vibration parameters and to describe first impressions with this experimental method. A photo of the optical system for object sizes (2-10 m) is given in Fig. 1.

Figure 1 : Stereo Camera system PONTOS, with tripod, cameras and flashes

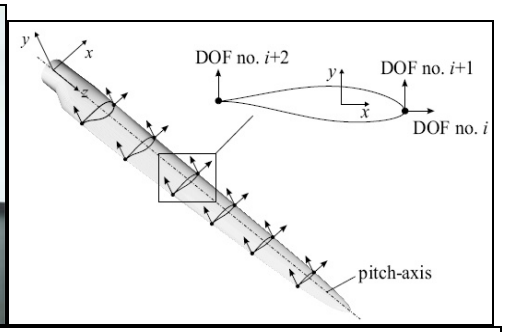

Figure 2 : Sensor positions (DOFs) [10]

2. Concept

In the absence of measured damping-, mass- and stiffness matrices we apply the mathematical notation, that the structure's vibrant response Z is a result of a mechanical load with associated displacement X: Z=H·X [13]. With measured 3D coordinate y on a wind turbine component, displacements of points relative to a reference point x could be used for applying modal analysis techniques [14, 15], e.g. transmissibility functions, operating deflection shapes, parameter estimation of damping and resonances, and mode shapes. For the instrumented blade shown in Fig. 2, Origo is regarded as a reference position w.r.t. to other sensor positions on the blade. The blade is interpreted as a lumped system with DOF elements, each represented as a SDOF system. With the reference position moving in space, the response functions (Mod, Arg) for the vector displacement z=y-x typically looks as in Fig. 3. For the wind turbine under normal (e.g. non-transient) conditions, transmissibility functions contain responses excited by Gaussian stochastic wind. Calculating 3D positions with an optical system is based on, that two cameras have their slightly angled picture plane fixed at a mutual distance and on a line connecting each. The line is perpendicular to the line from the object to the optical system. The digital stereo camera system records different load or movement states, and the software assigns 3D coordinates to the image pixels. The digital images are compared and the displacement of the reference points is computed.

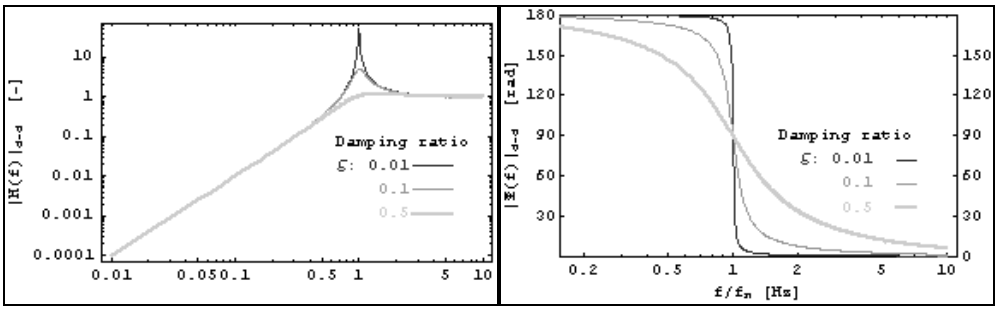

Figure 3 Frequency response functions, SDOF

3. The experiment

Description

The optical system setup for measuring deflections on a wind turbine is seen in Fig. 4. The distances from the 40 m rotor to the cameras is approximately 100 m. The optical system is capable to measure objects of 100 m rotor diameter. The reflective light from the targets are recorded at a speed of 100 Hz. Special reflective targets of diameter D are applied on the turbine in a way as visually seen in Fig. 4. Following 'rules of thumb' are applied:

- The markers are distributed as many as possible on the surface at sufficient intervals.
- Between spots: a distance of 2-3D.

- The domain surrounding the target contains significant contrast compared to the target for calculating torsion.
- A line consisting of at least 3 markers defines a pitch deflection axis.

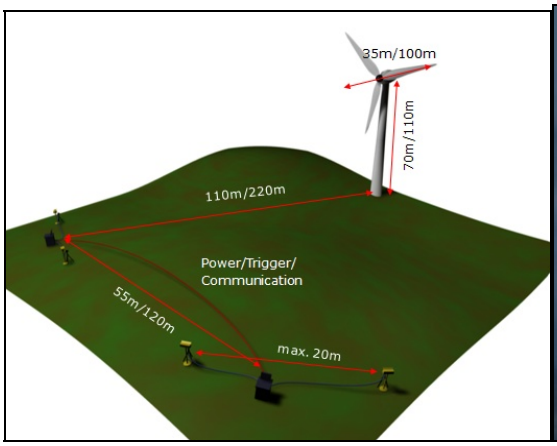

Figure 4 Experimental layout of camera system

Figure 5 The effect of flash on the reflective markers.Wind turbine at campus, Dec 2007.

([10], p16) concluded on the accelerometer positioning in terms of uncertainty for the mode shape calculation (see Fig. 1 on the relative variation of DOF_{i+2} and DOF_{i+1}):

- The distance between two targets measuring the flap wise accelerations should be as large as (practical) possible
- The angle between their measuring axes should be as close as possible to zero.

The wind turbine is instrumented with a variety of sensors on the rotor, nacelle and tower and measurement equipment for 35Hz to 10 kHz sampling. Measurement records are stored for post analysis in a data base. [16, 17] describe recent development and activities carried out with this wind turbine. Analysis of the data is carried out on the basis of the 35 Hz sampled records.

4. Calibration

The optical system is self-calibrating for effects influencing the optical quality and consistency. In general these effects are non-linear and dependent on the lens quality and the CMOS system. Once calibrated the cameras are able to detect positions when flash light bursts illuminate the targets and the pixels are stored on the CMOS plate, row by row.
A proper selection of the reference target is a key issue for determination of mobility. The camera settings shall match the condition, that all targets are captured and recognized.

5. Results

Lessons learned

During the setting up the optical system, as a field experiment, experiences due to weather impact on soil conditions, on hardware and wind turbine testing conditions were made. Firstly the wind changed in direction and dropped down to conditions where the turbine could not operate under steady conditions. This condition is not ideally for the analysis of the vibration of the wind turbine, in particular the condition provides a major impact on the assumption of the analysis methods of modal analysis. The loads are less energetic than under high wind conditions, which have in particular impact on the operating deflection shapes [14]. The excitation of the lightly damped structure practically exists for impacts with frequencies close to resonance (e.g. operating deflection shape~modal shape). Secondly the cameras, computers and flashes were placed on ploughed land. The soil-softness changed accordingly with precipitation and frost. However, a fixed position of the optical system was achieved.

Because of lack of high wind conditions during the initial tests, preventing access to responses at normal operation and at standstill, it was decided to follow up on the present concept at a later stage.

The test wind turbine rotor is mounted in upwind position, which makes the markers applied on the tower 'blind' for the cameras at the blade position is pointing downward. In this situation no data can be extracted from these targets, but this window lacking data is very narrow compared to one revolution.

Test cases

Despite the low wind speeds, some results from the conducted tests are presented. The rotor speed was increased by means of forcing the asynchronous generator works as a motor, and then let the wind turn the wind turbine rotor. Following tests were carried out under these conditions:

- rotor idling, RPM varying
- stop sequences (e.g. grid loss simulation)

To provide some results for the edgewise blade bending, rotor shaft torsion and tower bending at the bottom, Fig. 6 shows a comparison of measured spectral load responses.

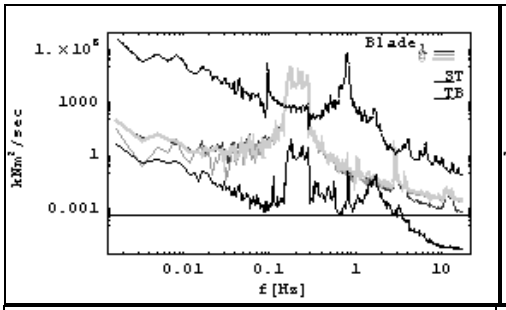

Figure 6 PSD of edgewise bending moments, tower base bending moment and rotor shaft torsion

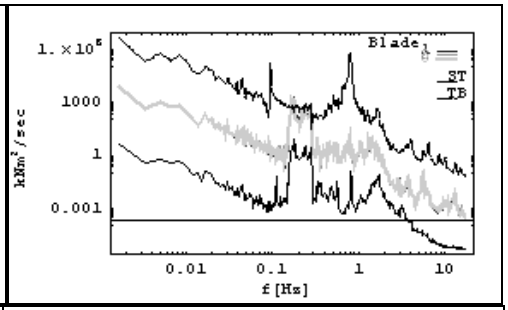

Figure 7 PSD of flap wise bending moments, tower base bending moment and rotor shaft torsion

Here at this atypical operating condition the turbine is rotating slowly at a speed of 0.17-0.29 Hz, demonstrating the edgewise blade vibration and in the rotor shaft. Furthermore the blade masses rotating with the rotor plane excite the tower natural frequency at about 0.8 Hz, and the 1'st symmetrical mode of the edgewise blade frequency at around 3.0 Hz.

The wind power spectrum is a straight sloping line following the main trend of the signals in the Fig. 6. A similar explanation on the influence of this ambient exciter is applicable for Fig. 7, which also reveals a similar result as in Fig. 6 on the coupled vibrations in the structure with a major flap wise motion correlated to the tower bending response and rotor shaft bending.

The 1'st symmetrical flapwise blade frequency mode is found at 1.5 Hz. In comparison, the optical displacement offers the ability to investigate on the vibrations which occur in the structure, as seen in Fig. 8. In the figure the Cartesian co-ordinate system is oriented as indicated, with a positive axis co-parallel with the wind. Furthermore mainly 1 Hz sinusoidal cycles from out-of-plane deflections correlated and synchronized with the 1'st bending mode of the main shaft are also observed from the spectral load response results. Phase information is seen from Fig. 8, when comparing deflections at the indicated radial position on the different blades.

The flapwise deflection of a cantilevered 19 m blade is measured and computed in [10] and consists of a relative measure of the deflection shape along the blade for the different modes. The operational deflection measured here is by magnitude superimposed with the wind loading and the mode shapes at this operating condition. To decouple these effects, detailed analysis of the test data are planned for the next measurement. The analysis of 3D motion requires static points to be referenced to. In the following part of the rotor plane has been used for developing a surface.

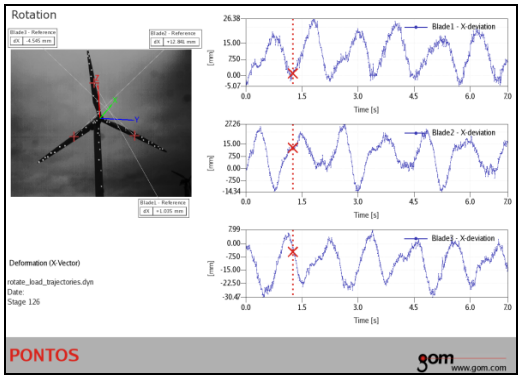

Figure 8 Optical measurement results, deflection in wind ward direction

Fig. 8 shows the out-of-plane movement of selected markers on the rotating blades. The signals contain several harmonics and show a proper resolution compared to the level of what can be detected (0.1-1 mm). The result is quite remarkable because the information regarding into the optical plane almost vanishes (still the view is slightly from below).

Fig. 9 visualizes the conditions during stopping of the rotor (grid loss simulation). The turbine is slowed down from 27 rpm to standstill. Again a lot of dynamics is developing when the rotor slows down. In Fig. 10 it is seen, that the tower deflects up to 15 mm at this stage.

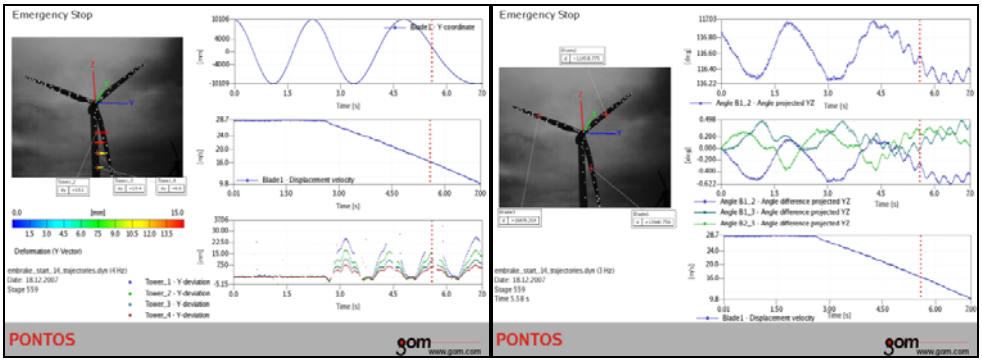

Figure 9 Phase angles and deflections during emergency shut down

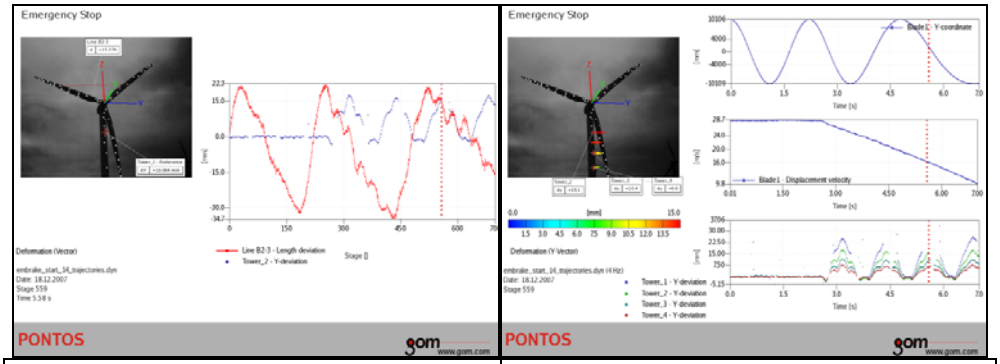

Figure 10 Blade and tower motion at the beginning of the emergency shut down

Figure 11 Tower deflections

At the end of the stop, the rotor is pitching back and forth due to backlash in the gearbox. This motion can be seen in Fig. 10, where the distance between the markers on two blades is monitored.

For the two blades in upside position as indicated on the image, the blades bend downwards causing an elongation. At the opposite position the situation has reversed to a

shortening of the distance between the markers. Fig.11 shows the in-plane deflection of the tower.

6. Conclusions

A novel method of measuring 3D positions of wind turbine components during operation has been introduced. The method is applicable for wind turbines of 100 m in size and is capable to measure 3D position, motion and acceleration with sufficient resolution and bandwidth. In the paper the analysis has been limited to results from the optical analysis and to a comparison with load measurements, carried out with traditional acquisition system hardware. With this method works has to be continued in analysis of the load responses:

- determination of deflection shapes and modal shapes, and the comparison
- analysis at standstill and at normal operation conditions
- impacts(emergency stop)

References:

[1] Paulsen.U.S. et al. *Modal Analysis on a 500 kW Wind Turbine with Stereo Camera Technique* Presented at IOMAC, Ancona Italy May 2009

[2] Paulsen.U.S. et al. *Wind Turbine Operational and Emergency Stop Measurements Using Point Tracking Videogrammetry*, Presented at SEM, Albuquerque USA .June2009.

[3] Paulsen.U.S. et al. *Full scale measurements with Pontos* Workshop GOM Braunschweig Germany May 2009.

[4] Paulsen.U.S. et al. *Developments in Large Wind Turbine Modal Analysis Using Point Tracking Videogrammetry*, Presented at IMAC-XXVIII February 2, 2010 Jacksonville, Florida USA

[5] Andersen, P. 1997. Identification of Civil Engineering Structures using ARMA Models PhD Thesis, Aalborg University, Denmark.

[6] Overschee, E. and de Moor, P. 1996 *Subspace Identification for Linear Systems: Theory, Implementation, Applications.* Kluwer Academic Publishers.

[7] Ventura C. E. and Gade, S. April 2005, *IOMAC Pre-Course*. IOMAC 2005. Copenhagen, Denmark

[8] Andersen, P., Brincker, R. ,2001. *The Stochastic Subspace Identification Techniques*.www.svibs.com

[9] Gade, S. 2003. Modal Parameters from a Wind Turbine Wing by Operational Modal Analysis. Inter·noise. Korea

[10] Larsen, G.C. et al. 2002. *Modal Analysis of Wind Turbine Blades.* Risø-R-1181(EN)

[11] Døssing O., Structural Stroboscopy -*Measurement of Operational Deflection Shapes,* Brüel & Kjær Application Note (BO 0212)

[12] Gatzwiller, K. B&K Application note, Measuring Torsional Operational Deflection Shapes of Rotating Shafts. BO 0402. www.BKSV.com

[13] Bendat, J. et al. 1971. *Random Data: Analysis and measurement procedures*. Wiley - Interscience

[14] McHargue, P. L., Richardson, M.H. 1993.*Operating Deflection Shapes from Time versus Frequency Domain Measurements.* 11'Th IMAC conference Florida USA

[15] Richardson, M.H. 1997. *Is It a Mode Shape or an Operating Deflection Shape?* Sound & Vibration

[16] Helgesen, K.O.et al, 2006, Wind Turbine Measurement Technique-an Open Laboratory for Educational Purposes. Wind Energy 11 pp.281-295 Wiley Interscience

[17] Paulsen. S. 2007. Preliminary Results with A Novel Drive Train Measurement System, *EWEC2008, Brussels, Belgium*

7 Complete list of publications

7.1 Journal papers

Bingöl, Ferhat ; Mann, Jakob ; Foussekis, Dimitri; *Conically scanning lidar error in complex terrain*, Meteorologische Zeitschrift (ISSN: 0941-2948) (DOI: 10.1127/0941-2948/2009/0368) , vol: 18, issue: 2, pages: 189-195, 2009

Bingöl, Ferhat ; Mann, Jakob ; Larsen, Gunner Chr.; *Light detection and ranging measurements of wake dynamics Part I: One-dimensional Scanning*, Wind Energy (ISSN: 1095-4244) (DOI: 10.1002/we.352) , vol: 13, issue: 1, pages: 51-61, 2010

Gottschall, Julia; Wagner, Rozenn; Courtney, Michael;. Jørgensen, Hans E. and Antoniou, Ioannis. *Lidar profilers in the context of wind energy – A verification procedure for traceable measurements*; Wind Energy (submitted).

Mann, Jakob ; Cariou, Jean-Pierre ; Courtney, Michael ; Parmentier, Remy ; Mikkelsen, Torben ; Wagner, Rozenn ; Lindelöw, Per Jonas Petter ; Sjöholm, Mikael ; Enevoldsen, Karen; *Comparison of 3D turbulence measurements using three staring wind lidars and a sonic anemometer*, Meteorologische Zeitschrift (ISSN: 0941-2948) (DOI: 10.1127/0941-2948/2009/0370), vol: 18, issue: 2, pages: 135-140, 2009

Mann, Jakob ; Peña Diaz, Alfredo ; Bingöl, Ferhat ; Wagner, Rozenn ; Courtney, Michael; *Lidar Scanning of Momentum Flux in and above the Atmospheric Surface Layer*, Journal of Atmospheric and Oceanic Technology (ISSN: 0739-0572)

(DOI: 10.1175/2010JTECHA1389.1) , vol: 27, issue: 6, pages: 959-976, 2010

Peña A, Hasager CB, Gryning SE, Courtney M, Antoniou I, Mikkelsen T; *Offshore wind profiling using light detection and ranging measurements*, Wind Energy, 2009; 12:105—124

Peña A, Gryning SE, Hasager CB; Measurement and modeling of the wind speed profile in the Marine Atmospheric Boundary Layer, Boundary-Layer Meteorology, 2008; 129:479--495

Sjöholm, Mikael ; Mikkelsen, Torben ; Mann, Jakob ; Enevoldsen, Karen ; Courtney, Michael; *Spatial averaging-effects on turbulence measured by a continuous-wave coherent lidar*, Meteorologische Zeitschrift (ISSN: 0941-2948) (DOI: 10.1127/0941-2948/2009/0379) , vol: 18, issue: 3, pages: 281-287, 2009

Trujilio,Juan-Jose; Bingöl, Ferhat ; Larsen, Gunner Chr.; Mann, Jakob ; Kuhn, Martin; *Light detection and ranging measurements of wake dynamics Part II: Two-dimensional Scanning*, Wind Energy Published online. DOI: 10.1002/we.402, 2010

Wagner R., Antoniou I., Pedersen S.M., Courtney M.S. and H.E. Jørgensen, 2009: The influence ot eh wind speed profile on wind turbine performance measurements, Wind Energy, **12**:348-362.

Wagner R., Courtney M.S., Gottschall J. and P. Lindelöw-Marsden, 2010: Accounting for the speed shear in wind turbine power performance measurement, submitted to Wind energy, under review.

7.2 Conference papers

Bingöl Ferhat; Mann Jakob; Foussekis, Dimitri. Lidar performance in complaex terrain modeled by WAsP Engineering, EWEC, 2009

Courtney Michael, Wagner Rozenn and Lindelöw Petter; Testing and comparison of lidars for profiles and turbulence measurements in wind energy,

IOP Conference Series: Earth and Environmental Science (ISSN: 1755-1307) (DOI: 10.1088/1755-1315/1/1/012021) , vol: 1, 2008

Gottschall Julia, Courtney Michael, Lindelöw Petter, and Albers Axel: Classification of lidar profilers – or: how to introduce lidars to power performance testing; EWEC 2010

Hasager CB, Peña A, Christiansen MB, Astrup P, Nielsen M, Monaldo F, Thompson D, Nieslen P. *Remote sensing observation used in offshore wind energy*, 2008, IEEE 1939--1404

Lindelöw, Per Jonas Petter ; Courtney, Michael ; Parmentier, R. ; Cariou, J.P. *Wind shear proportional errors in the horizontal wind speed sensed by focused, range gated lidars* in journal: IOP Conference Series: Earth and Environmental Science (ISSN: 1755-1307) (DOI: 10.1088/1755-1315/1/1/012023) , vol: 1, 2008

Mikkelsen, Torben. *On mean wind and turbulence profile measurements from ground-based wind lidars : limitations in time and space resolution with continuous wave and pulsed lidar systems - a review*, EWEC 2009

Mikkelsen, Torben ; Hansen, Kasper Hjorth ; Angelou, Nikolas ; Sjöholm, Mikael ; Harris, Michael ; Hadley, Paul ; Scullion, Richard ; Ellis, Gary. *Lidar wind speed measurements from a rotating spinner,* EWEC 2010

Mikkelsen, Torben ; Mann, Jakob ; Courtney, Michael ; Sjöholm, Mikael. *Windscanner: 3-D wind and turbulence measurements from three steerable doppler lidars*, IOP Conference Series: Earth and Environmental Science (ISSN: 1755-1307) (DOI: 10.1088/1755-1307/1/1/012018), vol: 1, pages: U148-U156, 2008

Sathe, A.; Mann, Jakob ; Gottschall, Julia ; Courtney, Michael. *Systematic error in the estimation of the second order moments of wind speeds by lidars*, 2010, ISARS

7.3 Reports

Angelou N, Mikkelsen T, Hansen KH, Sjöholm M, Harris M.. *LIDAR Wind Speed Measurements from a Rotating Spinner: "SpinnerEx 2009",*Risø-R-1741(EN), 2010

Angelou N., Mann J., Courtney M., Sjöholm M., Doppler lidar mounted on a wind turbine nacelle – UPWIND deliverable D6.7.1, Risø-R-1757(EN), 2010

Bingöl, Ferhat ; Mann, Jakob ; Foussekis, Dimitri. *Modeling conically scanning lidar error in complex terrain with WAsP Engineering,* Risø-R-1664(EN), 2008

Gottschall, Julia ; Courtney, Michael. *Verification test for three WindCube WLS7 LiDARs at the Høvsøre test site*, Risø-R-1732(EN) (ISBN: 978-87-550-3819-6), pages: 44, 2010

Lindelöw-Marsden P, UpWind D1. Uncertainties in wind assessment with LIDAR, Risø-R-1681, Risø 2008.

Mann J., Carious J.-P., Courtney M.S., Parmentier R., Mikkelsen T., Wagner R., Lindelöw P., Sjöholm M. and Enevoldsen K., Comparison of 3D turbulence measurements using three staring wind lidars and a sonic anemometer, Risø-R-1660(EN), 2008

Mikkelsen, Torben; Jørgensen Hans E., Kristensen Leif. *The bistatic Sodar "Heimdall"_ You blow, I listen*, Risø-R-1424(EN), 2007

Pedersen, Troels F., *Quantification of Linear Torque Characteristics of Cup Anemometers with Step Responses*, Risø-I-3131(EN), 2011

Wagner R. and M.S. Courtney. *Multi-MW wind turbine power curve measurements using remote sensing instruments - the first Høvsøre campaign*, Risø-R-1679(EN), 2009

Wagner R., Courtney M.S., Gottschall J. and P. Lindelöw-Marsden: *MultiMW wind turbine power curve measurement using lidar (second Høvsøre campaign)*, Risø-I-2954(EN), 2009

Wagner, Rozenn ; Mikkelsen, Torben ; Courtney, Michael. *Investigation of turbulence measurements with a continuous wave, conically scanning LiDAR*, Risø-R-1682(EN) (ISSN: 0106-2840) (ISBN: 978-87-550-3736-6), 2009

7.4 PhD thesis

Bingöl Ferhat, *Complex Terrain and Wind Lidars*, Risø-PhD-52(EN), 2009

Peña Alfredo, *Sensing the wind profile*, Risø-PhD-45(EN), 2009

Wagner Rozenn, *Accounting for the wind shear in wind turbine performance measurement*, Risø-PhD-56(EN), 2010.

7.5 Master thesis

Bingöl Ferhat, *Adapting a Doppler laser anemometer to wind energy*, Technical University of Denmark, Risø National Laboratory for Sustainable Energy, Division of Wind Energy.

Diznabi Babak, *Investigation of the flow in relation to nacelle anemometry.* Technical University of Denmark, Risø National Laboratory for Sustainable Energy, Division of Wind Energy.

Risø DTU is the National Laboratory for Sustainable Energy. Our research focuses on development of energy technologies and systems with minimal effect on climate, and contributes to innovation, education and policy. Risø has large experimental facilities and interdisciplinary research environments, and includes the national centre for nuclear technologies.

Risø DTU
National Laboratory for Sustainable Energy
Technical University of Denmark

Frederiksborgvej 399
PO Box 49
DK-4000 Roskilde
Denmark
Phone +45 4677 4677
Fax +45 4677 5688

www.risoe.dtu.dk